**Title**
Odorant Detection by Biological Chemosensor Arrays



**Author**
Schuech, Rudi

**Publication Date**
2011

Peer reviewed|Thesis/dissertation

# Odorant Detection by Biological Chemosensor Arrays

by

Rudi Carl Schuech

A dissertation submitted in partial satisfaction of the

requirements for the degree of

Doctor of Philosophy

in

Engineering – Civil and Environmental Engineering

in the

Graduate Division

of the

University of California, Berkeley

Committee in charge:

Professor Mark T. Stacey, Chair

Professor Fotini Katopodes Chow

Professor Mimi A. R. Koehl

Fall 2011

# Abstract

## Odorant Detection by Biological Chemosensor Arrays

by

Rudi Carl Schuech

Doctor of Philosophy in Engineering – Civil and Environmental Engineering

University of California, Berkeley

Professor Mark T. Stacey, Chair

The antennules of many marine crustaceans enable them to rapidly locate sources of odorant in turbulent environmental flows. The antennules are typically flicked through the water, causing the animal to take spatially and temporally discrete odorant samples. A substantial gap in knowledge concerns how the physical interaction between chemosensory appendages and the chemical filaments forming a turbulent plume affects odorant detection and filters the information content of the plume. The research presented here is focused on using numerical models to simulate the flow of odorant-laden water around arrays of chemosensory aesthetascs, and the transport of odorant molecules to their surfaces, during a plume sampling event. The time-varying odorant flux signals generated during these events are of key interest, since they are the lens through which a plume tracking agent will perceive its odor environment.

Simulations of infinitely long arrays of sensory hairs indicate that there are likely to be design tradeoffs between maximizing the sharpness of an odorant flux signal versus the total amount of odorant mass detected. It is also clear that the duration of odorant flux during a sampling event similar to a flick downstroke is not long enough to enable detection of 0.6 mm wide odorant filaments by crustaceans such as lobsters, or by engineered chemical

sensors currently available. This suggests that the return stroke and interflick pause may be critical if these animals are to detect fine-scale plume structures.

Models of hair arrays with a finite number of hairs reinforce the above conclusions, but because this more realistic geometry allows water to flow around the array of hairs in addition to through, it reveals additional behaviors that the infinite array simplification cannot capture. Fundamentally different trends in metrics describing the sharpness of the flux signal are observed for rapidly flicking, sparse arrays of hairs versus slowly moving, densely packed arrays. These surprising transitions are not well predicted by simple parameters describing only the fluid velocity field, pointing out the importance of explicitly modeling or observing odorant transport in addition to the flow of water.

A tomographic scan of a real aesthetasc array morphology, that of the spiny lobster *P. argus*, reveals substantial variation and deviation from any simple, idealized geometry, and 3D effects are likely to be important to its odorant sampling dynamics. Nonetheless, numerical simulations of an idealized version of *P. argus* morphology indicate that on average, odor-laden water is effectively channeled into the aesthetasc array as compared to a simple straight row of hairs. A simple row, however, still achieves greater odorant flux in most regards, again emphasizing differences in properties of the flow versus properties of passive scalar transport. Crustacean antennules might therefore best serve as starting iterations instead of optimal solutions for the design of engineered chemical sensor arrays for use on plume tracking robots.

To Mom, Dad, Pamela,

and Sarah.

# Contents

# Acknowledgments

My advisor, Mark Stacey, made this work possible through his insightful discussions and determined optimism. His ability to sift through a tangled pile of graphs and find meaning is uncanny. His sincere desire to guide his students to success, regardless of all obstacles and wrong turns, is profound. One could not ask for a better mentor. Faculty members Mimi Koehl, Tina Chow, Evan Variano, and Jon Wilkening were also instrumental as exam and dissertation committee members, and provided many invaluable bits of guidance along the way. I can confirm that UC Berkeley lives up to its reputation for fostering interdisciplinary discussion and collaboration; in particular, I'd like to thank Alastair MacDowell at the Lawrence Berkeley National Lab, who made a large portion of this work possible.

I am lucky to have had a most interesting group of colleagues in the environmental fluid mechanics research group. You all (especially Wayne Wagner, Ian Tse, Megan Williams, Rusty Holleman, Audric Collignon, Maureen Downing-Kunz, and Christina Poindexter, and Kevin "Fake Mary" Hsu) made certain that a day at the office was anything but mundane. In the early days, Patrick Granvold, Kyle Pressel, Rebecca Leonardson, Lissa MacVean, and Mary Cousins also provided much needed support, even if often in the form of shared pessimism, when I couldn't yet see the light at the end of the tunnel. Lastly, at Berkeley I gained both a close friend and inventive collaborator, Mike Fisher, whose eccentric humor has probably rubbed off on me more than I'd like to admit.

My parents gave me the insatiable scientific curiosity that started me along this journey. My sister ensured that the house was perpetually filled with all manner of animals to foster my love of biology. My teachers and professors, those mentioned above and particularly Ashim Datta, gladly engaged my endless questions and encouraged me to ask more. Most importantly, I could not have completed this work without the unwavering support of Sarah Boyd, the love of my life. She inspires me to ask the hardest questions, and to go seek out the answers.

# 1. Introduction

## 1.1. Background and motivation

The sense of smell is essential to many animals in the location of food and suitable habitats, identification of mates and predators, and communication with conspecifics. While many animals (e.g., marine crustaceans) are adept at rapidly tracking odors to the source, how they do this is not well understood. The interaction between an organism's olfactory organs and the surrounding odor-laden fluid is the animal's first step in filtering information contained in its odor environment. These organs are interesting not only from a biological standpoint, since olfaction mediates many ecologically important activites, but also an engineering standpoint, since they may yield insight into the design of artificial noses. This chapter introduces the many overlapping aspects of chemical sensing in the fluid environment, including the fluid dynamics of odorant transport, the morphology and neurobiology of crustacean olfactory appendages, and the state of current artifical sensing technology.

### 1.1.1. Turbulent plumes and plume tracking

#### Overview

Turbulent scalar plumes are ubiquitous in the environment and can consist of many quantities besides the odorants of interest to animals: chemicals (e.g., pesticides used in confined aquaculture as in Ernst et al. 2001 or stack emissions in air), pH (e.g., due to dissolved CO2 resulting from oceanic carbon sequestration as in Huesemann et al. 2002), concentrated brine (e.g., from desalination as in Alameddine and El-Fadel 2007), or temperature (e.g., thermal pollution via power plant cooling as in Wilson and Anderson 1984). In turbulent flow, these scalars do not smoothly diffuse outward from the source, as would occur in laminar flow. Instead, regions of high scalar concentration are strained into wispy, filamentous plumes by the turbulence (Crimaldi and Koseff 2001, Webster et al. 2003, Crimaldi and Koseff 2006). These plumes fluctuate rapidly in time and space and exhibit

complex instantaneous structure as depicted in Figure 1.1 A. The instantaneous gradient in the scalar value (e.g., odor concentration) is steep and frequently in a different or even opposite direction than the source, unlike the smooth monotonic gradients found in laminar plumes or quiescent, diffusion dominated conditions such as those encountered by microorganisms. Furthermore, turbulent plumes in the natural environment display even more complex behavior than laboratory studies might suggest, due to heterogenous bed structure (e.g., coral reefs) and large scale meander due to waves. Orienting in turbulent plumes and quickly tracking such plumes to their sources are therefore very challenging problems.

If concentration is averaged over a long period of time, a time-averaged plume is indeed well-behaved, with smooth gradients of increasing concentration toward the source as seen in Figure 1.1 B (Crimaldi et al. 2002b). Some macroscopic animals (e.g., marine snails as in Ferner and Weissburg 2005, tsetse flies as in Bursell 1984) may indeed simply travel up the average chemical gradient to locate the plume source. However, many organisms (e.g., marine crustaceans such as lobsters and crabs) do not have the luxury of waiting several minutes for time-averaged statistics to converge while tracking a plume to its source (Webster and Weissburg 2001). Besides the ephemeral nature of odor sources such as motile prey, it is important for tracking agents to make navigational decisions on a time scale faster than any large scale plume meander. Animals are clearly able to do this, but which plume features they do use is not known.

### Orientation and guidance cues

Despite the seemingly chaotic nature of instantaneous turbulent plume structure, several researchers have found correlations between features of individual odor "filaments" and position relative to the source location. Researchers first used electrochemical probes to measure concentration records at several points within the plume (Murlis and Jones 1981, Moore et al. 1992; 1989; 1994, Finelli et al. 1999), while newer studies (Crimaldi and Koseff 2001, Webster and Weissburg 2001, Koehl 2001b, Crimaldi et al. 2002b, Liao and Cowen 2002, Mead et al. 2003, Crimaldi and Koseff 2006, Dickman et al. 2009) generally utilize laser induced fluorescence (LIF) (Crimaldi 2008) to capture entire 2D slices or even 3D volumes (Dickman et al. 2009) of the evolving concentration field. Note that spatial structure of the plume is captured directly by LIF, while electrochemical probes convert spatial patterns into temporal patterns. Both methods have yielded similar descriptions of turbulent chemical plumes at a small scale. As a scalar plume is advected downstream and mixed by turbulence and diffusion, scalar filaments become wider and less concentrated. Quantitatively, both peak filament concentration and the peak onset slope of odor concentration, a measure of filament sharpness, decrease with distance downstream from the source (Moore and Atema 1991, Finelli et al. 1999, Webster and Weissburg 2001). Individual odor

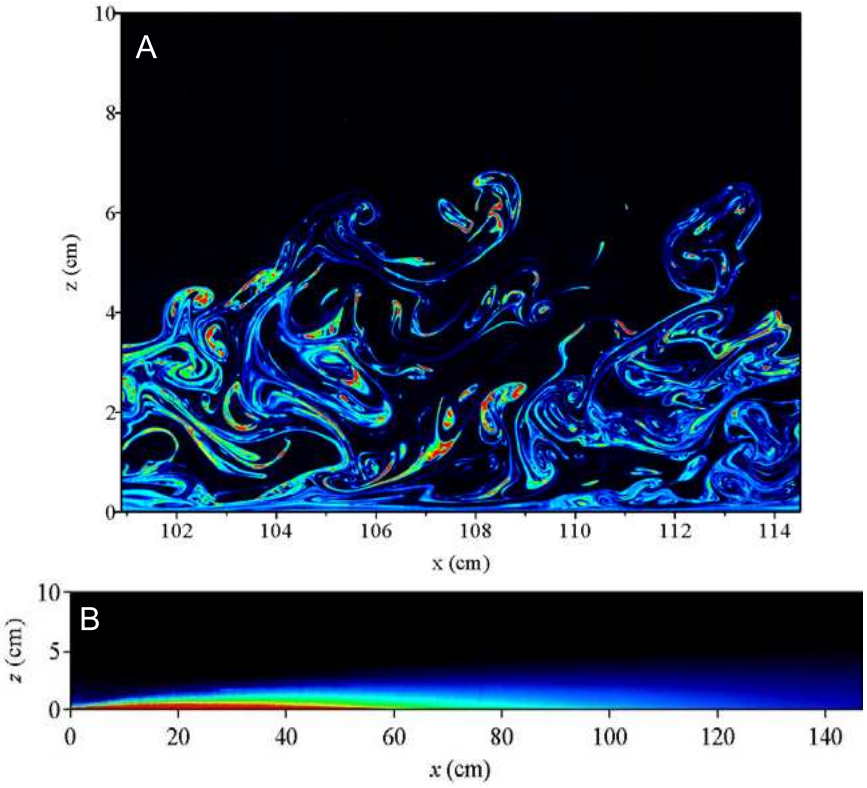


**Figure 1.1:** Laboratory flume experiment (Crimaldi and Koseff 2001) in which dye was released at the bed and advected to the right by turbulent flow while visualized in a vertical plane via planar laser induced fluorescence (PLIF). Color corresponds to dye concentration, where red is more concentrated and blue is less concentrated. (A) illustrates the instantaneous dye concentration field while (B) shows the time-averaged concentration field (note different fields of view and scales).

filaments contain fewer molecules (or less odorant mass) available for uptake farther from the source (Murlis et al. 1992). The odorant signal also becomes increasingly intermittent as the plume is transported downstream and laterally away from the source, and the durations of odor bursts and interburst periods are longer (Murlis 1997, Webster and Weissburg 2001). However, it must be noted that many of these fine-scale features still require long averaging periods (many filament samples) to fully converge statistically, making their usefulness to rapidly moving plume-tracking agents unclear (Webster and Weissburg 2001, Liao and Cowen 2002). Page et al (2011a) did recently find that peak filament concentration was well correlated with crab plume tracking progress, in a simple, binary above-threshold fashion. In addition, Liao and Cowen (2002) reiterated that intermittency was well correlated with lateral position and that the statistic did converge rapidly, indicating value in plume-tracking algorithms constrained by short sampling periods.

### Plume tracking behavior and algorithms

Critically important animal activities often involve tracking odors to a point source (Atema 1988), but how animals do this is generally poorly understood despite there being many studies on plume tracking behavior by terrestrial insects and marine crustaceans. An immediate distinction must be made between odor plumes in these two environments: because of differences in density, viscosity, and molecular diffusivity of odorants, plumes in air are typically much larger than the insects tracking them, while in water, a crustacean's two antennules could often span the entire width of the plume (Koehl 2006). The general strategies employed by animals in the two fluids are likely to be affected by this fundamental difference. Perhaps the most well studied creature is the moth: when tracking a pheremone plume in air, male moths fly upstream while they detect the odor, and if the signal is lost (i.e., they are no longer inside the plume) they employ a series of back and forth turns in the cross-stream direction (casting) until the trail is picked up again (David et al. 1983). Their algorithm does not and can not require information about fine-scale plume structure. In water, blue crabs appear to compare sensory inputs from the legs on either side of their wide bodies to determine position relative to the plume (Keller et al. 2003), and spiny lobsters may similarly compare the signals from their two long antennules (Reeder and Ache 1980), but the exact algorithms used by marine crustaceans are not nearly as well understood as in the case of the moth. This dissertation focuses on odorant detection in the marine environment, and thus on animals whose sensory appendages might measure fine-scale plume structure.

A variety of theories exist that attempt to explain plume tracking by lobsters, crabs, and other benthic crustaceans. As summarized by Grasso and Basil (2002), at one end of the spectrum is simple odor gated rheotaxis, in which an animal moves upstream as long as

sufficient odor is detected, and casts back and forth otherwise, as in a moth's behavior. At the other extreme lies eddy chemo-rheotaxis (Atema 1996), broadly defined as a method in which information coming from both fine-scale odor filament structure and the structure of eddies in the velocity field (i.e., "flavored eddies") is sampled, combined in some way, and used to guide navigation toward the source. While odor gated rheotaxis could be implemented with a single point probe measuring odor concentration and flow direction, eddy chemo-rheotaxis would require high resolution spatial sampling and complex neural processing ability. Several in-between algorithms of moderate complexity are reviewed by Grasso and Basil (2002) but much work needs to be done for a consensus of opinion, even for a single species under a single flow condtion, to be reached.

Unraveling biological plume-tracking behavior can be directly useful to some applications, such as maximizing the effectiveness of insect pest management using baited traps (Cooperband and Carde 2006, Bisignanesi and Borgas 2007) or, in the marine environment at a large scale, understanding how and where endangered or valuable fish (e.g., salmon) aggregate within plankton-rich riverine plumes (De Robertis et al. 2005). However, plume tracking research is much broader than this, as engineers have sought to replicate the outstanding success of animals by designing plume-sniffing and plume-tracking robots. Such robots have a wide range of applications, including risk assessment of water and air pollutant emissions, regulating releases of toxic substances, and finding sources of contaminants or unexploded ordnance. Applications of bio-inspired chemical sensing systems to national security (e.g., bomb sniffing) are particularly timely and are reviewed by Settles (2005).

Several wheeled robots have been used to test plume tracking algorthims in the terrestrial environment, albeit under very controlled conditions (Kazadi et al. 2000, Ishida et al. 2005, Martinez et al. 2006, Pyk et al. 2006, Harvey et al. 2008a;b). There have been fewer studies with underwater robots, with a "robot lobster" equipped with salinity sensors (Grasso et al. 2000) being one notable example. These robots typically employ either one or two chemical sensors, along with sensors that detect flow direction. As such, algorithms much simpler than eddy chemo-rheotaxis (that do not utilize fine-scale plume structure) are tested, and many do perform reasonably well given limitations such as slow response times. However, these robots have a long way to go before they achieve the performance of their biological counterparts, especially if the robot is not started within the plume or the plume is completely "lost" during tracking.

One important question not usually addressed by animal or robot studies is how the physical presence of the sensors affects the structure of the plume being sampled. The interaction between a chemosensory organ or device and a plume will affect how the plume is percieved, and what information is actually available to the plume-tracking agent. Physical signal filtering occurs before and in addition to any further processing by neurons or electronic

circuitry. In the case of marine crustaceans, the morphology of the sensory antennules is critical in understanding this first step.

## 1.1.2. Odorant detection by olfactory hair arrays

For macroscopic organisms, chemoreception is commonly thought of in terms of two activites: tasting and smelling. While the taste and smell organs are easily distinguished in humans, the entire bodies of marine crustaceans are adorned with a vast diversity of chemoreceptors that are all continuously exposed to the ambient fluid. Smelling then refers to the perception of odors at a distance versus when the animal is in close contact with the odor source, and is the sense of most interest here.

Aquatic malacostracan crustaceans (e.g., crayfish, crabs, mantis shrimp, lobsters) have a pair of antennules (not to be confused with the much longer antennae in lobsters) that serve as sensory appendages. In contrast to the mammalian nose, these organs act as movable external "noses" that are actively flicked through the water, intercepting and sampling patches of dissolved odorant in the environment. The antennules branch into filaments, and along one of the filaments are arrays of hair-like structures, the aesthetascs, that contain the dendrites of hundreds of olfactory neurons enclosed by a thin, permeable cuticle (Gleeson 1982, Spencer and Linberg 1986, Laverack 1988, Grunert and Ache 1988, Hallberg et al. 1992, Atema 1995, Mead and Weatherby 2002). Although there are many other chemosensory structures on the antennules and on the animals in general, the aesthetascs are the most well studied and play an important, though not crucial, role in olfaction-mediated behaviors such as plume tracking (Grasso and Basil 2002, Keller et al. 2003, Horner et al. 2004). A great diversity of aesthetasc array morphologies has evolved, as shown in Figure 1.2: e.g., the mantis shrimp *Gonodactylaceus falcatus* has relatively few, sparsely spaced aesthetascs, blue crabs (*Callinectes sapidus*) have toothbrush-like dense tufts of flexible aesthetascs on short antennules, and the spiny lobster *Panulirus argus* has a complex zig-zag arrangement of aesthetascs on long antennules. In each case, the entire structure encompasses a range of length scales, from the supporting antennule (mm's in diameter) to the individual aesthetascs (about 20 microns in diameter in *P. argus* (Goldman and Koehl 2001)).

### Importance of fluid dynamics

As an animal flicks its antennules, the "no-slip" condition dictates that the fluid velocity is zero along the entire surface of the antennule and individual aesthetascs, and the resulting boundary layers are thick relative to the size of the sensory hairs at the low Reynolds

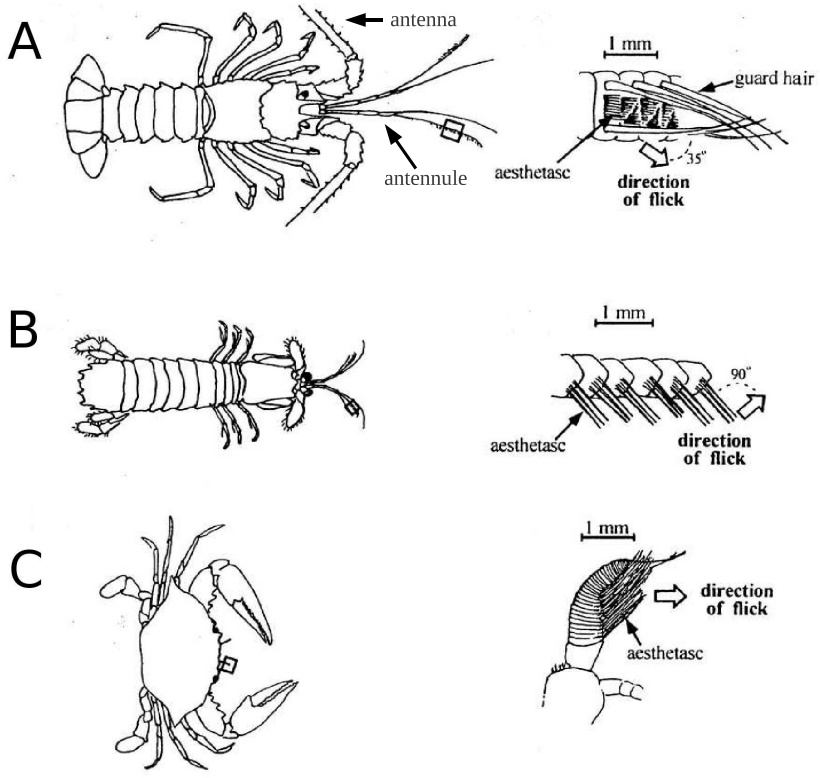


**Figure 1.2:** Antennule morphologies of the Florida spiny lobster *Panulirus argus* (A), mantis shrimp *Gonodactylus falcatus* (B), and blue crab *Callinectes sapidus* (C) (reprinted from Koehl 2001b). Diagrams at right are magnified views of the aesthetasc-bearing regions.

numbers ($Re's$) at which the hairs operate (Koehl 1996). The flow between the aesthetascs is laminar and transport of odorant molecules across streamlines occurs via molecular diffusion, though the antennule or aesthetasc array as a whole might enter a transitional flow regime in which vortex shedding occurs (Leonard 1992, Schuech unpublished).

When moving fluid encounters an array of cylindrical hairs of finite cross-stream width, some fluid will move through the array and the rest will move around the array. A non-obvious feature of crustacean aesthetasc arrays is their relatively large resistance to flow, and the corresponding propensity for water to travel around the structures instead of between individual microscopic hairs. Because the proportion of flow encountering the aesthetascs within an array is critical to its sampling performance, Cheer and Koehl (1987b) have defined a non-dimensional parameter, leakiness, to quantify it. Leakiness is defined as the volume of fluid that flows in between the elements of an array per unit time divided by the volume of fluid that would flow through the same area at the freestream velocity if no cylinders were present. Equivalently, leakiness can be defined as the ratio of the average fluid velocity in the gap between neighboring hairs to the freestream velocity. Leakiness summarizes the permeability of a cylinder array to flow as it is moved through the fluid during a sampling event. Therefore, leakiness determines how much passively transported odorant mass enters the array and is available for detection.

As mentioned earlier, several species of marine decapod crustacean, such as the mantis shrimp (*Gonodactylaceous falcatus*) and Florida spiny lobster (*Panulirus argus*), flick their antennules through the water (reviewed in Koehl 2006). Flicking reduces boundary layer thickness, increases leakiness (Koehl 1992, Mead and Koehl 2000, Koehl 2001b, Reidenbach et al. 2008), and facilitates odorant penetration into dense arrays of aesthetascs (Koehl et al. 2001, Mead et al. 2003). Furthermore, the movement is asymmetric: the faster downstroke or outstroke exhibits high leakiness while the slower return stroke and inter-flick pause exhibit low leakiness. This transition in flow regimes can critically affect the functioning of an olfactory appendage because odorant penetration into the hair array is greatly inhibited during times of low leakiness (Koehl et al. 2001). Since there is evidence that a new water sample is taken during the flick and retained within the aesthetasc array during the return stroke, antennule flicking seems to result in discrete odor sampling and has been likened to sniffing by mammals (Koehl 2001b).

Once odorant is inside the hair array, it must diffuse to the surfaces of the aesthetascs in order to be detected by the animal. However, this diffusion must only act over a short distance because advection is still usually the dominant mass transport mechanism: even during the slow return stroke, there is enough fluid movement that the Peclet number, which describes the relative importance of advection versus diffusion, is still much larger than 1 (Goldman and Koehl 2001). Only during the stationary pause between flicks is diffusion likely to dominate advection. Flicking therefore greatly decreases the distance that

odor molecules must diffuse, but simultaneously reduces the amount of time available for detection since it causes rapid advection of odorant patches out of the array - an important limitation discussed in detail in Chapter 2.

Flicking has another important effect on odorant detection. High fluid shear between aesthetascs is a necessary product of rapid flicking, since velocity is always constrained to be zero on each hair surface. Although it has been shown experimentally for *P. argus* that fine-scale plume structures can penetrate into an array of aesthetascs during the flick downstroke, those structures become distorted inside the array by the end of the flick due to this shear (Koehl 2001b). Little work has been done to examine this shear distortion, even though it may affect the information an animal may obtain from the plume. Chapter 2 of this dissertation focuses on distortion of plume structures as a function of array geometry and flicking speed.

### Neurobiology of odorant detection

Once odor molecules diffuse through the concentration boundary layer (e.g., Moore et al. 1991a) around an aesthetasc, they diffuse through the permeable cuticle into the lumen of the aesthetasc (e.g., Derby et al. 1997) and finally diffuse to and bind to receptor proteins on the outer dendritic segment of an olfactory neuron (e.g., Grunert and Ache 1988). Olfactory neuron response to odorant can be described as lying somewhere between two extremes: concentration detectors and flux detectors (Kaissling 1998): Concentration detectors are completely exposed to the fluid environment, and the effective chemical concentration at the receptor cell membrane is identical to that in the external fluid, while flux detectors are sheltered inside a perireceptor compartment in which stimulus molecules can accumulate and must be deactivated by the organism. While taste receptors are likely to be concentration detectors, Kaissling argues that odorant receptors, such as those inside crustacean aesthetascs, are probably closer in behavior to flux detectors (Kaissling 1998).

The work contained in this dissertation focuses on modeling aesthetascs as heavily simplified flux detectors. By assuming zero odorant concentration on the aesthetascs, we neglect any odorant accumulation, imagining that rapid and irreversible degradation of odorant molecules occurs. This boundary condition results in a time varying flux of odorant into the aesthetasc as an odor filament is sampled. This is an idealized sensory transduction process, in which the spatial structure of odorant concentration in the bulk fluid is transformed into time series of chemical flux to a number of detectors (cylindrical aesthetascs) arrayed in space. Properties of this transient signal may be important in determining both odorant quantity (e.g., concentration) and quality (i.e., the specific odor compound being smelled); such properties are discussed in detail in Chapter 2.

## 1.2. Highly relevant previous work

**In engineering** There is a vast body of engineering literature on scalar (usually heat) transport to single spheres and cylinders (Friedlander 1957, Acrivos and Taylor 1962) and arrays of these objects. However, most studies of cylinder arrays are focused on traditional engineering applications and are not applicable to biological aesthetasc arrays. Many investigate geometries clearly inappropriate to biological antennae (e.g., arrays of very long or infinite extent in the streamwise direction (Tamada and Fujikawa 1959, Stanescu et al. 1996, Yoo et al. 2007), and flow at moderate to high Reynolds number ($Re$) (e.g., (Chatterjee et al. 2009, Han et al. 2010)), whereas biological olfactory hairs operate at $Re's$ of $10^{-1}$ – 1 (e.g., Loudon and Koehl 2000, Goldman and Patek 2002, Koehl 2004). Furthermore, engineering studies often focus on physical processes that are not relevant to odorant detection such as conjugate heat transfer or buoyant effects (e.g., Wang and Georgiadis 1996, Lange et al. 1998, Juncu 2008). Finally, nearly all these studies involve steady state scalar transport, whereas sampling a turbulent plume is an unsteady process. However, in Chapter 2 we do compare our results to the analytical solution of steady scalar flux to a single cylinder, given by Friedlander (1957).

**In biology** There have been a number of studies in the biological literature directly geared toward understanding the fluid dynamics of hair-bearing appendages such aesthetasc-bearing antennules. The analytical model of Cheer and Koehl (1987b) was used to solve for the fluid velocity field around two cylinders in cross flow over a large range of $Re$ and $G/D$ (gap to diameter ratio). They found that both $Re$ and $G/D$ were important in determining the leakiness of a two-cylinder array, in a codependent matter (e.g., $G/D$ does not matter much at high $Re$). Most importantly, they showed that leakiness varied over orders of magnitude throughout a biologically relevant parameter space, so that whether a given appendage behaves as a leaky sieve or solid paddle depends on its morphology and movement speed. Later studies then expanded on this fundamental concept by including more cylinders or adding mass transport in addition to fluid flow.

Abdullah and Cheer (unpublished, described in Koehl 1992) numerically investigated the effects of additional cylinders in a row on leakiness by comparing two cylinders with a row of four cylinders, with intriguing results: at low $Re$ ($< 1$), adding hairs reduced leakiness, but at higher $Re$ ($> 1$), adding hairs increased leakiness. The reduction in leakiness at low $Re$ is in agreement with the work of Hansen and Tiselius (1992), who tested up to 12 cylinders and found a decrease in leakiness with additional cylinders at a $Re$ of 0.2. Hansen and Tiselius also found that the flow around the central cylinders changed little for rows of four cylinders or more, suggesting that asymptotic behavior is quickly reached. However, the relatively narrow parameter space investigated in these studies invites further research

into arrays of many cylinders. Chapter 3 details our results on arrays with many hairs and includes some comparisons with these studies.

Analytical solutions for flow and scalar transport become increasingly difficult as geometry becomes more complicated. Hence, Abdullah and Cheer used a numerical model and Hansen and Tiselius employed dynamically scaled physical models to determine flow patterns around more than two hairs. The use of the latter has been used extensively to study flow around hair bearing appendages because models can be made at a convenient size rather than the microscopic dimensions of the real structures (Koehl 2003). By matching the Reynolds number of the laboratory setup and the appendage in nature (often by using highly viscous fluids), the fundamental quality of the flow is preserved. Such physical models can be as complex as one's sculpting ability allows. Reidenbach et al (2008) constructed a model of a section of *P. argus* antennule, with its complex zig-zag arrangement of hairs, and measured the velocity field using particle image velocimetry (PIV). There is, however, a disadvantage to this research approach: because the diffusion of fluid momentum (kinematic viscosity $\approx 10^{-6}$ for water) is so different than that of mass (molecular diffusivity $\approx 10^{-9}$ for small molecules in water), it is not possible to dynamically scale both fluid flow and odorant transport simultaneously. Hence, these studies could only infer odorant sampling performance based on knowledge of the fluid flow.

In a hybrid approach, Stacey et al (2002) started with measured 2D velocity fields of the flow around dynamically scaled models of mantis shrimp (*G. falcatus*) antennules. They then post-processed the velocity fields to ensure mass conservation, and input the data into a numerical model of unsteady advection and diffusion of odorant to the aesthetascs. The overarching theme of this study was a comparison of juvenile to adult odorant sampling performance, and hypothetical cases of geometry and flicking kinematics based on these two life stages (e.g., adult geometry moved at the juvenile flicking speed). While directly showing that flicking greatly enhances exposure of aesthetascs to odorant, this work did not focus on studying a comprehensive parameter space, and the method employed had coarse spatial resolution relative to the size of the aesthetascs due to the experimentally measured velocity fields.

## 1.3. Overview of approaches

The objective of this dissertation is to quantify the effects of geometry and sampling kinematics on the odorant sampling performance of biologically-inspired sensor arrays. Our general approach uses computational fluid dynamics (CFD) software to solve the Navier Stokes equations that govern fluid flow around and the advection-diffusion equation that

governs odorant transport to idealized aesthetascs during an odorant sampling event. By solving for both velocity fields and odorant concentration fields numerically, spatial resolution is limited only by computational power, and geometry can be parameterized, quickly modified, and rerun. There are some disadvantages to this approach, however: creation of a suitable computational mesh for each major type of geometry is time consuming, and 3D simulations are not possible due to the much higher computational cost that would be involved. Still, the ability to simulate both flow and odorant transport simultaneously is a significant advantage of this method as compared to laboratory experiments with dynamically scaled physical models, for example.

This work first focuses on perhaps the simplest type of array possible: a single row of 2D cylindrical sensory hairs of infinite extent in the cross-stream direction. Since only one hair must be explicitly modeled with this simplification, computational costs are kept to a minimum. A very simple odorant plume composed of a single odorant filament, oriented parallel to the row, is intercepted by the hair array at a constant sampling speed. Aspects of geometry (i.e., diameter and gap spacing) and sampling speed were varied, and the effects on odorant flux were quantified. We focus on features of the flux time series that are likely to be neurobiologically important, as well as parameters that describe distortion of the flux signal relative to the original odorant filament. By holding leakiness constant, odorant penetration into the array is always maximal and the physics of odorant transport inside the array can therefore be isolated. This work, detailed in Chapter 2, provides a basis of fundamental behaviors with which we can intepret the results of more complicated geometries studied in later chapters. Chapter 2 is adapted from material that is currently in press.

Then another variable is introduced, the number of hairs, and its effect on the sampling performance of finite-extent arrays of variable leakiness is examined. This adds computational cost, but the addition of leakiness is an important step towards accounting for the complexity of real arrays because it allows an olfactory hair array to take discrete samples, or "sniff." Here, the main focus was on the number of hairs (or array width), since little is known about its effects on leakiness or odorant capture, and it varies widely from tens to thousands of hairs in different species. While simulations of infinite arrays assume that all hairs behave identically, models of finite-width arrays can also reveal variability in sampling performance across the appendage. This work on finite arrays, detailed in Chapter 3, will form a self-contained publication that is currently in preparation.

Lastly in Chapter 4, an in-depth study of an actual, highly complex morphology, that of the well-studied spiny lobster *P. argus*, is conducted. This work takes the form of morphological measurements of a real antennule specimen via state-of-the-art X-ray microtomography, as well as numerical simulations of a simplified version of its peculiar zig-zag aesthetasc array. While the simple geometries discussed above (2D rows of cylinders) can teach us about the fundamental characteristics of flow and scalar transport to hair-bearing appendages,

they are a far cry from reality, and it is difficult to guess whether they indeed capture all the important dynamics that occur *in situ*. The eventual use of real morphology in 3D simulations of flow and odorant transport will help answer this question, and to this end, an algorithm is developed to extract the surface morphology of hair-bearing appendages from 3D tomographic scan data. However, since 3D simulations of real morphology are extremely costly, 2D simulations of a V-shaped arrangement of cylinders similiar to the repeating subunits of the *P. argus* zig-zag morphology are a reasonable compromise. These simulations are used to test a hypothesis proposed in the literature that such morphology channels flow and odorant into the aesthetasc array.

# 2. Infinite Arrays

## 2.1. Introduction

### 2.1.1. Background

Scalar transport between small (sub-millimeter scale) cylinders or arrays of cylinders and the surrounding fluid is important in the modeling of many phenomena in biology and engineering, such as filters (Rubenstein and Koehl 1977, Kirsch 2007), artificial kidneys and lungs (Chan et al. 2006), and the hair-bearing appendages many animals use for environmental sensing (Koehl 1992). The work reported here is motivated by the use of small-scale arrays of cylindrical chemical sensors, in both engineered systems (i.e., artificial noses) and living organisms (i.e., olfactory antennules), to sense chemicals dispersed in the fluid environment.

Scalar quantities released into a typical environmental flow of air or water form spatially and temporally complex plumes. These turbulent plumes consist of concentrated filamentous structures interspersed with clean fluid (Crimaldi and Koseff 2001, Webster et al. 2003, Crimaldi and Koseff 2006). We focus on the physical design of odor-sensing antennae composed of hair-like chemical sensors, a design inspired by the olfactory antennules of marine crustaceans, in order to measure microscale chemical plume structure. Many of these olfactory antennules bear arrays of chemosensory hairs that might be used to to measure the spatial details of odorant patches in the environment (Koehl et al. 2001, Koehl 2006). However, using arrays of sensors to achieve this goal presents an apparent dilemma to both animals and robots: the size and spacing of sensors must be comparable to the spatial scale of the plume features of interest, but at small scales, the physical presence of the sensors distorts the surrounding plume due to viscous effects. Thus, our intent is to quantify how the physical filtering process of capturing odorant molecules from the ambient fluid filters the "odorant landscape" (Moore and Crimaldi 2004) observed by a plume-sampling agent.

Measurements of turbulent aquatic chemical plumes in the laboratory and environment have correlated the fine-scale structure (e.g., properties of individual chemical filaments)

adapted from a manuscript accepted to *Bioinspiration and Biomimetics*

of the plume at a point with relative source location (i.e., upstream and lateral distance) and type of source (e.g., continuous versus pulsed) (Moore and Atema 1991, Webster and Weissburg 2001, Crimaldi et al. 2002b, Keller and Weissburg 2004). Since many crustaceans track plumes too rapidly to rely on gradients of mean properties such as time-averaged concentration (Grasso and Basil 2002, Webster and Weissburg 2009), it has been suggested that their sensors must sample the instantaneous properties of an odorant plume (Atema 1985, Moore et al. 1991b, Weissburg and Zimmer-Faust 1993, Gomez et al. 1994, Zimmer-Faust et al. 1995, Koehl 2001a, Moore and Crimaldi 2004, Koehl 2006, Page et al. 2011a;b). Furthermore, many crustaceans "sniff," i.e., take discrete samples of the ambient water each time they flick an antennule. Flume experiments have shown that dye filaments in a turbulent plume can be captured within crustacean chemosensory hair arrays during a flick and retained there until the next flick (Koehl et al. 2001, Mead et al. 2003). However, which odorant filament properties (if any) are detected and utilized by an animal is an exceedingly difficult question to test via laboratory experiments because of the scale (tens of microns in diameter) of the chemosensory hairs.

Although arrays of sensing elements are often employed in the experimental design of artificial noses and tongues, it is typically in the context of using sensors with different chemical sensitivities in order to identify the sample, or discern odor quality. Indeed, such an ability is the contemporary definition of an "electronic nose." While determining odor quality is clearly very important (e.g., food engineering), only a few researchers have investigated using chemical sensor arrays to better characterize the detailed spatial structure of the plume, and additionally, discern properties of the source such as location or type of release (Kikas et al. 2001a;b, Cantor et al. 2008). For instance, Cantor et al (2008) showed experimentally that a group of sensors arrayed in space greatly increases the ability to characterize a modulated plume, such as that formed by a pulsed release or the wake of a nearby obstacle. It is unknown whether biological chemosensor arrays may be used in a similar fashion.

There is a vast body of engineering literature on flow around and scalar (usually heat) transport to cylinders and arrays of cylinders. However, most of these studies are focused on traditional engineering applications and are not very applicable to biological sensor arrays. Many investigate geometries inappropriate to biological antennae (e.g., arrays of very long or infinite extent in the streamwise direction as in Tamada and Fujikawa 1959, Stanescu et al. 1996, Yoo et al. 2007), and flow at moderate to high Reynolds number ($Re$) (e.g., Chatterjee et al. 2009, Han et al. 2010), whereas biological olfactory hairs operate at $Re's$ of $10^{-1} - 1$ (e.g., Loudon and Koehl (2000), Goldman and Patek (2002), Koehl (2004)). Other engineering studies often focus on physical processes that are not relevant to odorant detection such as conjugate heat transfer or buoyant effects (e.g., Wang and Georgiadis 1996, Lange et al. 1998, Juncu 2008). One exception is an analytical solution by Friedlander (1957) for scalar transport to a single sphere at low $Re$, which although steady-state,

is compared to our results in Section 2.3.2. It should be noted that dynamically scaled physical models of olfactory appendages (e.g., Reidenbach et al. 2008) have also proven useful, but practical requirements dictate that only the flow, not odorant transport, can be studied this way due to difficulties in scaling up both fluid momentum and scalar transport simultaneously.

To understand the fluid dynamics of odorant capture by crustacean antennules or biologically inspired artificial noses with small (tens of microns in diameter) hair-like sensors, a basic knowledge of the physical processes near the chemosensory hairs must be developed. This study focuses on perhaps the simplest type of sensor array and plume structure possible: an infinite row of 2D cylinders in low-$Re$ crossflow, sampling a single odorant filament. Using numerical methods, we examine odorant transport to the cylindrical flux-detecting sensors in an effort to describe how sampling performance is determined by array geometry and sampling kinematics (i.e., how fast the sensor array is moved through the ambient fluid). We have three main objectives that will help inform the design of biologically inspired chemical sensor arrays:

- Quantify the effects of sensor array geometry and plume sampling kinematics on distortion of the environmental odorant signal (Section 2.3.1)
- Quantify the effects of sensor array geometry and plume sampling kinematics on odorant flux metrics likely to be relevant to a plume sampling agent (Section 2.3.2)
- Apply these results to biological chemosensor arrays and discuss implications for bioinspired designs (Section 2.3.3)

### 2.1.2. Biological sensor arrays and flux metrics

Along one of the filaments of the antennules of many aquatic malacostracan crustaceans (e.g., crayfish, crabs, mantis shrimp, lobsters) are arrays of hair-like structures, the aesthetascs, that contain the dendrites of hundreds of olfactory neurons enclosed by a thin, permeable cuticle (Gleeson 1982, Spencer and Linberg 1986, Laverack 1988, Grunert and Ache 1988, Hallberg et al. 1992, Atema 1995, Mead and Weatherby 2002). Although there are many other chemosensory structures on these animals, the aesthetascs are the most well studied and play an important, though not crucial, role in olfaction-mediated behaviors such as plume tracking (Grasso and Basil 2002, Keller et al. 2003, Horner et al. 2004). A great diversity of aesthetasc array morphologies has evolved: e.g., the mantis shrimp *Gonodactylaceus falcatus* has relatively few, sparsely spaced aesthetascs, blue crabs (*Callinectes sapidus*) have toothbrush-like dense tufts of flexible aesthetascs on short antennules, and

the spiny lobster *Panulirus argus* has a complex zig-zag arrangement of aesthetascs on long antennules. In each case, the entire structure encompasses a range of length scales, from the supporting antennule (mm's in diameter) to the individual aesthetascs (20 microns in diameter in *P. argus* (Goldman and Koehl 2001)). The "no-slip" condition dictates that the fluid velocity is zero along the entire surface of the sensory appendage, and the resulting boundary layers are thick relative to the size of the sensory hairs at the low $Re's$ at which the hairs operate (Koehl 1996). The flow between the aesthetascs is laminar and transport across streamlines occurs via molecular diffusion.

All of these aesthetasc arrays consist of a finite (though sometimes very large) number of sensory hairs. Thus, water can flow both between hairs of the array and around the array as a whole. Cheer and Koehl (1987b) have quantified this flow feature with "leakiness," which is the ratio of the volume of fluid that flows between neighboring hairs in a unit of time to the volume of fluid that would flow through the same area if the hairs were not there. Equivalently, leakiness can be defined as the ratio of the average fluid velocity in the gap between neighboring hairs to the freestream velocity. Mathematical and physical models of flow through a variety of small-scale hair-bearing appendages have revealed that they often operate in a critical range of $Re$ where leakiness is very sensitive to morphology and sampling kinematics (Cheer and Koehl 1987a;b, Koehl 1995, Mead and Koehl 2000, Loudon and Koehl 2000, Koehl 2001a;b). At the lower end of this $Re$ range ($Re$ $10^{-2}$), the boundary layers around each hair are thick and overlapping, and the entire appendage behaves as a solid paddle of low leakiness. At the higher end ($Re$ 1), the boundary layers are thinner and the appendage behaves like a leaky sieve. This transition in flow regimes can critically affect the functioning of an olfactory appendage because it determines odorant access into the spaces between sensory hairs of the array (Loudon and Koehl 2000, Koehl et al. 2001, Stacey et al. 2002, Mead et al. 2003).

We modeled sensor arrays of infinite cross-stream extent, thus all the fluid must flow between the hairs of an infinitely wide row (it is maximally leaky). However, we matched properties of the flow between hairs of our infinitely wide rows to flow between real crustacean aesthetascs (see Section 2.2.5) in an effort to minimize errors inherent in an infinite array approximation to reality.

Crustaceans such as *P. argus*, *G. falcatus,* and *C. sapidus* flick the aesthetasc-bearing branch of their antennules back and forth through the water. In addition to the effects of sweeping through and sampling a two-dimensional region of the plume (Crimaldi et al. 2002a), flicking also increases leakiness (Koehl 1992, Mead and Koehl 2000, Koehl 2001b, Reidenbach et al. 2008) and facilitates odorant penetration into dense arrays of aesthetascs (Koehl et al. 2001, Mead et al. 2003, Koehl 2006). Furthermore, the movement is asymmetric: the faster downstroke or outstroke exhibits high leakiness while the slower return stroke and inter-flick pause exhibit low leakiness. This has the effect of replacing an old water sample with a new one

and then holding the new sample within the chemosensory array, a process likened to sniffing in mammals (reviewed in Koehl 2006). We modeled steady flow as a simplification of this behavior, focusing on the flow that occurs during mid-downstroke and mid-return, but discuss implications of our simple model on real sniffing behavior in Section 2.3.3.

During an odorant sampling event (a flick of the antennule through an odorant plume, e.g., Koehl et al. 2001), odorant molecules are transported via advection to the vicinity of an aesthetasc, reach the aesthetasc surface via molecular diffusion through the concentration boundary layer (e.g., Moore et al. 1991a), diffuse through the permeable cuticle into the lumen of the aesthetasc (e.g., Derby et al. 1997), and finally diffuse to and bind to receptor proteins on the outer dendritic segment of an olfactory neuron (e.g., Grunert and Ache 1988). We assume that these neurons act as odorant flux detectors such that that the rate of odorant molecule arrival to the receptors affects the signal that is output from the neuron, encoded as a series of action potentials or "spikes" (Kaissling 1998, Rospars et al. 2000). Thus, our principle interest is in the time-varying flux of odorant into an aesthetasc, integrated over the cylindrical aesthetasc surface. For simplicity, hereafter we refer to the surface-integrated quantity as "odorant flux." Although it is possible that variations in flux over a single aesthetasc might be percieved by animals, this seems unlikely due to neural convergence and we do not investigate such variation here even though engineered sensors might not have such limitations.

Neurobiological research has linked certain aspects of the time course of odorant molecule arrival at crustacean olfactory appendages with the firing of action potentials. Such experiments often delivered controlled pulses of odor-laden water to intact antennules or exposed axons of olfactory neurons in devices called "olfactometers" (Gomez and Atema 1994, Michel and Ache 1994, Hatt and Ache 1996, Gomez and Atema 1996b;a, Zettler and Atema 1999, Gomez et al. 1999). Increasing the concentration of odorant in a pulse increased the rate of neuron spiking and the number of spikes, and decreased the response latency (Gomez and Atema 1996a). If odorant arrival to aesthetascs is governed by advection and molecular diffusion (described by a linear partial differential equation), odorant pulse concentration is proportional to the flux to the aesthetascs, all other things being equal. Hence we take peak odorant flux during a sampling event to be an important metric of the flux time series. Lobster olfactory neurons also increase their spiking frequency as the rate of increase of odorant concentration near the aesthetascs (and thus onset slope of flux) is increased (Zettler and Atema 1999). We must note that the timescales in (Zettler and Atema 1999) were longer than the actual timescales of flux that we observe in this work, and there is evidence that onset slope might not be especially useful for plume tracking (Webster et al. 2001). However, we include peak onset slope in our analysis as a simple, representative aspect of transient sensor response, since it may be useful for odor quality determination (see below), and because similar quantities have been used successfully in plume tracking

robots (Ishida et al. 2005). Lastly, the olfactory receptors of crustaceans might need to interact with a certain number of odorant molecules in order to fire, analogous to the visual system requiring a certain number of photons (Barlow 1958, Hood and Grover 1974), although to our knowledge evidence of this has not yet been found in crustacean olfaction (Gomez and Atema 1996a). We include time-integrated flux, or total flux, in our analysis in light of this possibility as well as the fact that engineered chemical sensors might be designed with such properties.

While the ability of biological or electronic noses to measure microscale plume structure is a debated topic, it is clear that both systems must discriminate among different chemical compounds to be of great practical use. In electronic noses as well as the olfactory neurons of several animal species, the time courses of the response signals can be partially determined by chemical species (through the chemical kinetics occuring on and/or within the sensors) (Spors et al. 2006, Nakamoto and Ishida 2008, Junek et al. 2010, Su et al. 2011) in addition to the effects of fluid dynamics that we focus on in this work. Of particular note, mutant fruit flies with olfactory receptor neurons that express just one functional type of odorant receptor can still distinguish different odorants, presumably based on temporal response dynamics alone (DasGupta and Waddell 2008). Likewise, the utility of analyzing transient aspects of sensor response to help discriminate odors is gaining recognition among electronic nose and tongue researchers (Amrani et al. 1997, Hines et al. 1999, Nakamoto and Ishida 2008, del Valle 2010). Hence, temporal parameters such as those we investigate here for flux detectors (peak flux, peak onset slope, total flux) may be important for both plume tracking and identification of an odor plume's chemical composition.

## 2.2. Methods

### 2.2.1. Numerics

#### Overview

We used numerical simulations to model the flow of water (viscosity $\nu \approx 10^{-6}\ \mathrm{m^2\,s^{-1}}$) around arrays of cylinders tens of microns in diameter, as well as the advection and diffusion of low molecular weight odorant molecules (molecular diffusivity $k_D \approx 10^{-9}\,\mathrm{m^2\,s^{-1}}$) to the cylinders, during a plume sampling event. Although it is possible to numerically model an array of sensors moving through water containing an odorant plume, it is typically much simpler to model the equivalent problem of water containing an odorant plume moving past

a stationary array of sensors. This allows the computational grid to remain fixed in time, and is the approach employed here.

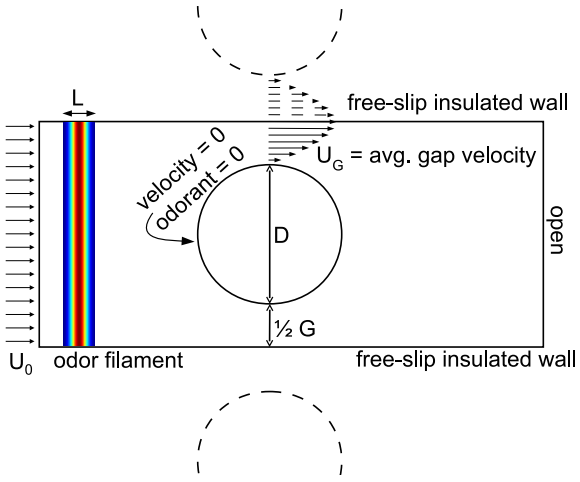


**Figure 2.1:** Schematic of geometry and boundary conditions. Items marked with dashed lines indicate neighboring subunits of the infinite array that are not explicitly modeled. The velocity profile in the gap is sketched. Domain length not to scale.

The arrays consisted of an infinitely long row of 2D cylinders, with various diameters and gap spacings. The steady fluid flow field for such geometry is set by a Reynolds number (we use $Re_{U_G,G}$, based on average gap velocity $U_G$ and gap length $G$) and the gap to diameter ratio $G/D$ of the array; see Section 2.2.5 for details of our parameter space. Besides simplifying the interpretation of flux results since there are no array edge effects, such simple geometry is also computationally easy because an infinite array of cylinders can be represented numerically with just one cylinder in the computational domain. Figure 2.1 illustrates the computational unit. By using appropriate boundary conditions, symmetry of the flow and odorant concentration fields on both sides is enforced, thus being equivalent to that in an array of infinite extent.

### Boundary and initial conditions

At the inflow face of the computational domain (see Figure 2.1), we use a Dirichlet condition for velocity, specifying a constant flow speed equal to the sampling speed of the array through the water. We use a time-varying Dirichlet condition for odorant concentration to advect a Gaussian-shaped odorant filament into the domain. We start with the ideal solution for a

point mass $M$ of odorant released at a point $x_0$ at time $t_0$ (far upstream of the computational domain) in an unbounded domain with uniform fluid velocity (i.e., sampling speed in the reference frame of the array) $U_0$ (Fischer et al. 1979):

$$C(x,t) = \frac{M}{\sqrt{4\pi k_D(t-t_0)}} \exp\left\{-\frac{[x-x_0-U_0(t-t_0)]^2}{4k_D(t-t_0)}\right\} \tag{2.1}$$

The parameters $x_0$, $t_0$, and $M$ are determined by enforcing that for every simulation, the odorant filament has the same width $L$ and peak concentration $C_0$ when its center reaches the leading edge of the cylinder in the case that it is undisturbed by the cylinder, i.e. equation 2.1. This standardizes the filaments over the varying sampling velocities and domain sizes we used and accounts for diffusion of the filament before it reaches the array. The peak concentration of the filament was arbitrarily chosen to be $C_0 = 1$ mg $\mathrm{L}^{-1}$, since the solution of the linear advection-diffusion equation will simply scale with this value, and the filament was chosen to be $L = 0.56$ mm wide (we assume "width" to equal the smallest interval that contains 95% of the total odorant mass in the filament; this corresponds to a filament standard deviation $\sigma_{filament} = 0.14$ mm). This is in the same range as the 1 mm wide odor filaments used in a previous study of mantis shrimp odorant capture (Stacey et al. 2002), although odorant patches in water as small as 0.2 mm have been measured (Moore et al. 1992).

To reduce numerical errors associated with spatial and temporal discontinuities of concentration, we modify the odorant filament specified by equation 2.1 and replace the infinitely long tails with linear tails that drop off to exactly zero over a finite distance. This hybrid shape is determined by setting 99.9% of the mass in the odorant filament to be within the Gaussian core, and the remaining 0.1% to be in the linear tails. Thus, the resulting piecewise function varies from zero to linear to Gaussian from left to right toward the filament center; it is not explicitly given here. This "Gaussian-linear" function is evaluated at the inflow domain face to specify the odorant concentration boundary condition over time. Although there is a slope discontinuity where the Gaussian core meets the linear tails, this appears to be insignificant in practice because both the concentration and slope are nearly zero at these locations.

The outflow face is "open," with a viscous stress and stream-wise scalar gradient of zero imposed. Since this boundary condition forces gradients to be zero which may not be zero in a real unbounded domain, we carefully studied the effect of the proximity of the outflow face to the cylinder and ensured enough downstream distance was present for the solution to develop properly (see Section 2.2.3).

The side faces of the domain are slip walls: no flux of odorant or water is permitted through the wall, but velocity parallel to the wall is not constrained to be zero as would be the case with a real wall. Since there are planes of symmetry in the middle of every gap of an infinite array, the cross-stream gradient of any quantity along such planes is zero, as if there were slip walls present. Hence, the distance from the edge of the cylinder to the slip wall of our domain is equal to half the gap distance $G$ of the infinite array we are modeling.

On the cylindrical sensor, we use a no-slip zero velocity condition for flow. This study focuses on the physical processes governing odorant molecule arrival at the aesthetasc surface, and consequently we idealize the processes thereafter. Thus, we employ a Dirichlet condition for odorant at the cylinder surface, and set concentration to zero for all time. This results in a diffusive flux of odorant into the cylinder, which is recorded as the simulation progresses. This boundary condition models an ideal flux detector, which immediately and irrevocably consumes all odorant molecules that arrive on it, perhaps by rapid enzymatic degradation (Trapido-Rosenthal et al. 1987, Carr et al. 1990). We believe this to be a more appropriate model of olfactory sensors than the other straightforward alternative, a Neuman boundary condition, in which concentration would be measured instead of flux (Kaissling 1998, Rospars et al. 2000).

The initial condition for velocity is computed as a potential flow solution, and the initial condition for concentration is zero everywhere, since initially the odorant filament is located far upstream of the computational domain. As the velocity field "spins up" to the correct viscous, steady state field, the odorant filament hypothetically diffuses and advects toward the cylinder according to equation 2.1. The parameters of equation 2.1 and the final Gaussian-linear approximation are chosen such that the leading edge of the incoming linear tail of the odorant filament reaches the inflow face when the velocity field reaches steady state. To determine an acceptable velocity steady state, we introduce a second, independent scalar specifically for this purpose. The boundary and initial conditions for this scalar are the same as for the odorant, except that the inflow boundary condition is a constant concentration equal to 1 $\mathrm{mg\,L^{-1}}$. Hence, this scalar advects into the empty domain as soon as the simulation begins, and eventually reaches the vicinity of the cylinder and begins to flux into it. When this flux stabilizes to two significant digits, the velocity field is assumed to be sufficiently steady and the odorant filament begins entering the domain. The convenience scalar is used since it allows a direct estimate of the effects of flow unsteadiness on odorant flux.

### Numerical method

The numerical method we use (Barad et al. 2009) solves the incompressible Navier Stokes equations for fluid motion and the scalar advection-diffusion equation for scalar transport.

The method couples the embedded-boundary (or cut-cell) method for complex geometry with block-structured adaptive mesh refinement (AMR) while maintaining conservation and second-order accuracy. These features allow us to accurately resolve the scalar flux to the cylinders while using domains large enough to make boundary effects insignificant. For our simulations, adaptive mesh refinement over time was not necessary, but local refinement around the cylinder was used to obtain accurate odorant fluxes (Figure 2.2). To calculate time-varying odorant flux into the embedded-boundary of the cylinder, the finite-volume based code computes a mass flow rate across the boundary for each Cartesian-cell cut by the cylinder (see Barad et al. 2009 for details), and then sums these contributions to obtain the spatially integrated flux into the cylinder, per unit length in the third dimension.

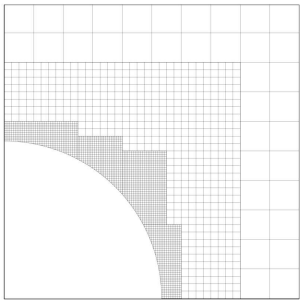

**Figure 2.2:** Section of a typical computational grid ($Re_{U_G,G} = 3$, $G/D = 2$) illustrating local refinement near the cylinder surface.

## 2.2.2. Sample output and shape parameters

### Velocity field

Figure 2.3 shows a typical steady state velocity field. Note the relatively thick laminar boundary layer around the cylinder, and maximal velocities at the midpoints between cylinders (at the slip walls). The flow field is slightly asymmetric in the stream-wise direction due to the non-negligible advective terms in the Navier-Stokes equations, which would be disregarded in a creeping flow regime. Since the array is of infinite extent, all flow is forced through the gaps and the peak speed in the gap in this case is about double the inflow velocity.

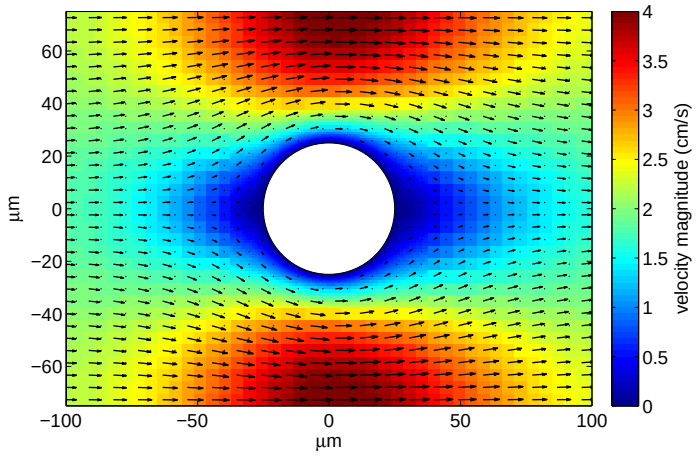


**Figure 2.3:** Velocity vector field and false color rendering of velocity magnitude (speed) in the vicinity of a cylinder in the array for $Re_{U_G,G} = 3$, $G/D = 2$. No smoothing of the color rendering has been done to show resolution of nested grids. Only a short stream-wise section of the computational domain is shown for clarity.

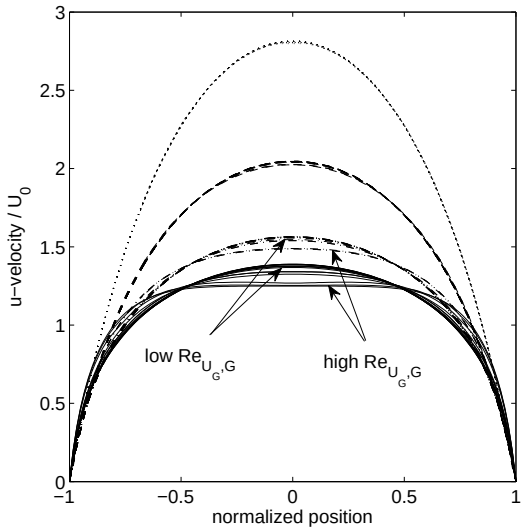


**Figure 2.4:** Profiles of normalized stream-wise velocity component versus normalized position in gap for all $Re_{U_G,G}$ and $G/D$ studied. Most profiles collapse onto four groups of curves corresponding to $G/D$ and are independent of $Re_{U_G,G}$, except where noted. dotted = $G/D$ 1, dashed = $G/D$ 2, dash-dot = $G/D$ 5, solid = $G/D$ 10

Figure 2.4 summarizes velocity profiles of the stream-wise velocity component within the gap

for the parameter space we investigated. The flow speed is normalized by the inflow velocity $U_0$ and plotted versus normalized position, which varies from -1 to 1 between the cylinders. While the normalized velocity profile only depends on $G/D$ at low $G/D$ (curves for different $Re_{U_G,G}$ collapse), at high $G/D$ the shape of the profile becomes dependent on both $Re_{U_G,G}$ and $G/D$. In the limit of high $Re$ (but still laminar flow), we'd expect boundary layers to shrink and the interactions between cylinders to disappear. In this limit, normalized velocity in the gap center would approach unity and the velocity profile would resemble the superposition of the profiles for two non-interacting cylinders. That is, a peak would occur near each cylinder surface due to the velocity speedup that occurs even for flow around an isolated cylinder, forming double-peaked velocity profiles in the gaps of the array. At the highest $G/D$ we studied, this is beginning to happen as the boundary layers around the neighboring cylinders become distinct instead of merged. Thus, for this parameter space, the velocity field between closely spaced cylinders exhibits fully overlapping boundary layers and velocity profiles proportional to $U_0$, while the flow fields for the highest $G/D$ we studied entered a different flow regime with a region of nearly constant velocity and low shear in the middle of the gap, and an increasing dependence on $Re_{U_G,G}$.

### Odorant concentration field

A representative series of odorant field snapshots is shown in Figure 2.5, from when the odorant filament first reaches the array to when the bulk of the filament has advected far beyond the array. High shear in the velocity field in the gap causes the filament to "bend" around each cylinder of the array, distorting it significantly and transforming the streamwise concentration gradient in the original filament to a cross-stream gradient within the gap. Concentration profiles in the gap over time are shown in Figure 2.6. As the filament enters the gap, the profile is single-peaked, but because odorant becomes trapped in the boundary layers around the cylinders, it develops a double-peaked shape as the bulk of the filament advects past the array. The peaks near the sensors then diminish due to both odorant flux and slow but persistent advection within the boundary layer.

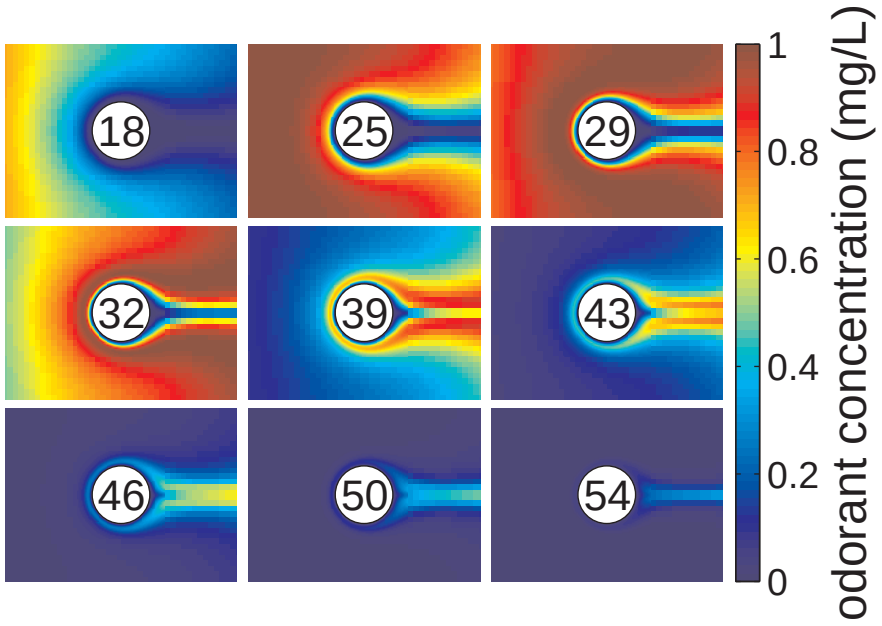


**Figure 2.5:** False-color renderings of odorant concentration in the vicinity of a cylinder in the array at consecutive times indicated by values inside circles (milliseconds) for $Re_{U_G,G} = 3$ ($U_0 = 2$ cm/s), $G/D = 2$, $D/L = 0.089$. Spatial scale is the same as Figure 2.3, with $D = 50$ $\mu$m and $L = 0.56$ mm.

Concentration profiles for several other $Re_{U_G,G}$, $G/D$, and $D/L$ are shown in Figure 2.7, all at times near when peak flux occured (concentration field output was not saved exactly when peak flux occured for all simulations). The profiles are double peaked for all cases except the lowest $Re_{U_G,G}$ tested ($Re_{U_G,G} = 0.06$), in which the gap velocity is slow enough that most of the odorant filament is still in the gap when peak flux occurs. Concentration boundary layer thickiness, defined as the distance from the cylinder surface to where concentration equals 99% of the instantaneous peak value in the gap, reaches 78% to the center of the gap in this case. This indicates that at very low $Re_{U_G,G}$, such as that of a *P. argus* return stroke (Table 2.1), chemical interactions between odorant molecules and the aesthetasc cuticle are likely to extend significantly into the gaps between hairs.

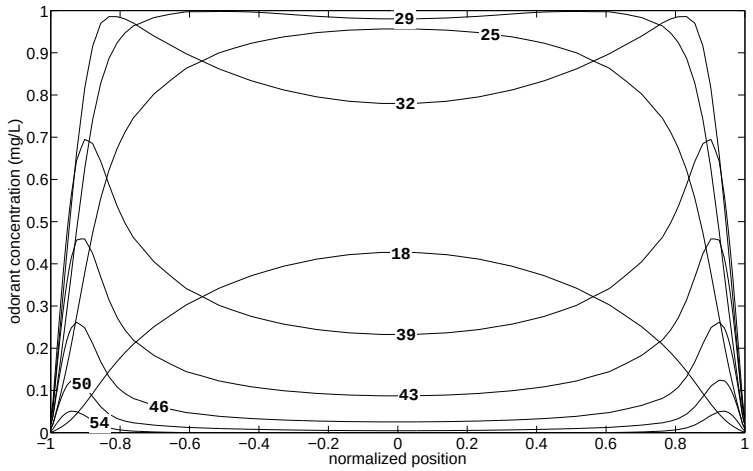


**Figure 2.6:** Odorant concentration profiles over time across the gap for $Re_{U_G,G} = 3$ ($U_0 =$ 2 cm/s), $G/D = 2$, $D/L = 0.089$. Labeled times (milliseconds) correspond to those in Figure 2.5.

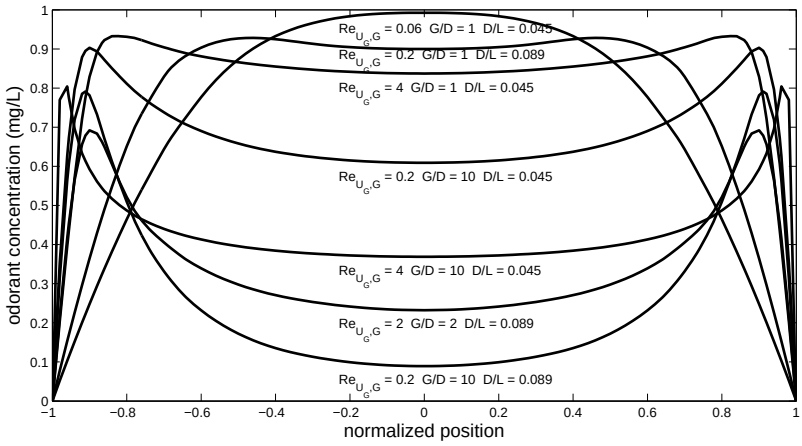


**Figure 2.7:** Odorant concentration profiles across the gap for various $Re_{U_G,G}$, $G/D$, and $D/L$ (labeled below each curve) at times near to when peak flux occured, where "near" is defined as within the smallest time interval that contains 33% of the total flux $F_{total}$ for each simulation.

The corresponding time series of odorant flux into a cylinder of the array is shown in Figure 2.8. For comparison, a hypothetical time series of odorant concentration at the leading edge of the array is also shown, determined from equation 2.1 as if the array were not there. In

Figures 2.5, 2.6, and 2.8, time has been shifted so that t = 0 corresponds to when the leading edge of the undisturbed odor filament reaches the leading edge of the array. The shape of the flux time series is very nearly Gaussian like that of the odorant filament being sampled. However, the flux time series is slightly wider than the concentration time series and there is a slight amount of asymmetry around the centroid (not present in the undisturbed odorant filament or hypothetical concentration time series), with slightly more odorant mass under the right tail than the left. Note too the ~10 ms lag between concentration and flux due to the slow velocity boundary layer around the cylinder; peak odorant flux (shortly before the 5th pane, 39 ms, in Figure 2.5) occurs long after the concentration peak of the filament has passed by the cylinder.

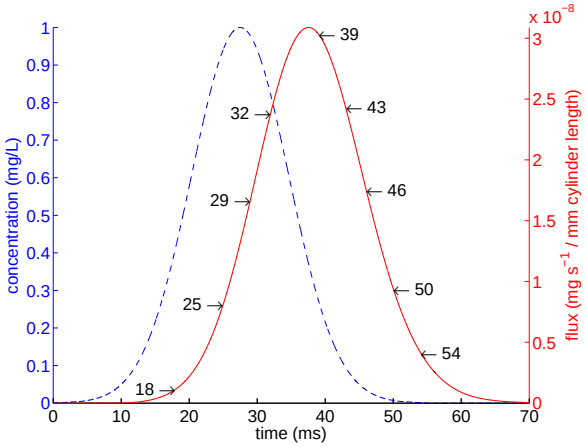


**Figure 2.8:** Time series of undisturbed odorant concentration at the cylinder's leading edge (dashed) and odorant flux into the cylinder (solid) for $Re_{U_G,G} = 3$ ($U_0 = 2$ cm/s), $G/D = 2$, $D/L = 0.089$ with marked times (milliseconds) corresponding to frames depicted in Figure 2.5.

### Flux time series shape parameters

The signal filtering characteristics of the sensor array are represented by the differences in shape of the unaltered incoming odorant filament and the flux time series output by the array. These shape differences are especially important if one's goal is to simply measure microscale plume structure (e.g., with field instrumentation). We focus on three dimensionless shape parameters: normalized duration (or width) $w^{norm}$, skewness, and excess kurtosis, to quantify these differences. The duration of the flux time series $w$ is defined as the smallest time interval that contains 95% of the total odorant flux (equation 2.2), and it is normalized to $w^{norm}$ by using free-stream velocity $U_0$ and filament width $w_{filament} =$

0.56 mm (equation 2.3); this essentially compares the temporal duration of the flux time series to the equivalent temporal duration of the undisturbed odorant filament as it advects past in the reference frame of the array. Skewness and kurtosis of the flux time series are determined by calculating normalized central moments of the flux time series $f(t)$ according to equations 2.4 and 2.5:

$$w = min(t_2 - t_1) \mid \int_{t_1}^{t_2} f(t)dt = 0.95(F_{total}) \tag{2.2}$$

$$w^{norm} = {}^{w}\!/_{(w_{filament}/U_0)} \tag{2.3}$$

$$skewness = \frac{\mu_3}{\sigma^3} \tag{2.4}$$

$$kurtosis = \frac{\mu_4}{\sigma^4} - 3 - \kappa_0 \tag{2.5}$$

where

$\mu_k = \frac{\int_{-\infty}^{\infty}(t-\mu)^k f(t)\,dt}{\int_{-\infty}^{\infty} f(t)\,dt}$

$\mu = \frac{\int_{-\infty}^{\infty} t\, f(t)\,dt}{\int_{-\infty}^{\infty} f(t)\,dt}$

$\sigma = \sqrt{\mu_2}$

The skewness of the incoming Gaussian-linear odorant filament is zero, since it is symmetric, and its excess kurtosis $\kappa_0$ is about 0.01 (above the kurtosis of a pure Gaussian, equal to 3) due to the finite linear tails. We normalize the excess kurtosis (shortened to "kurtosis" from here on) of the flux time series to that of the incoming filament by subtracting this preexisting (though very slight) kurtosis.

A simulation is ended when the flux of odorant into the cylinder (the time series in Figure 2.8) has become sufficiently small. In practice, we found that the higher moments of the flux time series, skewness and kurtosis, were very sensitive to the tails of this curve, and convergence of these parameters to a maximum of 10% error was the determining factor in how long a simulation was run for.

### 2.2.3. Calculation of flux metrics

In addition to the three time series shape parameters outlined in Section 2.2.2, we examine three metrics of flux, introduced in Section 2.1.2, that are more directly related to biological odorant detection: peak flux, peak onset slope (or simply peak slope), and time-integrated or total flux.

Peak flux is simply taken as the maximum value of the flux time-series (near t = 39 ms for the simulation in Figures 2.5, 2.6, and 2.8). Peak onset slope is estimated by calculating the time derivative of the flux time series using central differences, and taking the maximum of this approximate derivative. Peak onset slope occurs nearest to t = 29 ms for the simulation in Figures 2.5, 2.6, and 2.8. Total flux is calculated by integrating the flux time-series using the trapezoidal approximation. In the solver, a CFL condition due to the explicit hyperbolics limits the timestep to be very small relative to the timescale of flux variation, and flux data points are very closely spaced (e.g., 45000 data points in Figure 2.8). Hence, the errors due to the approximations used to calculate flux metrics are small compared to the error in the flux time series itself.

For the outer values of the parameter space we covered, convergence of the flux metrics (peak flux, peak onset slope, total flux) was investigated versus grid resolution at the finest level of local refinement near the cylinder and the number of cells in each dimension was doubled until a maximum of 10% difference between solutions was achieved. In addition to grid resolution, the effects of the inflow and outflow boundaries were tested. This is critical for low $Re$ flows, when boundary effects can be extremely large (Loudon et al. 1994, Lange et al. 1998). The domain length (in the streamwise direction) was repeatedly doubled until a maximum of 10% difference between solutions was achieved. Once sufficient grid resolutions and domain sizes were determined for the corners of the parameter space, the most conservative values were chosen for all other combinations of parameters.

### 2.2.4. Dimensionless groups

Here we present a dimensional analysis of this problem. The variables of interest are the three flux metrics:

| | |
|---|---|
| $F_{peak}$ | peak flux ($\mathrm{mg\,m^{-1}\,s^{-1}}$) |
| $F_{slope}$ | peak onset slope ($\mathrm{mg\,m^{-1}\,s^{-2}}$) |
| $F_{total}$ | time-integrated (total) flux ($\mathrm{mg\,m^{-1}}$) |

Each flux metric depends on the following seven independent variables:

| | |
|---|---|
| $U_0$ | inflow velocity ($\mathrm{m\,s^{-1}}$) |
| $D$ | cylinder diameter (m) |
| $G$ | gap between cylinders (m) |
| $\nu$ | kinematic viscosity of water ($\mathrm{m^2\,s^{-1}}$) |
| $k_D$ | molecular diffusivity of odorant in water ($\mathrm{m^2\,s^{-1}}$) |
| $C_0$ | peak concentration of odorant filament ($\mathrm{mg\,m^{-3}}$) |
| $L$ | width of odorant filament (m) |

Here we neglect the effect of approximating the Gaussian tails as linear, and assume the odorant filament's shape is determined solely by $C_0$ and $L$. Since neither $C_0$ or $L$ were varied in this work, odorant filament shape was constant in all simulations.

As each flux metric plus the seven variables that determine it sum to eight quantities consisting of three dimensional units (mass, length, time), five dimensionless groups are required to describe each flux metric. We choose the following normalizations to non-dimensionalize the flux metrics:

| | |
|---|---|
| $F^{norm}_{peak} = \frac{F_{peak}}{C_0 k_D}$ | normalized peak flux |
| $F^{norm}_{slope} = \frac{F_{slope} L^2}{C_0 k_D^2}$ | normalized peak slope |
| $F^{norm}_{total} = \frac{F_{total}}{C_0 L^2}$ | normalized time-integrated (total) flux |

And the following four dimensionless groups they depend on:

| | |
|---|---|
| $Pe_{U_G,G} = \frac{U_G G}{k_D}$ | gap-based Peclet number |
| $G/D$ | gap to diameter ratio |
| $D/L$ | sampling fraction |
| $\nu/k_D$ | Schmidt number |

The normalizations of the flux metrics are not intuitive, but were chosen for convenience: because we did not vary $C_0$, $k_D$, or $L$, the effect of our normalizations is simply to scale the dimensional flux metrics by the same amount across all simulations. If we had chosen a more intuitive set of normalizations that utilized parameters we did vary (e.g., $D$, $G$, $U_0$), our results would be framed in a different context as they would represent a comparison to another dynamically changing system (e.g., a type of virtual sensor) rather than mimicking the behavior of the dimensional flux metrics. Although comparisons to a virtual sensor can be useful since they normalize to theoretical limits, here we wanted to examine absolute performance. However, our normalizations come with the caveat that $C_0$, $k_D$, and $L$ *must be viewed as constants* when interpreting trends in $F^{norm}_{peak}$, $F^{norm}_{slope}$, and $F^{norm}_{total}$.

We use a gap-based Peclet number $Pe_{U_G,G}$ to describe how much advection dominates diffusion as odorant is transported within the array. We believe scaling with $U_G$ is more appropriate than $U_0$ since $U_G$ more directly describes the fluid dynamics near the sensors where flux takes place. For the infinite arrays studied here this seems especially appropriate because of the sometimes large increase in flow speed as fluid is forced through the array gaps. The choice of $G$ for a length scale is more arbitrary; $D$ may be equally appropriate. In addition to the relative importance of advection versus diffusion, $Pe_{U_G,G}$ can also describe the interactions between cylinders. When $Pe_{U_G,G}$ is maximized via $U_G$ and $G$, there is fast flow between distant cylinders, and when $Pe_{U_G,G}$ is minimized, there is slow flow between close cylinders. Hence, one would expect boundary layer interactions (concentration and momentum) between cylinders to be strong at low $Pe_{U_G,G}$ and weak at high $Pe_{U_G,G}$, given constant $\nu$ and $k_D$.

$G/D$ is an aspect ratio describing how sparse the array of sensors is, and like $Pe_{U_G,G}$, describes the interactions between cylinders in the array. Dense arrays are expected to have overlapping boundary layers between cylinders, and as $G/D$ increases the interactions between cylinders diminish (see Figure 2.4). It is important to keep in mind that for infinite arrays, denser arrays sampling at the same speed experience higher fluid velocities in the gaps due to mass conservation, whereas denser finite arrays often experience lower gap velocities due to lower leakiness.

$D/L$ describes the size of the sensors compared to the thickness of the odorant filament. One interpretation of $D/L$ is the ratio of array volume to filament volume, or "sampling fraction." A high sampling fraction indicates that much or all of the odorant filament can fit within the gaps of the array, while a low sampling fraction indicates that only a small region of the filament is sampled at a given moment.

A similar dimensional analysis can be done for aspects of the fluid flow only, such as velocity profiles and shear rates. This would yield a Reynolds number $Re_{U_G,G}$ instead of $Pe_{U_G,G}$, and $G/D$ as the two governing groups.

Note that because we did not vary the Schmidt number ($Sc = 10^3$ for small molecules in seawater), $Pe_{U_G,G}$ and $Re_{U_G,G}$ always differ by a constant factor of 1000 and $Sc$ is omitted from the analysis from here on. More data would be needed to understand how the functional relationships presented in this work would change if the sensor arrays were operated in a different fluid such as air.

### 2.2.5. Parameter space

The objective of this work is to understand the effects of array geometry and sampling speed on the flux time series generated by the array. To this end, we varied the sampling speed $U_0$, the gap between sensors $G$, and the diameter of each sensor $D$. Parameter ranges we studied are summarized in Table 2.1 as "min tested" and "max tested," along with values known for two crustacean species, the mantis shrimp *G. Falcatus* (juvenile and adult) and spiny lobster *P. argus* (adult).

For an infinite array of cylinders, the average fluid speed in a gap can easily be determined in terms of the sampling speed from mass conservation:

$U_G = U_0 \left(1 + \frac{1}{G/D}\right)$

The average gap velocity $U_G$ of an infinite array is always higher than the gap velocity of a corresponding (same inflow velocity $U_0$ and $G/D$) finite length array. This causes the leakiness (see Section 2.1.2) of an infinite array, defined as $U_G/U_0 = 1 + \frac{1}{G/D}$, to always be greater than unity. Koehl and coworkers noted a parameter range ($Re_{U_0,D} = 10^{-2}$ – $10^1$ and $G/D = 1$ – 15) in which leakiness of finite length arrays varied strongly from about 0.06 – 0.95 (Koehl 1992; 1996). It is likely that scalar transport also varies strongly in this flow regime. Although infinite arrays cannot reproduce the low leakiness that finite arrays can exhibit, both geometries may experience similar local flow in the immediate vicinities of the cylinders, where flux occurs. To better match this local flow, one can use $Re_{U_G,G}$, based on flow between cylinders, instead of the traditional $Re_{U_0,D}$. Koehl et al's results can be converted by multiplying their reported leakiness, $Re_{U_0,D}$, and $G/D$ values to obtain $Re_{U_G,G}$. The critical parameter range of finite arrays is then predicted to be $Re_{U_G,G} = 10^{-3}$ – $10^1$. Here, we varied $G/D$ and $U_0$ to achieve $Re_{U_G,G}$ of 0.06 – 22 (Table 2.1), which falls within the predicted critical range of biological importance.

### 2.2.6. Curve fits

The shape parameters $w^{norm}$, skewness, and kurtosis and flux metrics $F^{norm}_{peak}$, $F^{norm}_{slope}$, and $F^{norm}_{total}$ were fit to the following five parameter power law function of $Pe_{U_G,G}$, $G/D$, and $D/L$ ($Sc$ is not included since it was not varied):

$$\text{fitted value} = M\left(Pe_{U_G,G}\right)^a \left({}^{G}/_{D}\right)^b \left({}^{D}/_{L}\right)^c + I \tag{2.6}$$

**Table 2.1:** Parameter ranges of this study and selected morphologies. An odorant filament width of $L = 0.56$ mm is assumed. Values for *G. Falcatus* based on measurements by Mead and Koehl (2000); $U_G$ calculated as leakiness $\cdot\ U_0$. Values for *P. argus* from measurements by Goldman and Koehl (2001) and Reidenbach et al. (2008). Parameters that differ between real, finite extent appendages (i.e., measurements) and our infinite array models are labeled as such.

| | $U_0$ ($\mathrm{cm\ s^{-1}}$) finite | $Re_{U_0,D}$ finite | $D$ ($\mu$m) | $G$ ($\mu$m) | $G/D$ | $U_G$ ($\mathrm{cm\ s^{-1}}$) | $Re_{U_G,G}$ | $U_0$ ($\mathrm{cm\ s^{-1}}$) infinite | $Re_{U_0,D}$ infinite | $Pe_{U_G,G}$ | $D/L$ |
|---|---|---|---|---|---|---|---|---|---|---|---|
| min tested | - | - | 10 | 10 | 1 | 0.24 | 0.06 | 0.12 | 0.03 | 60 | 0.018 |
| max tested | - | - | 50 | 500 | 10 | 40 | 22 | 20 | 2 | 22000 | 0.089 |
| | | | | | | | | | | | |
| *G. Falcatus* juvenile return | 1.2 | 0.12 | 10 | 103 | 10.3 | 0.3 | 0.32 | 0.27 | 0.027 | 319 | 0.018 |
| *G. Falcatus* juvenile flick | 2.5 | 0.26 | 10 | 103 | 10.3 | 1.5 | 1.6 | 1.4 | 0.014 | 1593 | 0.018 |
| *G. Falcatus* adult return | 3.9 | 0.80 | 20 | 96 | 4.8 | 0.98 | 0.96 | 0.81 | 0.16 | 965 | 0.036 |
| *G. Falcatus* adult flick | 7.8 | 1.6 | 20 | 96 | 4.8 | 3.5 | 3.5 | 2.9 | 0.58 | 3474 | 0.036 |
| *P. argus* adult return | 2 | 0.5 | 20 | 100 | 5 | 0.01 | 0.01 | 0.0083 | 0.0017 | 10 | 0.036 |
| *P. argus* adult flick | 9 | 2 | 20 | 100 | 5 | 0.24 | 0.24 | 0.20 | 0.040 | 240 | 0.036 |

The fits were performed in MATLAB (2010a, The Mathworks, Natick, MA) using the non-linear least-squares optimization function lsqnonlin() in the Optimization Toolbox. Since the magnitude of the flux metrics was typically about $10^{-8}$, to avoid numerical precision problems, the data were rescaled temporarily when necessary to perform the curve fitting. Since negative values for $F_{peak}^{norm}$, $F_{slope}^{norm}$, and $F_{total}^{norm}$ would be physically impossible, we constrained $I$ for these fits to be non-negative, but did not constrain $I$ for $w^{norm}$, skewness, or kurtosis.

### 2.2.7. Predictions for real olfactory appendages

Our model allows us to predict aspects of the signal distortion (i.e., $w^{norm}$, skewness, and kurtosis) introduced by real olfactory antennules. To mitigate the differences between our infinite array model and real finite arrays, we limited ourselves to species for which the gap velocity between aesthetascs is known or can be estimated from published data so that we could calculate the appropriate $Pe_{U_G,G}$. Gap velocities for the adult spiny lobster *P. argus* were obtained from measurements of velocity fields around the aesthetascs of physical models (Reidenbach et al. 2008), and for the juvenile and adult mantis shrimp *G. falcatus* by multiplying published leakiness and freestream velocity values, also obtained using physical models (Mead and Koehl 2000). We used these gap velocities together with published measurements of aesthetasc diameter and gap width (Mead et al. 1999, Goldman and Koehl 2001) to estimate $Pe_{U_G,G}$, $G/D$, and $D/L$ for these real olfactory hair arrays sampling a 0.56 mm odor filament. We then predicted the duration $w$ of the flux into aesthetascs during the rapid downstroke or outstroke using the power law equation for $w^{norm}$ described in Section 2.2.6 and the definition of $w^{norm}$ given in Section 2.2.2. Skewness and kurtosis for *P. argus* and *G. falcatus* inspired infinite arrays were also predicted using our curve fits.

## 2.3. Results and discussion

### 2.3.1. Flux time series distortion

The ranges of the flux time series shape parameters over our parameter space give an overview of the signal filtering properties of the sensor arrays. Normalized durations ($w^{norm}$) of the flux time series range from 1.0 – 1.5 over the parameter space we investigated (Table 2.2). Since the lower limit of $w^{norm}$ is not very different from unity, the effect of the array over this parameter range is to either broaden the sampled filament or leave its temporal width essentially unchanged. All skewness values of the flux time series are positive (range

2.9E-4 – 1.0, Table 2.2), indicating that the tail of the flux time series is always "heavier" than the lead-in to some degree. Kurtosis varies from nearly zero (minimum -0.08, Table 2.2) to higher than the nearly Gaussian odorant filament (maximum 2.9) at high $Pe_{U_G,G}$, $G/D$, and $D/L$. Thus although these arrays only seem capable of increasing the perceived width of the sampled filament, they can simultaneously make it appear more "peaked."

**Table 2.2:** Power law regressions of flux time series shape parameters and flux metrics. fitted value $= M\left(Pe_{U_G,G}\right)^a \left({}^{G}/_{D}\right)^b \left({}^{D}/_{L}\right)^c + I$ Ranges of predicted values across the parameter space are also given. $k_D$, $C_0$, and $L$ should be treated as constant due to our normalization method for the flux metrics.

| fitted value | $a$ | $b$ | $c$ | $M$ | $I$ | $R^2$ | min | max |
|---|---|---|---|---|---|---|---|---|
| $w^{norm}$ | 0.30 | 0.48 | 1.7 | 0.54 | 0.99 | 0.993 | 1.0 | 1.5 |
| skewness | 0.52 | 0.39 | 1.8 | 0.20 | -0.011 | 0.982 | 2.9E-4 | 1.0 |
| kurtosis | 0.93 | 0.27 | 2.2 | 0.033 | -0.091 | 0.984 | -0.08 | 2.9 |
| $F^{norm}_{peak}$ | 0.32 | -0.5 | -0.068 | 2.89 | 2.2E-14 | 0.992 | 9.6 | 52 |
| $F^{norm}_{slope}$ | 1.3 | -1.2 | -1.1 | 3.3 | 2.3E-10 | 0.997 | 2.1E4 | 1.4E7 |
| $F^{norm}_{total}$ | -0.68 | 0.26 | 0.99 | 4.4 | 2.4E-5 | 0.996 | 1.8E-4 | 0.013 |

The power laws summarized in Table 2.2 appear to fit the data well, with the lowest $R^2$ value being 0.982. The curve fits indicate that $w^{norm}$, skewness, and kurtosis all display direct relationships with $Pe_{U_G,G}$, $G/D$, and $D/L$. All three shape parameters are most sensitive to the sampling fraction $D/L$ with approximately quadratic dependence, indicating that for flux time series shape, the interplay between array geometry and filament structure is more important than parameters only describing the sensor array ($Pe_{U_G,G}$ and $G/D$). This is consistent with the ability of these arrays to sample fine scale plume structure, since a strong relationship between plume structure and the flux time series would be necessary to do so, as opposed to the flux time series being mostly determined by the properties of the array alone.

As an odorant filament is advected through the array, a portion of odorant mass appears to become trapped in the low-velocity boundary layer around each cylinder of the array (Figure 2.3) for a relatively long period of time (Figure 2.5). Hold-up of odorant could cause the delay in peak flux, broad width, and positive skewness we often see in the flux signal. Our flux time series, which would always be essentially Gaussian if not for the physical presence of the array, bear some resemblance to concentration time series measured at a point in many tracer release experiments, in both laminar and turbulent shear flows, that are designed to test theories of shear (Taylor) dispersion (Young and Jones 1991). In these studies, the unexpected skewness is often attributed to scalar trapping in the viscous

sublayer near boundaries or dead-zones in the flow such that insufficient time has occurred for complete transverse mixing, violating a necessary condition for Taylor's approximation. We can make a similar argument here: If the time required for odorant molecules to traverse the gap via diffusion was very small compared to their residence time within the gap, then we would expect a Gaussian-shaped flux time series, as the array would act as a rapid and complete sink for the incoming Gaussian concentration profile. However, if we take the ratio of odorant residence time $D/U_G$ to the diffusion timescale $\left(\frac{1}{2}G\right)^2/k_D$ (this ratio is equivalent to $4\left(Pe_{U_G,G}\right)^{-1}\left(G/D\right)^{-1}$), we find that this quantity is indeed much less than unity for our entire parameter space (max 0.07). This indicates that transverse mixing via diffusion in the gap is by no means complete. Instead, a large fraction of odorant mass appears to pass through the gap un-sensed, while the remainder is trapped in the boundary layer around and directly behind each cylinder and diffuses inside.

### 2.3.2. Flux metrics

Table 2.2 summarizes the power law fits of $F^{norm}_{peak}$, $F^{norm}_{slope}$, and $F^{norm}_{total}$ to $Pe_{U_G,G}$ and $G/D$ and $D/L$, with excellent fits indicated by the high $R^2$ values. Interestingly, our dependence of $F^{norm}_{peak}$ on the Peclet number ($\propto Pe^{1/3}_{U_G,G}$) is the same as the dependence of steady state scalar flux on $Pe$ for an isolated sphere at $Re = 0.1$, given by Friedlander (1957). This suggests that a pseudo-steady state approximation might be valid for the case of unsteady sampling of an odorant filament, since a 0.56 mm filament is much larger than 10 - 50 $\mu$m aesthetascs.

The exponents in Table 2.2 indicate that $F^{norm}_{peak}$ and $F^{norm}_{slope}$ both increase with $Pe_{U_G,G}$ and decrease with $G/D$ and $D/L$, with the strength of the dependencies being higher for $F^{norm}_{slope}$ than for $F^{norm}_{peak}$. Peak slope is intuitively expected to be more sensitive than peak flux because it is a property of the derivative of the flux time series versus the time series itself. $F^{norm}_{total}$ displays the opposite trends, decreasing with $Pe_{U_G,G}$ and increasing with $G/D$ and $D/L$. The physical interpretations of the non-dimensional groups can help explain these trends, although we caution that due to our normalization method (Section 2.2.4), $k_D$, $C_0$, and $L$ should be treated as constants. In particular, $D/L$ should be interpreted as the effect of varying $D$ only so that trends in $F^{norm}_{peak}$, $F^{norm}_{slope}$, and $F^{norm}_{total}$ accurately represent trends in the absolute performance metrics $F_{peak}$, $F_{slope}$, and $F_{total}$.

The gap Peclet number $Pe_{U_G,G}$ combines aspects of array geometry ($G$) and sampling kinematics ($U_G$) with scalar diffusivity ($k_D$) to represent the relative importance of advective to diffusive transport of odorant within the array. Since $F^{norm}_{peak}$ and $F^{norm}_{slope}$ occur at instants in time, to obtain high values it is most important to bring the peak of the filament close to

the sensor surface, via advection, so that the final diffusive step may occur rapidly. Diffusive transport decreases peak slope and peak flux by smoothing peaks in the concentration field before they reach the sensor. This is in agreement with the experimental work by Moore et al (1991a) on the odorant sampling properties of the various chemosensory appendages of the clawed lobster *H. americanus*; slower flow in the immediate vicinity of the sensory hairs caused lower peak concentrations and larger widths of the odorant pulse they were exposed to compared to the original free-stream pulse. Oppositely, $F_{total}^{norm}$ is increased by a lower $Pe_{U_G,G}$ transport regime in which diffusion becomes more important. This is because signal smoothing is inconsequential to total flux, and the effects of diffusion integrated over the sampling event bring more odorant molecules to the sensor surface than would occur at high $Pe_{U_G,G}$.

$G/D$ represents the sparsity of an array of sensors. As seen in Figure 2.4, denser infinite arrays with low $G/D$ have generally steeper, more parabolic velocity profiles than sparse arrays, and achieve higher velocity speed-ups in the gap relative to the freestream velocity. Arrays at low $G/D$ experience a relatively high shear rate over most of the gap, causing the odorant filament to undergo more stretching around the sensors compared to arrays at high $G/D$. This moves more of the central odorant peak close to the sensor surfaces, resulting in the higher $F_{peak}^{norm}$ and $F_{slope}^{norm}$ that we see at low $G/D$. However, the higher shear at low $G/D$ also results in lower $F_{total}^{norm}$, a tradeoff for which we do not have a detailed explanation.

$D/L$, the sampling fraction, represents the ratio of sensor size, or streamwise array width, to filament width. The sampling fraction describes how much of the filament is sampled at any instant in time and the extent to which spatial integration over a sensor results in the loss of information contained in the plume structure. However, increasing $D/L$ via $D$ also acts to increase the surface area available for flux, allowing more odorant molecules to be captured. $D/L$ can thus describe a tradeoff between array surface area and signal smoothing. Consequently, $F_{peak}^{norm}$ displays only a slightly negative correlation with $D/L$, the effects of spatial integration largely offset by increased surface area. On the other hand, $F_{slope}^{norm}$ is somewhat decoupled from the magnitude of odorant flux since $F_{slope}^{norm}$ is a property of the time series's temporal derivative. Hence, surface area does not directly affect peak slope and it is inversely related to sampling fraction due to the signal smoothing effect. In contrast to the peak metrics, $F_{total}^{norm}$ increases with $D/L$ (i.e., as $D$ increases) because more odorant molecules in the filament can be captured at any moment (the filament becomes narrow relative to the array) and signal smoothing does not adversely impact $F_{total}^{norm}$ since it is a time-integrated quantity.

## 2.3.3. Application to real olfactory arrays

### Signal distortion

Table 2.3 summarizes the predicted flux time series shape parameters for the antennules of the spiny lobster *P. argus* and the juvenile and adult stages of the stomatopod *G. falcatus*. The normalized duration of flux $w^{norm}$ is nearly unity for all cases, indicating that these chemosensory hair arrays do not distort the observed temporal width of the filament. Similarly, the flux time series generated by these arrays are predicted to introduce almost no skewness or kurtosis compared to the original odorant filament shape. Even though the antennules of spiny lobsters and mantis shrimp distort the spatial structure of an odorant filament at the scale of the aesthetascs by physically intercepting it, the predicted flux time series is still an excellent representation of the filament's original structure. Thus, if low signal distortion is desired, the antennules of *P. argus* or *G. falcatus* seem to be reasonable starting points for the design of an artificial sensor array tasked with sampling small-scale turbulent plume structure in water.

The strongest predictor of signal distortion is $D/L$ (Section 2.3.1). Therefore, using very small sensors is expected, not surprisingly, to greatly enhance the ability of an artificial nose to measure fine-scale plume structure. Individual sensors as small as the Batchelor scale (the spatial scale of the smallest chemical fluctuations, $O(10\ \mu\text{m})$ in typical benthic boundary layer flows) are within reach given current technological trends (James et al. 2005).

### Flux metrics

To summarize the trends in Section 2.3.2, a high $Pe_{U_G,G}$, low $G/D$, low $D/L$ array will generate a sharp (high onset slope) time series with a high peak flux, but will detect fewer odorant molecules in total. This trade-off may have important neurobiological consequences, since olfactory neurons respond more strongly (i.e., exhibit higher spiking frequency) to more concentrated odorant pulses (Gomez and Atema 1996a) but likely also require a certain threshold $F_{total}$ to respond at all, though the threshold might be quite low. Similarly, Liao and Cowen (2002) suggest that the sensors of an engineered plume-tracing agent should be capable of sampling both sharp gradients and very low concentrations; our results suggest that these properties may be mutually exclusive.

Recently, Page et al (2011a) found that upstream movement by plume-tracking crabs is well predicted, in a binary fashion, by antennular encounters with peak odorant filament concentrations above a certain threshold. In our model of crustacean aesthetasc arrays, peak

flux of odorant into aesthetascs is proportional to peak concentration; hence, a high peak flux might be required for upstream movement. Although odorant flux is affected by both plume structure and how the plume is sampled, $F_{peak}^{norm}$ varies over less than an order of magnitude over our entire parameter space (Table 2.2) of array geometries and sampling speeds. The greater dependence of peak flux on $C_0$ (linear) than on array properties is echoed by the power law exponents for $F_{peak}^{norm}$ in Table 2.2, whose absolute values are all substantially less than unity. Furthermore, the minimum concentration in a turbulent plume is essentially zero, resulting in a huge dynamic range of sampled concentrations as an animal flicks its antennules. Peak flux may therefore be mostly determined by plume structure, and if it is only important in a binary fashion, an organism's (or robot's) plume tracking performance might not be sensitive to its precise morphology and sampling kinematics.

### Flux time series duration

The duration of the flux time series is an important quantity because it determines approximately how long olfactory neurons or chemical sensors are exposed to odorant during a sampling event. Here we focus on the biological implications with some concluding remarks on artificial systems.

Olfactory neurons require a certain period of stimulation to detect and quantify an odorant. For example, antennule olfactory neurons of *Homarus americanus*, the clawed lobster, need 50 ms of exposure to an odorant to detect it and 200 ms to measure its concentration (Gomez and Atema 1996a). On the other hand, adaptation (decreased response to the odorant) acts to diminish the effect of odorant flux at long exposure time; *H. americanus* olfactory neurons begin adapting to a stimulus in as little as 300 ms (Gomez and Atema 1996a). The relatively narrow range between the stimulus integration time of 200 ms and the beginning of adaptation at 300 ms means that lobster olfactory neurons may be tuned to a fairly precise duration of stimulation. Indeed, this time window matches the flicking frequency of *H. americanus* antennules, 4 – 5 Hz (Gomez and Atema 1996b).

Koehl et al showed that for a real *P. argus* antennule sampling a real turbulent dye plume, the spatial pattern of the chemical filaments in the aesthetasc array at the end of a flick is retained during the return stroke and inter-flick pause (Koehl 2001b). It has been hypothesized that in antennule-flicking crustaceans like lobsters, the slow return stroke and inter-flick pause enhance odorant flux by trapping odorant within the array and allowing more time for diffusion, and presumably stimulation of neurons, to occur (Mead et al. 1999, Mead and Koehl 2000, Goldman and Koehl 2001, Reidenbach et al. 2008). To investigate this idea, we predicted (see Section 2.2.7 for details) the durations of odorant flux, and thus neural stimulation, during the outstroke and downstroke of *G. falcatus* and *P. argus*,

respectively (Table 2.3). Note that predictions for *P. argus* are extrapolated outside the convex hull of our parameter space (*P. argus* was originally an end member of a parameter space based on $Re_{U_0,D}$). Also included in Table 2.3 are $w$ and $w^{norm}$ predicted by Stacey et al (2002), using velocity profiles measured around aesthetascs of dynamically-scaled physical models of antennules of *G. falcatus*. Values in Table 2.3 were visually estimated from plots of their flux time series. The differences between the predictions of Stacey et al and this study may be due to substantially different modeling approaches as well as our infinite array approximation. Although we define our *G. falcatus* and *P. argus* cases using $Re_{U_G,G}$ based on measurements in an attempt to account for differences in how infinite versus finite arrays operate (see Section 2.2.5), we are currently exploring these differences further with simulations of sensor arrays of finite extent.

**Table 2.3:** Predicted durations and shape parameters of flux time series for *P. argus* and *G. falcatus* during the rapid downstroke or outstroke, respectively, for both this study and the work of Stacey et al. (2002). Italicized values are extrapolated.

| | $w$ (ms) | $w^{norm}$ | skewness | kurtosis |
|---|---|---|---|---|
| Stacey et al | | | | |
| juvenile *G. falcatus* | 40 | 1.00 | NA | NA |
| adult *G. falcatus* | 12 | 0.94 | NA | NA |
| this study | | | | |
| juvenile *G. falcatus* | 41 | 1.0 | 0.0054 | -0.083 |
| adult *G. falcatus* | 20 | 1.0 | 0.053 | -0.026 |
| adult *P. argus* | 6.3 | *1.0* | *0.0091* | *-0.0864* |

Our results indicate that for a 0.56 mm odorant filament, it only takes about 6 ms for *P. argus* chemosensors sampling at the downstroke velocity to achieve maximum total flux (Table 2.3). For mantis shrimp we predict maximum total flux in 41 and 20 ms for juvenile and adult stages, respectively, while Stacey et al predict 40 and 12 ms. These flux durations are worth comparing to both the duration of the actual downstroke or outstroke movement, since this study and Stacey et al effectively assume an infinitely long sweep through the water but real flicks do not continue forever, and the stimulus integration times of olfactory neurons, as discussed above.

In reality, *P. argus* takes approximately 150 to 200 ms to complete the flick downstroke (Goldman and Koehl 2001), and *G. falcatus* (juvenile and adult) takes about 33 ms for the outstroke (Mead et al. 1999). Therefore, *P. argus* can certainly completely sample a 0.56 mm odorant filament during the downstroke, but in the case of *G. falcatus* the length of the downstroke may be limiting, especially for juveniles. Failure to intercept an entire odor filament would decrease total flux but not necessarily affect the ability to capture peak slope or peak flux.

Unfortunately there are no data on the stimulus integration times of *P. argus* or *G. falcatus* olfactory neurons, so we refer to the values for *H. americanus* here (i.e., 50 ms of stimulation needed for detection and 200 ms for quantification). These neural processing timescales are generally longer than the predicted flux durations for *G. falcatus* and especially *P. argus*. Therefore, the return stroke and inter-flick pause are indeed likely to be important to these animals by allowing ample time for neural stimulation to occur, as long as some odorant remains trapped in the array during these phases. The rapid advection of odor filaments through the aesthetasc arrays of *P. argus* and *G. falcatus* means that the width of a 0.56 mm odorant filament is unlikely to be measured via the duration of flux.

Over our entire parameter space, we observed flux durations ($w$) from 3 to 470 ms. Although the upper end is within the detection limits of crustacean olfactory neurons, we cannot predict leakiness with our infinite array model, and this is likely to be a critical factor in the performance of real sensor arrays as it determines how much of an odorant patch can enter a finite array. Since our arrays could only stretch the temporal width of the original odorant filament by a maximum factor of 1.5 (max $w^{norm}$, Table 2.2), the longer flux durations we observed were mainly due to slower sampling speeds than are the case for *P. argus* or *G. falcatus* flicks (e.g., 470 ms corresponds to the *P. argus* return stroke). We suspect that in reality, the cost of dramatically decreased odorant access at these sampling speeds would outweigh any advantage of increased flux duration.

It is useful to examine these flux durations in the context of diffusion of odorant through the aesthetasc cuticle. Although we assume a constant surface concentration of zero on each aesthetasc, it is likely that diffusion and/or consumption of odorant inside the aesthetasc will continue for some finite time. The diffusion depth for odorant into an aesthetasc is on the order of $\sqrt{2k_D t}$, assuming a diffusivity equal to that of odrant in water; diffusion through aesthetasc cuticle is likely to be slower than this estimate, and dependent on the molecular weight of the odorant (Derby et al. 1997). A flux duration of 3 ms (lowest across our parameter space) thus corresponds to a diffusion depth of about 2.4 $\mu$m while a flux duration of 470 ms (highest across our parameter space) corresponds to a diffusion depth of about 31 $\mu$m. Hence, since the cuticle is typically 0.5 - 1 $\mu$m thick (Grunert and Ache 1988, Mead and Weatherby 2002), odorant / dentritic receptor interactions don't seem to

be confined to either being purely surface phenomenon or volumetric phenomenon over a biologically relevant parameter space.

We focus on the information a plume tracking agent receives via the flux time series generated by the sensor array as a whole. However, odorant filament structure could also be inferred via spatial differences in flux throughout the array. For example, a filament's width could be estimated this way if it were oriented perpendicularly to the row of sensors. It is not known whether lobsters or mantis shrimp can use the spatial concentration distribution along an antennule to measure filament width; this depends in part on how signals from individual aesthetascs are aggregated via neural convergence. Nonetheless, in principle, a bio-inspired olfactory antennule could measure filament structure using both spatial and temporal information from its array of sensors.

The response times of most engineered chemical sensors currently in use are also too slow to resolve brief odorant bursts in either air or water (Ishida and Moriizumi 2004, Nakamoto and Ishida 2008, Vlasov et al. 2010). Hence, we face a similiar problem as crustaceans in translating temporal flux signals to high resolution odorant concentration maps, and analysis of spatial response data seems the more promising route if such maps are desired. The external location and morphology of olfactory antennules seems to facilitate spatial sampling, but artifical noses generally have a long way to go for this to be possible. The sampling systems of most electronic noses are quite ungainly, often employing separate "preconcentrators" that collect odorant mass from a bulk fluid sample and then relay it to the actual sensors (e.g., via adsorption and subsequent desorption) (Settles 2005). Not only are such sampling methods slow, but they obliterate any fine-scale plume structure. Crustacean aesthetasc arrays might be an elegant solution, as the sampling kinematics and dense hair spacing may faciliate odorant detection by slowly-responding sensors (via odorant trapping during the return stroke and pause), while the array-like morphology simultaneously may allow for direct spatial sampling.

## 2.4. Summary

To sample fine-scale turbulent plume structure using physical contact sensors, an array of closely spaced, small sensors is needed. However, as a small-scale sensor array samples a plume, the physical presence of the sensors necessarily results in distortion of the original plume structure. We found that signal distortion increases with each of the three dimensionless groups that characterize this problem ($Pe_{U_G,G}$, $G/D$, and $D/L$).

Flux-detecting olfactory sensors transduce spatial properties of odorant filaments into temporal properties of flux time series. We found that peak properties (peak flux, peak onset

slope) of the flux time series are maximized by advection-dominated transport (high $Pe_{U_G,G}$) between densely spaced (low $G/D$), thin (low $D/L$) sensors, while total flux is minimized by this sampling regime.

Since signal distortion is most sensitive to the sampling fraction $D/L$, flux-detecting chemical sensor arrays for use underwater should incorporate the smallest sensors possible if distortion is to be minimized. However, our analysis of trends in peak flux metrics and total flux indicates that preservation of odorant filament "sharpness" and the ability to measure very low concentrations may be mutually exclusive design goals.

For chemical sensor arrays inspired by the specific morphologies and sampling kinematics of the spiny lobster *P. argus* and the mantis shrimp *G. falcatus*, the shape of a sampled odorant filament appears to be preserved quite well in the flux time series. However, our results also imply that the olfactory neurons of these species probably cannot detect the brief flux event resulting from interception of a single 0.56 mm odorant filament arriving parallel to the antennule. Current chemical sensing technology is similarly constrained. This suggests either that spatial differences in flux across the aesthetasc array are utilized by animals, or that malacostracan crustaceans (and bio-inspired robots) simply might not require such highly detailed information to track turbulent odorant plumes.

## Acknowledgments

This research was supported by NSF grant # IOS-0842681 to M. Koehl and used resources of the National Energy Research Scientific Computing Center, which is supported by the Office of Science of the U.S. Department of Energy under Contract No. DE-AC02-05CH11231. We thank two anonymous reviewers for their comments on earlier versions of the manuscript.

# 3. Finite Arrays

## 3.1. Introduction

Many animals have small-scale hair-bearing appendages that are used for locomotion, feeding, and chemical sensing. A common feature of such appendages is that they operate in a relatively low-Reynolds number (Re) flow regime. At the fluid velocities and geometric scales of these organs, fluid inertia is either balanced or exceeded by viscous forces. In such flow regimes, non-intuitive behavior can be commonplace; for example, the feeding appendages of copepods were once thought to act as particle filters due to their morphology, but observations have shown that they sometimes act as paddles, pushing the water surrounding food particles and resulting in other mechanisms of food capture (Koehl 1995). The primary motivation of this work is the capture of scent molecules from the ambient fluid by the antennules of marine crustaceans, which also typically occurs in such transitory flow regimes. While previous studies have focused on only the flow of water through olfactory appendages, this work seeks to directly quantify odorant detection over a comprehensive parameter space for both an entire appendage as well as locally within an array of sensory hairs.

In the environmental conditions commonly encountered by marine crustaceans, odor compounds released into the water form spatially and temporally complex plumes. These turbulent plumes consist of concentrated filamentous structures interspersed with clean fluid (Crimaldi and Koseff 2001, Webster et al. 2003, Crimaldi and Koseff 2006). Sampling such odor filaments is critical to many marine crustaceans in the location of food, suitable habitats, and conspecifics. How animals perceive their odor landscape, however, is mediated by the small-scale fluid dynamics near their olfactory appendages.

This work focuses on arrays of hair-like structures called aesthetascs that are borne on one of the filaments of the antennules of many aquatic malacostracan crustaceans (e.g., crayfish, crabs, mantis shrimp, lobsters). The aesthetascs are tens of microns in diameter and contain the dendrites of hundreds of olfactory neurons enclosed by a thin, permeable cuticle (Gleeson 1982, Spencer and Linberg 1986, Laverack 1988, Grunert and Ache 1988,

Hallberg et al. 1992, Atema 1995, Mead and Weatherby 2002). Although there are many other chemosensory structures on these animals, the aesthetascs are the most well studied and play an important, though not crucial, role in olfaction-mediated behaviors such as plume tracking (Grasso and Basil 2002, Keller et al. 2003, Horner et al. 2004).

The aesthetasc-bearing branches of the antennules are typically flicked back and forth through the water as an active sampling mechanism. Since the "no-slip" condition dictates that the relative fluid velocity is zero along the entire surface of the sensory appendage, relatively thick boundary layers are always present around the aesthetascs due to their small size (Koehl 1996). The thickness of the boundary layers around each hair determines how much fluid moves through the gaps between hairs, versus around the array as a whole. Cheer and Koehl (1987b) have quantified this flow feature with "leakiness," which is the ratio of the volume of fluid that flows between neighboring hairs in a unit of time to the volume of fluid that would flow through the same area if the hairs were not there. Equivalently, leakiness can be defined as the ratio of the average fluid velocity in the gap between neighboring hairs to the freestream velocity.

Flicking reduces boundary layer thickness, increases leakiness (Koehl 1992, Mead and Koehl 2000, Koehl 2001b, Reidenbach et al. 2008), and facilitates odorant penetration into dense arrays of aesthetascs (Koehl et al. 2001, Mead et al. 2003, Koehl 2006). Furthermore, the movement is asymmetric: the faster downstroke or outstroke exhibits high leakiness while the slower return stroke and inter-flick pause exhibit low leakiness. This transition in flow regimes can critically affect the functioning of an olfactory appendage because it determines odorant access into the spaces between sensory hairs of the array (Koehl et al. 2001). However, few studies (Stacey et al. 2002) have explicitly quantified odorant transport to olfactory hair arrays; most have relied on leakiness and other fluid-based surrogates to infer odorant sampling performance. Although odorant acts as a passive scalar whose behavior is determined by the velocity field, the relationship between the two can be complex, especially for unsteady processes such as plume sampling.

During an odorant sampling event (a flick of the antennule through an odorant plume, e.g., Koehl et al. 2001), odorant molecules are transported via advection to the vicinity of an aesthetasc, reach the aesthetasc surface via molecular diffusion through the concentration boundary layer (e.g., Moore et al. 1991a), diffuse through the permeable cuticle into the lumen of the aesthetasc (e.g., Derby et al. 1997), and finally diffuse to and bind to receptor proteins on the outer dendritic segment of an olfactory neuron (e.g., Grunert and Ache 1988). We assume that these neurons act as odorant flux detectors such that that the rate of odorant molecule arrival to the receptors affects the signal that is output from the neuron, encoded as a series of action potentials or "spikes" (Kaissling 1998, Rospars et al. 2000). Thus, our principle interest is in the time-varying flux of odorant into an aesthetasc, integrated over the cylindrical aesthetasc surface. For simplicity, hereafter we refer to the

surface-integrated quantity as "odorant flux." We computed odorant flux for both individual hairs as well as summed over the entire array of hairs, which we refer to as "aggregate flux."

Here, we model flow around and odorant transport to simple rows of finite numbers of olfactory hairs, oriented in crossflow, as they intercept single odorant filaments. We build on the model of Cheer and Koehl (1987b), which included fluid flow around a pair of cylinders, the experimental work of Hansen and Tiselius (1992) on flow around more than two cylinders, and the model used in Chapter 2 of this work, which examined both flow and odorant transport to infinite arrays of cylinders but did not account for variations in leakiness or number of hairs. Accounting for variations in number of hairs is important because of the large range found in nature, from less than ten along the antennule of the juvenile mantis shrimp *G. falcatus* (Mead 2002) to a few thousand in the spiny lobster *P. argus* (Gleeson et al. 1993). The present work covers a detailed range of array widths from 2 to 15 hairs, and quantifies aspects of odorant flux that may be neurobiologically important (as detailed in Chapter 2). We focus on the following objectives:

- assess how well leakiness predicts odorant flux
- quantify variations in leakiness and aggregate flux to the entire array as sampling speed and geometry vary, particularly number of hairs
- quantify variations in leakiness and odorant flux locally within the arrays

## 3.2. Methods

### 3.2.1. Overview

We used numerical simulations to model the flow of seawater (kinematic viscosity $\nu \approx 9.4{\cdot}10^{-6}$ $\mathrm{m^2\,s^{-1}}$) around rows of cylinders $D = 25$ $\mu$m in diameter, as well as the advection and diffusion of low molecular weight odorant molecules (molecular diffusivity $k_D \approx 10^{-9}\,\mathrm{m^2\,s^{-1}}$) to the cylinders, at biologically relevant flow speeds (e.g., similar to the flick and return speeds of crustacean olfactory antennules, modeled as steady flow as an approximation to real flicking behavior). Our simplified odorant plume consists of a single filament, Gaussian in streamwise cross section, oriented parallel to the array. Although it is possible to numerically model an array of sensors moving through water containing an odorant filament, it is typically much simpler to model the equivalent problem of water containing an odorant filament moving past a stationary array of sensors. This allows the computational grid to remain fixed in time, and is the approach employed here.

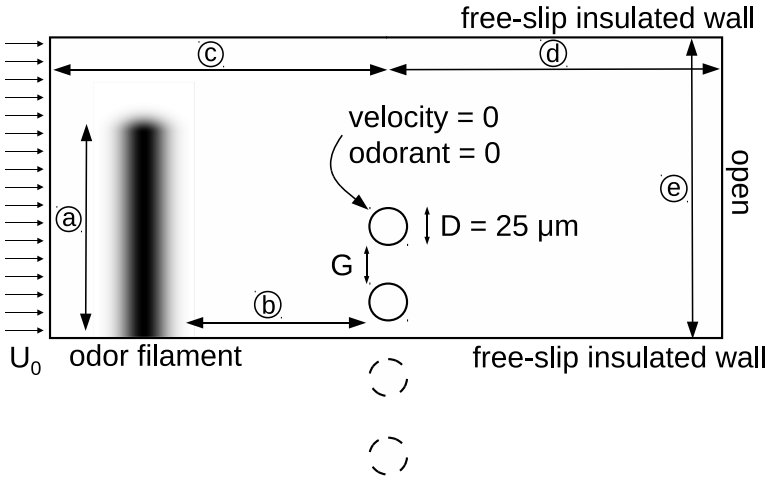


**Figure 3.1:** Computational domain for $N = 4$. Dashed circles represent the other half of the array which is not explicitly modeled due to symmetry. Distances are not to scale; actual odor filament is about 1 mm wide (streamwise) and initialized far ahead of the array, and actual domains are extremely large relative to the scale of the arrays. Circled letters correspond to important sources of error discussed in Section 3.2.4.

The steady fluid flow field for such geometry is set by three dimensionless numbers: a Reynolds number ($Re = {}^{U_0 D}/_{\nu}$) based on inflow velocity $U_0$ and cylinder diameter $D$, the gap to diameter ratio $G/D$ of the array, and the number of cylinders $N$. Since in the case of laminar flow, the flow is symmetric about the center of the row, we explicitly modeled half the row and used the appropriate boundary conditions to enforce symmetry. A sketch of the computational domain for $N = 4$ is shown in Figure 3.1; for odd $N$, only half of the center cylinder was explicitly modeled. We varied three parameters: $U_0$ (from 0.375 - 15.0 cm/s), $G$ (from 25 - 250 $\mu$m), and $N$ (from 2 - 15), concentrating the most effort in resolving variation versus $N$, as of the three, this parameter has received the least attention in the literature thus far. Not every possible combination of the three parameters was tested; instead, we focused more simulations on regions of the parameter space that exhibited interesting (non-monotonic or transitory) behavior.

We present our results primarily in terms of $U_0$ and $G$ but often list the corresponding dimensionless $Re$ and $G/D$ to simplify interpretation. Although the two could indeed be interchanged without error when discussing trends in non-dimensional leakiness, one cannot do the same (i.e., generalize observed trends versus $U_0$ and $G$ to trends versus $Re$ and $G/D$) with the dimensional metrics of odorant flux introduced in Section 3.2.3. Table 3.1 lists the correspondences between the dimensional and dimensionless parameters.

**Table 3.1:** Correspondences between varied parameters and $Re$ and $G/D$.

| $U_0$ (cm/s) | $Re$ |
|---|---|
| 0.375 | 0.1 |
| 0.749 | 0.2 |
| 1.87 | 0.5 |
| 3.75 | 1 |
| 7.49 | 2 |
| 15.0 | 4 |

| $G$ ($\mu$m) | $G/D$ |
|---|---|
| 25 | 1 |
| 80 | 3.2 |
| 125 | 5 |
| 250 | 10 |

## 3.2.2. Numerics

### Initial and boundary conditions

Before starting the simulation of unsteady odorant advection and diffusion, we first solve for the steady fluid flow field around the array of hairs. The flow is forced by a uniform speed of $U_0$ at the inflow face; this is equivalent to the array steadily moving through still fluid at $U_0$. A no-slip condition was imposed on the surfaces of each hair. The fluid leaves via an open boundary condition on the right domain face. The top and bottom faces are free-slip solid walls. The bottom wall simply maintains symmetry of the flow between the two halves of the array. Although we wish to model flow in an unbounded domain, a top wall is needed to compute a numerical solution. We therefore increased the domain height until the solution converged to within reasonable accuracy; see Section 3.2.4 for details.

Once the steady velocity field was determined, the odorant concentration field was initialized. We introduced a simple filament-like region of odorant some distance ahead of the array, where the flow was nearly uniform. The filament is a 1D Gaussian in the stream-wise direction except near the end, where it smoothly transitions to a 2D Gaussian that decays in both the stream-wise and cross-stream directions (Figure 3.1). We cut off the filament in this way because it could not be represented on the coarsest mesh in the far-field (Section 3.2.2), and to avoid sharp discontinuities that pose numerical problems. Since we wish to model an infinitely long odorant filament that already exists in the bulk fluid as it is intercepted by the array, both the vertical height of the filament and the distance between the initialized filament and the array were tested to ensure that the solution was unaffected by these values; see Section 3.2.4 for details. The filament was chosen to be $L = 0.56$ mm wide (we assume "width" to equal the smallest interval that contains 95% of the total odorant mass in the filament; this corresponds to a filament standard deviation $\sigma_f$ of 0.14 mm). This is the same as in the simulations of Chapter 2 and in the same range as the 1 mm wide odor

filaments used in a previous study of mantis shrimp odorant capture (Stacey et al. 2002), although odorant patches in water as small as 0.2 mm have been measured (Moore et al. 1992). A peak concentration of 1 mg/L was chosen arbitrarily, as the solution to the linear advection-diffusion equation will simply scale with this value.

Molecular diffusion causes the peak concentration of the odorant filament to decrease and its width to increase as it advects toward the array. Since the filament moves at different speeds depending on $U_0$ and needs to be initialized further ahead of the array at low $Re$ versus high $Re$ due to larger flow disturbances, we normalized the filaments such that they would all be identical (0.56 mm wide and 1 mg/L peak) by the time they reached the arrays, neglecting physical interactions with the arrays. This was done by initializing the stream-wise standard deviation as $\sigma_0 = \sqrt{\sigma_f^2 - 2k_D\Delta t}$, where $\sigma_f = 0.14$ mm and $\Delta t$ is the time it takes for the filament to advect from its starting position to the center of the array, and initializing the peak concentration as $C_0 = C_f \cdot \sigma_f/\sigma_0$, where $C_f = 1$ mg/L.

Boundary conditions for odorant are similar to those for velocity. Odorant-free water is introduced at the inflow face, and the outflow face is "open," with a stream-wise gradient in odorant concentration of zero imposed. The insulated wall bisecting the array again enforces symmetry in the odorant concentration field, while the top wall is a practical requirement whose spurious effects must be minimized (Section 3.2.4).

This study focuses on the physical processes governing odorant molecule arrival at the aesthetasc surface, and consequently we idealize the processes thereafter. Thus, we employ a simple Dirichlet condition for odorant at the cylinder surface, and set concentration to zero for all time. This results in a diffusive flux of odorant into the cylinder, which is recorded as the simulation progresses. This boundary condition models an ideal flux detector, which immediately and irrevocably consumes all odorant molecules that arrive on it, perhaps by rapid enzymatic degradation (Trapido-Rosenthal et al. 1987, Carr et al. 1990). We believe this to be a more appropriate model of olfactory sensors than the other straightforward alternative, a Neumann boundary condition, in which concentration would be measured instead of flux (Kaissling 1998, Rospars et al. 2000).

### Software and computational mesh

The commerical software COMSOL Multiphysics 4.2 was used to numerically solve the Navier Stokes equations and advection-diffusion equation for steady fluid flow and unsteady odorant transport, respectively. COMSOL employs the finite element method (FEM) and implicit timestepping for time-dependent problems; we used a combination of triangular and quadrilateral elements with linear discretizations for odorant concentration, and the generalized alpha timestepping scheme.

Generating the computational mesh was not trivial, as the goal was to advect a relatively sharp Gaussian pulse a relatively large distance through the domain (i.e., a moving-front problem) while representing molecular diffusion accurately, as well as capturing the even sharper concentration gradients that form as the odorant filament passes through the gaps in the array. Simultaneously, an extremely large domain is needed relative to the size of the array because of the large effects of boundaries that occur at low $Re$ (Loudon et al. 1994, Lange et al. 1998).

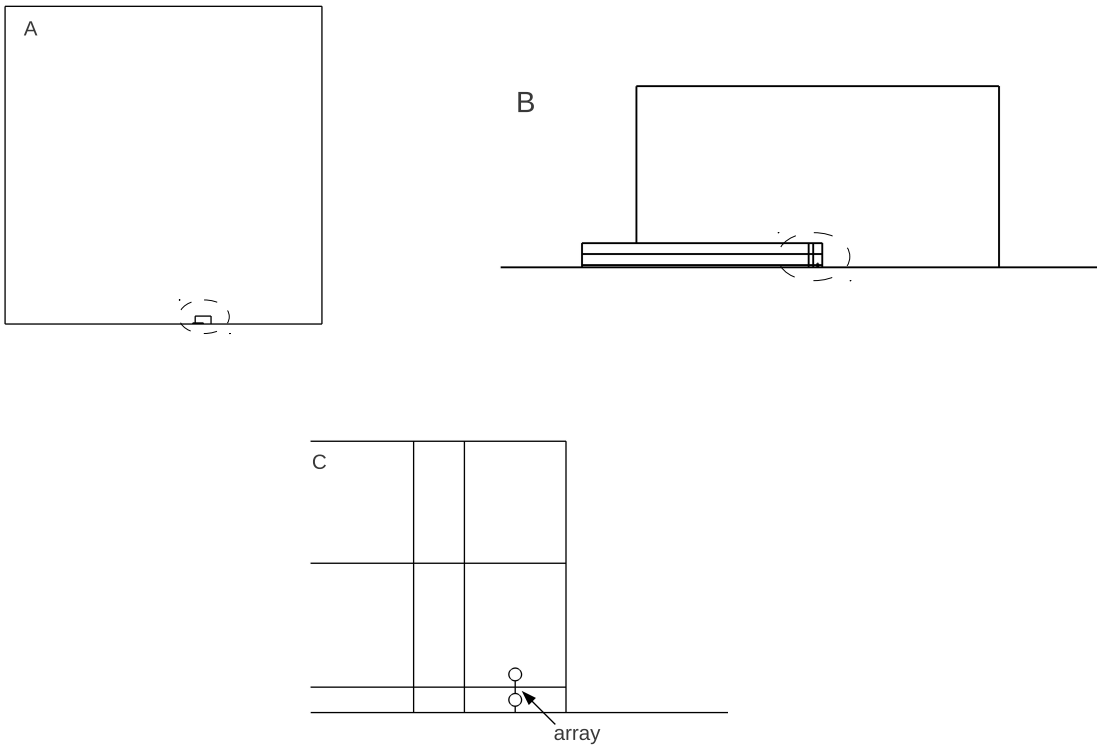


**Figure 3.2:** Sketch of different mesh regions. A) Entire domain; dashed ellipse indicates zoom-in on rectangular region B. B) Refined rectangular region designed to resolve velocity boundary layer around array. Lines are not walls in the model, but only serve to demarcate different mesh regions. Dashed ellipse indicates zoom-in on near-field region C. C) Sub-divided refined regions near array; again, straight lines show different mesh regions and are not walls.

Since gradients in the velocity field are small far from the array, we employed a very coarse triangular mesh (0.75 mm elements) in the far field (Figure 3.2 A). Note that the array of cylinders is too small to be visible here – such a the vast domain size is needed to make the unwanted effects of the domain edges insignificant at low $Re$. The domain region

near the array was refined throughout a small rectangular region (25 $\mu$m elements) that enclosed much of the velocity boundary layer around the array (Figure 3.2 B, Figure 3.3 A). Within this, another rectangular region encompasses the array and extends far ahead of it (Figure 3.2 B); the odorant filament is initialized near the upstream edge of this region. It is within this long rectangular area that we wish to fully resolve odorant transport as the filament advects toward and into the array. In the left-hand side of the region, we employed anisotropic structured rectangular meshes: because the flow ahead of the array is mostly unidirectional, coarse resolution could be used in the cross-stream direction (parallel to the filament) while fine resolution could be used in the stream-wise direction to ensure accurate advection. We used several domain sub-divisions to fine tune mesh resolution, increasing it from bottom to top and left to right, to resolve the sharpening gradients as the filament approaches and bends around the array; mesh size decreases from 25 to 2 $\mu$m in these regions (Figure 3.2 C, Figure 3.3 A). Finally, a very fine unstructured triangular mesh was used in the immediate vicinity of the cylinders (boxes containing cylinders in Figure 3.2 C, Figure 3.3 A) with a "boundary layer mesh" around each cylinder. The latter consists of layers of thin quadrilateral elements designed to resolve sharp gradients normal to surfaces, such as we expect as odorant fluxes into each hair. The mesh in the immediate vicinity of a cylinder is shown in Figure 3.3 B, where the maximum size of the triangles is 1.25 $\mu$m; this region appears black in Figure 3.3 A because of the high density of elements.

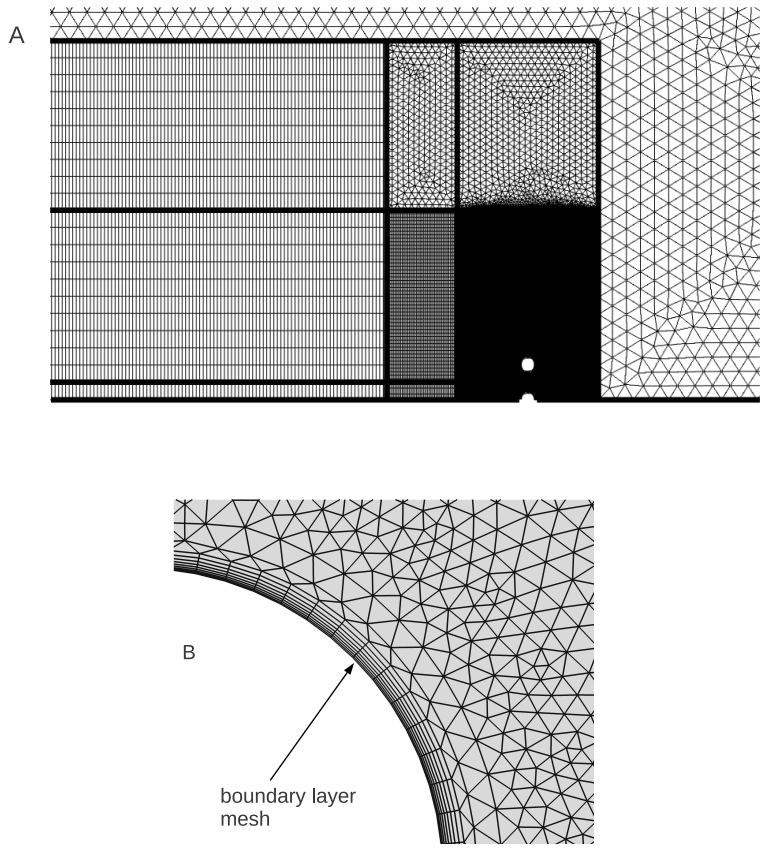


**Figure 3.3:** Computational mesh in A) near-field of array, corresponding to regions shown in Figure 3.2, and B) in immediate vicinity of a cylinder.

Mesh size varied with the number of cylinders from about 300,000 elements for a two-cylinder array to about a million elements for a 15-cylinder array. Likewise, computation time varied from about 12 hours to 60 hours, with higher $Re$ simulations taking longer. The simulations were generally run on a single CPU core, though up to four cores were sometimes used on a desktop workstation for a parallel speedup of about 2.8.

### 3.2.3. Sample output and calculation of performance metrics

Figure 3.4 shows a representation of the steady velocity field for $U_0 = 3.75$ cm/s [$Re = 1$], $G = 25$ $\mu$m [$G/D = 1$], $N = 6$; the simulation data has been mirrored across the array center to simplify interpretation. The velocity vectors only indicate flow direction, not speed, as there is actually very little movement behind the array compared to in front of it and around the

edges. However, normalizing velocity in this way allows one to see the two (slowly moving) standing vortices in the wake, similar to those that would form behind a flat plate without any gaps. We quantified the flow reduction through the array using leakiness, introduced in Section 3.1. For each gap of every array, we computed (within COMSOL) an individual leakiness equal to the average u-velocity in the gap divided by the freestream velocity $U_0$. This is equivalent to the flow rate through the gap divided by how much flow there would be if the hairs were not present. The leakiness of the entire array is simply equal to the mean of these individual leakiness values; we call the whole-array quantity "aggregate leakiness." Note that for leakiness, "average" leakiness is identical to "aggregate" leakiness - this differs from how flux is treated (below). For the case in Figure 3.4, the leakiness values are about 0.09, meaning the average velocity in the gaps is about 9% of the freestream (sampling) speed.

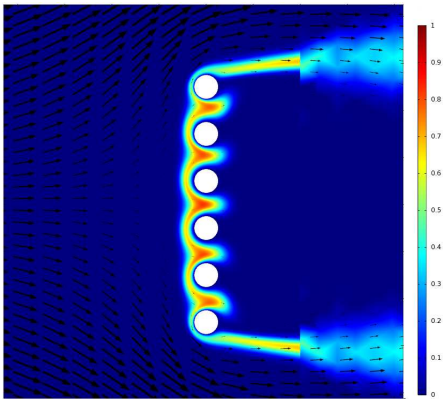


**Figure 3.4:** Velocity field vectors and odorant concentration field at an instant in time for $U_0 = 3.75$ cm/s ($Re = 1$), $G = 25$ $\mu$m ($G/D = 1$), $N = 6$. Colorbar indicates odorant concentration (mg/L).

Also shown in Figure 3.4 is the odorant concentration field at a single point in time, as odorant advects through the gaps in the array. As the structure of the odorant filament enters the gaps, it is heavily strained such that gradients that were intially parallel to the flow become normal to the flow. The zero-concentration boundary condtion on each hair preserves a region of depleted odorant around each hair and leads to a time-varying flux of odorant molecules into the hairs via molecular diffusion. The low leakiness of the array also causes a lag between concentration and flux, and in Figure 3.4, the peak concentration in the far-field odorant filament has already passed the array. Once the filament advects past the hairs, its fine-scale structure is obliterated by the coarse outer mesh visible in the right part of the figure. However, this does not appear to propagate upstream and affect odorant

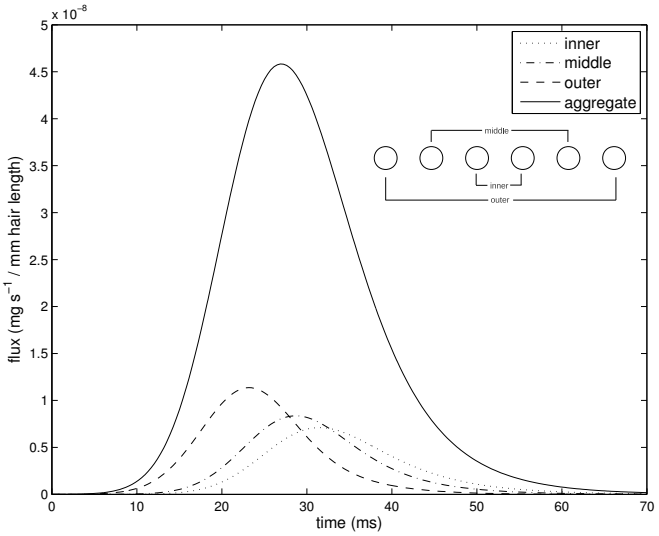


**Figure 3.5:** Time series of odorant flux into the array. Aggregate curve is for the entire array of $N = 6$ hairs. t = 0 is arbitrary.

flux into the cylinders results since various aspects of this flux changed little if outer mesh element size was halved (see Section 3.2.4).

The time series of odorant flux into the hairs is shown in Figure 3.5; the fluxes into the bottom three hairs are identical to those for the top three so only one set is shown. Also plotted is the aggregate flux time series generated by the entire 6-hair array, created by summing the fluxes into all 6 hairs. The flux to the outer hairs always occurs first by an often substantial amount of time, followed by each hair in turn moving toward the center. The outermost hairs also always experience the highest peak odorant flux, again with a monotonic decrease toward the center hair(s).

Little is known about how animals process the signals generated by each aesthetasc on an antennule. Neural convergence, or the aggregation of many neurons to fewer neurons, means that it is unlikely that each aesthetasc's output is represented separately in the brain. However, differences in neural stimulation across the array resulting from purely physical transport processes could conceivably affect the signals received in the brain. Thus, we examined properties of both the aggregate flux signal and the individual flux signals generated by each hair. Given a flux time series $f(t)$, these metrics are:

| | |
|---|---|
| peak flux | maximum value of $f(t)$ |
| peak onset slope (or peak slope) | maximum value of $\frac{d}{dt}(f(t))$ |
| time-integrated flux (or total flux) | $\int_0^\infty f(t)dt$ |
| flux duration | minimum value of $t_2 - t_1$ such that $\int_{t_1}^{t_2} f(t)dt = 0.95$(total flux) |

These flux metrics were chosen to match those of previous study of odorant detection by mantis shrimp (Stacey et al. 2002) as well as a study of infinite olfactory hair arrays (Chapter 2 of this work). The reader is referred to Chapter 2 for a detailed discussion of why these properties may be neurobiologically important.

Storage space limitations meant that highly resolved simulation output could not always be saved. Therefore, to enable accurate calculation of the flux metrics (especially peak slope), cubic splines were fitted to the saved flux time series. Since most time series consisted of long regions of zero flux and a relatively brief pulse, the pulse region was first bounded by locating the closest points to the maximum point that were at least 10,000 times smaller than it. Then 20 uniformly spaced knots were placed in each "tail" region, and 40 uniformly spaced knots were placed in the pulse region. Cubic splines were fit using this set of knots and the Shape Language Modeling package for MATLAB (D'Errico 2010). This choice of knots resulted in excellent fits for all time series, verified by visual inspection. All flux metrics were then calculated analytically from the fitted splines using functions such as fnmin(), fnder(), and fnint() in the Curve Fitting Toolbox for MATLAB 2011a.

Since the aggregate flux metrics are obtained after summing the responses from all the hairs, if all the hairs experienced exactly the same flux, the first three aggregate flux metrics would simply increase proportionally with $N$ (i.e., doubling $N$ would double peak flux, peak slope, and total flux), while aggregate duration would remain constant. However, non-linear effects such as lag between the fluxes into each hair often result in diminishing returns in aggregate flux. We therefore computed average peak flux, peak slope, and time integrated flux by dividing the aggregate quantities by N. By examining trends in the average quantities versus number of hairs, any deviation from proportionality becomes clear. Since there is large variation in the flux metrics across $U_0$ and $G$ and because we are mainly interested in trends in the average metrics only with $N$, we normalized these values by the values for $N = 2$ in Figure 3.6. Thus, the normalized average metrics should not be compared across arrays with different $U_0$ or $G$.

### 3.2.4. Convergence testing

Careful attention was paid to the following sources of error (letters correspond to labeled distances in Figure 3.1, but they are not drawn to scale):

- mesh size in each region of refinement
- time stepping relative error tolerance
- vertical length of odorant filament (a)
- distance from initialized odorant filament to array (b)
- distance from inflow face to array (c)
- distance from outflow face to array (d)
- height of domain (e)

We tested each of these factors at the four cases defined by the combinations of $U_0 = 7.49$ cm/s, $U_0 = 0.375$ cm/s, $G = 25$ $\mu$m, and $G = 250$ $\mu$m, with $N$ held constant at 10 hairs. Convergence of peak flux, peak onset slope, and total flux was tested by repeatedly halving (in the case of mesh size and time step error tolerance) or doubling (in the case of distances) each factor until each of these metrics changed by less than 5%. The limiting values of each factor were then conservatively used for most simulations, with these exceptions: because much of the computation time of each simulation is spent advecting the odor filament from its starting position to the vicinity of the array, we halved this distance for $U_0 = 3.75$ cm/s and $U_0 = 7.49$ cm/s after testing its effect at each $U_0$. Secondly, since we later expanded the parameter space by including $U_0 = 15$ cm/s, and $N > 10$, those simulations may contain larger errors. However, we did not observe any strange behavior in trends across $U_0$ or $N$ that would be indicative of high error for these simulations in particular.

## 3.3. Results

### 3.3.1. Aggregate metrics

#### Leakiness

The range in total leakiness values spans a large range, from 0.02 – 0.88 (Figure 3.6 A). The lower end of this range represents non-porous paddle like behavior, while the upper end represents sieve or rake-like behavior.

Aggregate leakiness intuitively increases monotonically with $U_0$ and $G$ for all values of $N$ (Tables 3.2 and 3.3). Increasing the sampling speed or spacing between hairs both act

**Table 3.2:** Ratio of aggregate parameter value at $U_0 = 7.49$ cm/s [$Re = 2$] to value at $U_0 = 0.375$ [$Re = 0.1$] for $N = 10$.

| | G = 25 $\mu$m | G = 125 $\mu$m | G = 250 $\mu$m |
|---|---|---|---|
| leakiness | 6.1 | 7.0 | 4.7 |
| peak flux | 53 | 22 | 14 |
| peak slope | 5400 | 2000 | 1100 |
| total flux | 0.43 | 0.23 | 0.21 |
| flux duration | 0.0075 | 0.011 | 0.015 |

**Table 3.3:** Ratio of aggregate parameter value at $G = 250$ $\mu$m [$G/D = 10$] to value at $G = 25$ $\mu$m [$G/D = 1$] for $N = 10$.

| | $U_0 = 0.375$ cm/s | $U_0 = 3.75$ cm/s | $U_0 = 15.0$ cm/s |
|---|---|---|---|
| leakiness | 9.5 | 10 | 7.3 |
| peak flux | 7.7 | 2.8 | 2.1 |
| peak slope | 14 | 4.5 | 2.7 |
| total flux | 2.8 | 1.5 | 1.4 |
| flux duration | 0.31 | 0.50 | 0.63 |

to increase permeability to flow. This is in agreement with the work of Cheer and Koehl (1987b) on a pair of cylinders.

Aggregate leakiness decreases asymptotically with number of hairs, in agreement with the work of Hansen and Tiselius (1992). Contrary to intuition, more fluid is not forced through the array as it gets wider (via $N$) and obstructs more of the flow; instead, the boundary layer around the array simply grows larger and deflects ever larger quantities of fluid off to the sides. It is therefore critical to note that as $N$ approaches infinity, behavior does *not* approach that of an infinite array - the two are fundamentally different in this regard.

The importance of all three quantities ($U_0$, $G$, and $N$) on leakiness is especially apparent in the intersections of some curves (e.g., $U_0 = 15$ cm/s, $G = 25$ $\mu$m and $U_0 = 0.375$ cm/s, $G = 250$ $\mu$m): which case has higher leakiness depends on $N$, and an array of 4 hairs has about the same leakiness for both cases. However, the dependence of leakiness on $N$ is nonetheless relatively small compared to the effects of $U_0$ and $G$. Since changing $N$ never drastically changes leakiness in an absolute sense (from zero to one), whether an appendage behaves as a sieve or a paddle is primarily determined by $U_0$ and $G$.

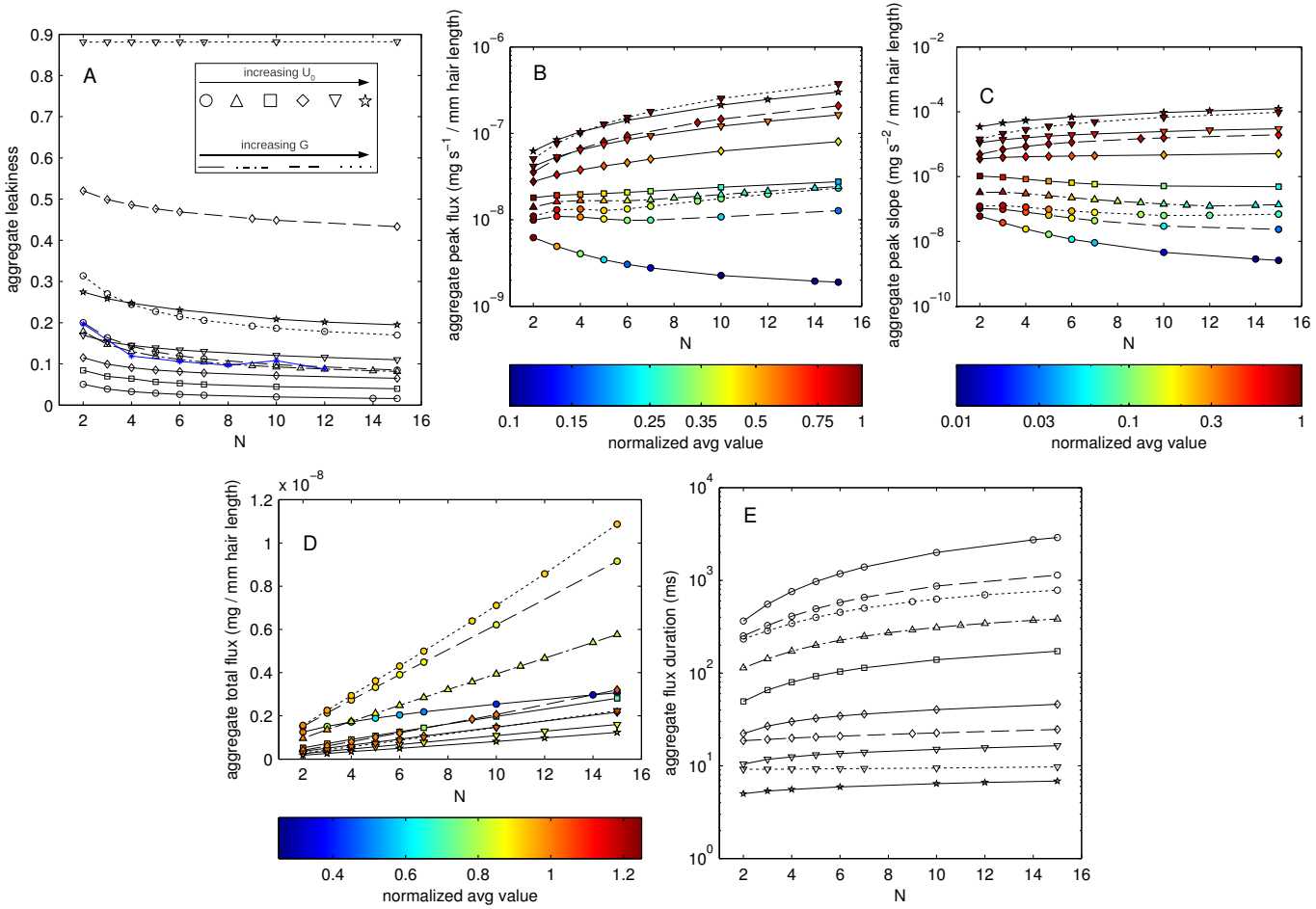


**Figure 3.6:** Aggregate sampling performance metrics vs number of hairs $N$. Marker symbols indicate $U_0$ (cm/s), with corresponding $Re$ in [ ]: $\bigcirc = 0.375$ [0.1], $\triangle = 0.749$ [0.2], $\square = 1.87$ [0.5], $\diamond = 3.75$ [1], $\triangledown = 7.49$ [2], $\star = 15.0$ [4]. Lines indicate gap spacing ($\mu$m) with corresponding $G/D$ in [ ]: solid = 25 [1], dash-dot = 80 [3.2], dashed = 125 [5], dotted = 250 [10]. Trends across markers and lines are summarized in inset of A. Marker color (where present) indicates normalized average value as discussed in Section 3.2.3. Blue line in A = physical models of Hansen and Tiselius (1992) (Re = 0.2, G/D = 3.2). Note logarithmic scaling on several y-axes and colorbars.

### Peak metrics

As shown in Table 3.3, peak flux and peak slope increase with $G$, indicating that hairs placed infinitely far apart would maximize these aspects of odorant capture. The increase becomes larger at smaller $U_0$, when interactions between hairs are more significant. The peak metrics also increase with $U_0$, with peak slope being especially sensitive, increasing thousands of times from $U_0 = 0.375$ cm/s [$Re = 0.1$] to $U_0 = 7.49$ cm/s [$Re = 2$] (Table 3.2).

Peak flux and peak slope display intriguing behavior versus $N$. They increase with $N$ at high $U_0$, but decrease with N at low $U_0$ (Figure 3.6 B and C). Increasing $G$ also tends to increase the slope of the curves but it is not entirely clear whether gap size can determine whether the peak metrics increase or decrease with $N$. At low $U_0$, changes in $G$ do seem to cause transitional behavior in sparse arrays, marked by inflection points in the curves. The data suggest the existence of certain $Re$ and $G/D$ for which there is no change in peak flux or peak slope as $N$ increases.

The change in marker color from warm to cold along the curves in Figure 3.6 B and C indicates that the average peak metrics (both flux and slope) decrease with $N$ for all $U_0$ and $G$ we tested. As the number of hairs increases, decreasing leakiness coupled with larger array width causes more stretching of the odorant filament as it bends around the array (Figure 3.4), and this stretching accelerates diffusion of the filament before it enters the array. Since this effect is very slight at high $U_0$ and high $G$, the aggregate quantities still increase with $N$ in those cases, as the added surface area of additional hairs outweighs the slight decrease in flux to preexisting hairs. At low $U_0$ and low $G$, however, the decrease in flux into the preexisting hairs is so large that even the aggregate peak metrics, summed over all hairs, decrease as hairs are added.

As with leakiness, there are conspicuous intersections for peak flux versus $N$ in Figure 3.6 B. The existence of these intersections emphasizes that different combinations of $N$, $Re$, and $G/D$ may achieve similar odorant detection dynamics.

### Total flux

Aggregate total flux increases with $G$ (Table 3.3), so isolated hairs would be expected to achieve maximum peak metrics as well as total molecules captured. However, unlike the peak metrics, total flux decreases with $U_0$ (Table 3.2); this tradeoff between peak metrics and total odorant mass captured was also found to occur with infinite arrays (Chapter 2 of

this work). Again, the changes are largest at low $G$ when cylinders can "feel" each other the most.

Unlike the peak metrics, aggregate total flux always increases with number of hairs (Figure 3.6 D, even though average total flux always decreases to some extent as hairs are added. The decrease in average total flux is largest at low $U_0$ and low $G$, and manifests as a nonlinear relationship between aggregate total flux and $N$. Nonetheless, since aggregate total flux always increases with $N$, the decrease in leakiness is not enough to overcome the increased surface area of more hairs. In other words, even though the odorant filament is less sharp as it enters a wider array and concentration gradients less steep, more odorant molecules in total are captured.

Again, intersections of curves in Figure 3.6 D indicate the interdependence of sampling speed, gap size, and number of hairs. $U_0 = 0.375$ cm/s, $G = 25$ $\mu$m provides an interesting example: With 4 hairs, an array with this combination of sampling speed and gap size will capture the same number of odorant molecules as another 4-hair array with $U_0 = 0.749$ cm/s, $G = 80$ $\mu$m (higher speed and larger gap size). With about 14 hairs, this array achieves the same total flux as another array with $U_0 = 3.75$ cm/s, $G = 125$ $\mu$m (further increases in both speed and gap size).

### Flux duration

The approximate duration of odorant stimulation (flux) decreases dramatically with $U_0$ and, to a lesser extent, $G$ (Tables 3.2 and 3.3). Like with the other flux metrics, the largest changes occur at low $U_0$ and low $G$. As seen in Figure 3.6, the global range of values is huge, from 5.0 ms to 2.9 s. The sampling speed and geometry of an olfactory appendage can therefore be critical in controlling how long neurons are stimulated for when an odorant filament is encountered.

Duration increases with $N$ (Figure 3.6 E). This is partly because as the array becomes wider, there is an increasingly large lag between the flux occurring at the outer edge of the array versus in the center (Figure 3.5), but also because the flux durations for each individual hair increase, as indicated by increasing average durations and the data presented in Section 3.3.2. The increase in duration with $N$ is far greater at low $U_0$, and to a lesser extent, low $G$. Presumably aggregate duration eventually asymptotes as $N$ increases, even at low $U_0$, but we did not study large enough $N$ to observe this for all cases.

## 3.3.2. Intra-array variability

### Leakiness

The central part of the array is least leaky in most cases, with a jump at the outermost hairs at low $U_0$ (Figure 3.7 A). At high $U_0$ and high $G$, there is very little variation in leakiness, or any other parameters, across the array (Table 3.4). Interestingly, at high $U_0$, small $G$, and large enough $N$, the central part does become the most leaky section. The transition is clearly visible near $N = 6$ for $U_0 = 7.49$ cm/s [Re = 2] in Figure 3.7 B, and at even higher speeds, leakiness is highest in the center for all $N$ (Figure 3.7 C). This trend seems the more intuitive pattern - relatively more fluid is forced through the center region versus the outer region as hairs are added, though leakiness at a given location in the array still generally decreases with $U_0$.

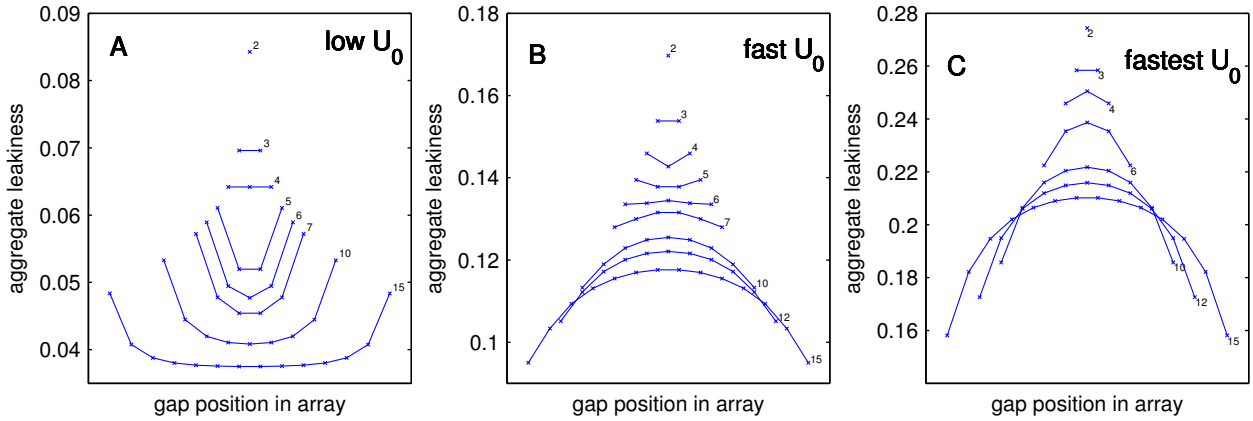


**Figure 3.7:** Intra-array variability in individual-gap leakiness. Each curve corresponds to an array with the labeled number of hairs. $G = 25$ $\mu$m $[G/D = 1]$ in each case. Qualitatively different behavior is observed at A) $U_0 = 1.87$ cm/s [Re = 0.5], (representative shape for most of parameter space) versus B) $U_0 = 7.49$ cm/s [Re = 2] (higher $U_0$, small $G$) versus C) $U_0 = 15.0$ cm/s [Re = 4] (highest $U_0$ tested, small $G$). Note different y-axis scales.

**Table 3.4:** Summary of intra-array variability across $U_0$ and $G$, tabulated as (value at outermost hair) / (value at innermost hair), for $N = 10$. high $U_0 = 7.49$ cm/s [$Re = 2$], low $U_0 = 0.375$ cm/s [$Re = 0.1$], high $G = 250$ $\mu$m [$G/D = 10$], low $G = 25$ $\mu$m [$G/D = 1$]

| | low $U_0$ low $G$ | high $U_0$ low $G$ | low $U_0$ high $G$ | high $U_0$ high $G$ |
|---|---|---|---|---|
| leakiness | 1.7 | 0.9 | 1.3 | 1.0 |
| peak flux | 3.2 | 1.5 | 1.5 | 1.0 |
| peak slope | 4.4 | 1.7 | 1.9 | 1.0 |
| total flux | 2.5 | 1.2 | 1.2 | 1.0 |
| flux duration | 0.82 | 0.86 | 0.75 | 1.0 |

### Peak metrics and total flux

The peak flux, peak slope, and total flux values occur on the outside ends of the array, with large jumps at the outermost cylinders (Figure 3.8 A, B, and C). This spatial pattern is expected for peak flux and peak slope (panels A and B) due to the high shear at the outer hairs, and the sharp instantaneous concentration gradients it creates. Less obvious is why total flux (panel C) also would increase from center to edge. It is possible that the thinner concentration boundary layers at the outer parts of the array more than make up for the decreased time available for molecule capture to occur (see next section).

Of additional note, there is little variation in total flux to the outermost hairs as compared with variation in the peak metrics to those hairs as $N$ increases (panel C). In contrast, variation across a given array diminishes as $N$ increases for the peak metrics, while the difference between innermost and outermost total flux gets larger with additional hairs.

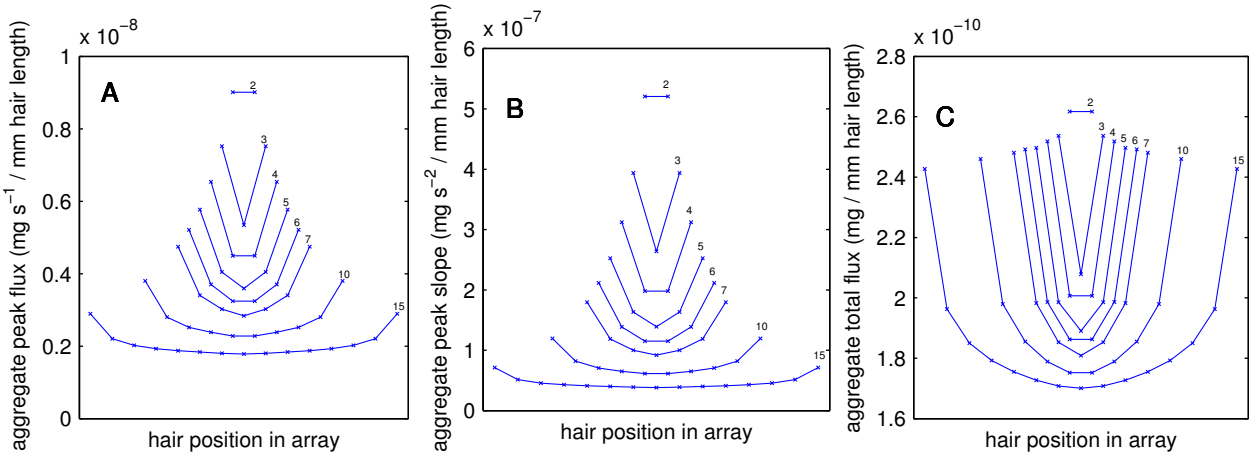


**Figure 3.8:** Intra-array variability in individual-hair A) peak flux, B) peak slope, and C) total flux. Each curve corresponds to an array with the labeled number of hairs. $U_0$ = 1.87 cm/s [Re = 0.5], $G$ = 25 $\mu$m [G/D = 1] for A), B), and C); these same qualitative shapes were observed over the entire parameter space.

### Flux duration

In contrast to leakiness and flux, the longest duration of odorant flux occurs in the center of the array for most sampling speeds and gap sizes studied (Table 3.4, Figure 3.9 A and B), with variability diminishing at high $U_0$ and high $G$ (Table 3.4). At low $U_0$, the difference between innermost and outermost durations can be more than 100 ms at $U_0$ = 0.375 cm/s [$Re$ = 0.1] (not shown) and about 40 ms at $U_0$ = 1.87 cm/s [$Re$ = 0.5] (Figure 3.9 A). This is a substantial variation, on the order of crustacean neural timescales (the clawed lobster *H. americanus* requires 50 ms to detect an odor and 200 ms to distinguish its concentration (Gomez and Atema 1996a)).

We also note that there is a qualitative change in the spatial varation of flux duration as $N$ changes at high $U_0$ and low $G$. As hairs are added in this regime, the decrease in duration at the outer hairs diminishes and eventually the profile shape across the array reverses, with the outermost hairs experiencing longer odorant stimulation than their neighbors (Figure 3.9 C). This change does not seem to be directly associated with the change in intra-array leakiness structure described above since the change in leakiness profile shape occurs at N = 6 in Figure 3.7 B while the change flux duration profile shape requires larger $N$ to develop in Figure 3.9 B. The higher flux duration at the outermost hairs in Figure 3.9 C (the highest $U_0$ we tested) is probably not neurobiologically significant, however, since the variation is

only on the order of a few milliseconds; for practical purposes, the profiles in this case are probably flat.

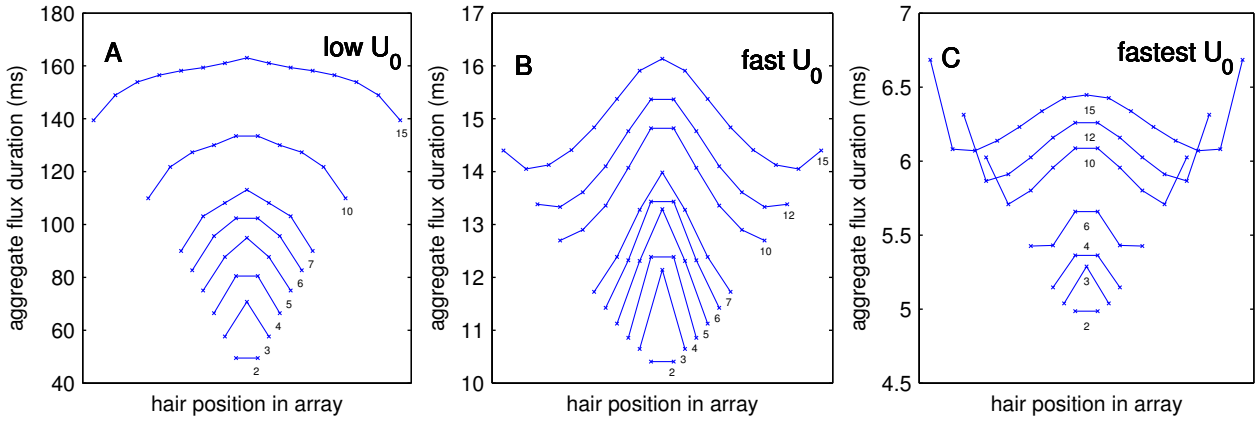


**Figure 3.9:** Intra-array variability in individual-hair flux duration. Each curve corresponds to an array with the labeled number of hairs. $G = 25$ $\mu$m $[G/D = 1]$ in each case. Qualitatively different behavior is observed at A) $U_0 = 1.87$ cm/s [Re $= 0.5$] (representative shape for most of parameter space) versus B) $U_0 = 7.49$ cm/s [Re $= 2$] (higher $U_0$, small $G$) versus C) $U_0 = 15.0$ cm/s [Re $= 4$] (highest $U_0$ tested, small $G$). Note different y-axis scales.

## 3.4. Discussion

### 3.4.1. Leakiness vs uptake

Previous studies on the small-scale dynamics within crustacean olfactory appendages have focused on aspects of the fluid velocity field. Transport of a passive scalar such as odorant has rarely been explicitly addressed. Leakiness has thus been used as a simple descriptor of how much fluid, and the food or scent it carries, can penetrate into the spaces between hairs of an array. Although the fluid velocity field does largely determine the transport dynamics of a passive scalar, the relationship is by no means simple even at low $Re$ laminar conditions, and is complicated by the unsteady aspect of plume sampling. Here, we can directly assess the effectiveness of leakiness at explaining odorant sampling performance.

The large changes in leakiness that occur over the parameter range covered by many hair-bearing appendages is undoubtedly related to the behavior we see in odorant molecule

capture, but leakiness by itself is not a good predictor of any of the odorant flux metrics we studied. Although increased leakiness does generally predict increased peak flux, peak slope, and decreased flux duration, poor collapse is observed in plots of each metric (peak flux, peak slope, total flux, flux duration) versus leakiness (Figure 3.10). This is the case for both aggregate parameters of the entire array, and for locally within the array, such as in the center (not shown). Hence, odorant flux depends on array morphology and sampling kinematics in unique ways and leakiness cannot be relied upon to predict this behavior.

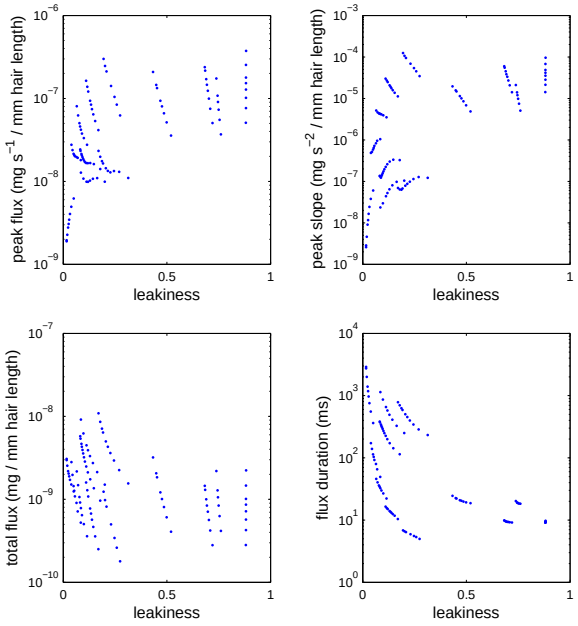


**Figure 3.10:** Aggregate flux metrics plotted vs aggregate leakiness for all simulations.

## 3.4.2. Effect of number of hairs

Although leakiness does decrease with number of hairs, the effect is small relative to the changes across $U_0$ and $G$ (Section 3.3.1). The overall scale of leakiness variation within the arrays is also small (Section 3.3.2) and means that it is unlikely for one part of a hair array to be paddle-like and another section to simultaneously be sieve-like. The basic function of a hair bearing appendage, therefore, seems dependent only on $Re$ and $G/D$, not the number of hairs.

The simple monotonic variation in leakiness versus $N$ stands in contrast to the behavior of the flux metrics. The opposite effects of $N$ on aggregate peak flux and peak slope at different

$U_0$ and $G$ (Section 3.3.1) could have important consequences for animals that change the number of hairs on their appendages as they grow. Stacey et al highlighted how changes in $Re$ and $G/D$ between juvenile and adult stomatopods (*G. falcatus*) lead to large changes in odorant transport to the aesthetascs (Stacey et al. 2002). Stomatopods also increase $N$ as they grow. Here, we show how this can have opposite effects on odorant flux during the flick versus return strokes, in addition to the changes in $Re$ and $G/D$ that also occur. Our data (Figure 3.6 B and C) also suggest the possibility of hair-bearing appendages that experience nearly the same peak flux and peak onset slope over a range of $N$ (e.g., as the animal grows), despite changes in total array surface area.

Some animals, such as the spiny lobster *P. argus*, have thousands of aesthetascs arrayed along their antennules. Since the behavior of finite arrays is fundamentally different from that of infinite arrays (Section 3.3.1), one motivation of this work was to determine a sufficient value of $N$ such that the odorant transport dynamics, at least near the center such arrays, are no longer sensitive to further increases in $N$. As shown by the trends in Figure 3.11 of innermost-hair behavior, there is no simple answer, as it depends on $U_0$ and $G$, and often on the specific quantity of interest. At high $U_0$ and $G$, interactions between cylinders are very small and a pair of cylinders is in fact nearly identical to a row of ten or more in terms of leakiness and odorant flux, both in an aggregate sense and at the center of the array (Figures 3.6 and 3.11). As $U_0$ and $G$ decrease, however, it takes more and more hairs for leakiness and the flux metrics to asymptote in the center of the array (Figure 3.11), particularly in the cases of peak flux and peak slope (panels B and C). Total flux at the array center (panel D) may lack asymptotic behavior entirely at $U_0 = 0.375$ cm/s [$Re = 0.1$], $G = 250$ $\mu$m [$G/D$] = 10, instead having a local minimum between 7 and 10 hairs. Therefore, although the fast flick movements of many olfactory appendages might be modeled with just a few hairs without incurring large errors, the same is not true for the slower return strokes. This could be a formidable obstacle to the development of models that seek to include the complete flick-return-pause sequence of appendages with many hairs.

Lastly, the question of why some animals (e.g., *P. argus*) have so many aesthetascs has been raised in the literature. Each aesthetasc has been shown to contain the same complement of olfactory receptor neurons (Steullet et al. 2000), so additional hairs probably do not help with discrimination of odor quality. Instead, long arrays of aesthetascs could simply improve the chances of encountering a thin odor filament oriented arbitrarily relative to the antennule. Here, we show that there may be some performance costs (i.e., decreasing aggregate leakiness, peak flux, and peak slope) associated with increasing the number of hairs in an array, but only at low sampling speeds (Figure 3.6 A, B, C). The rapid flick movements of marine crustaceans put the aesthetasc array in a regime where additional hairs do intuitively act to increase all aggregate flux metrics for a given odorant filament. Hence, one simple advantage of many hairs may be to increase sensitivity and make detection more

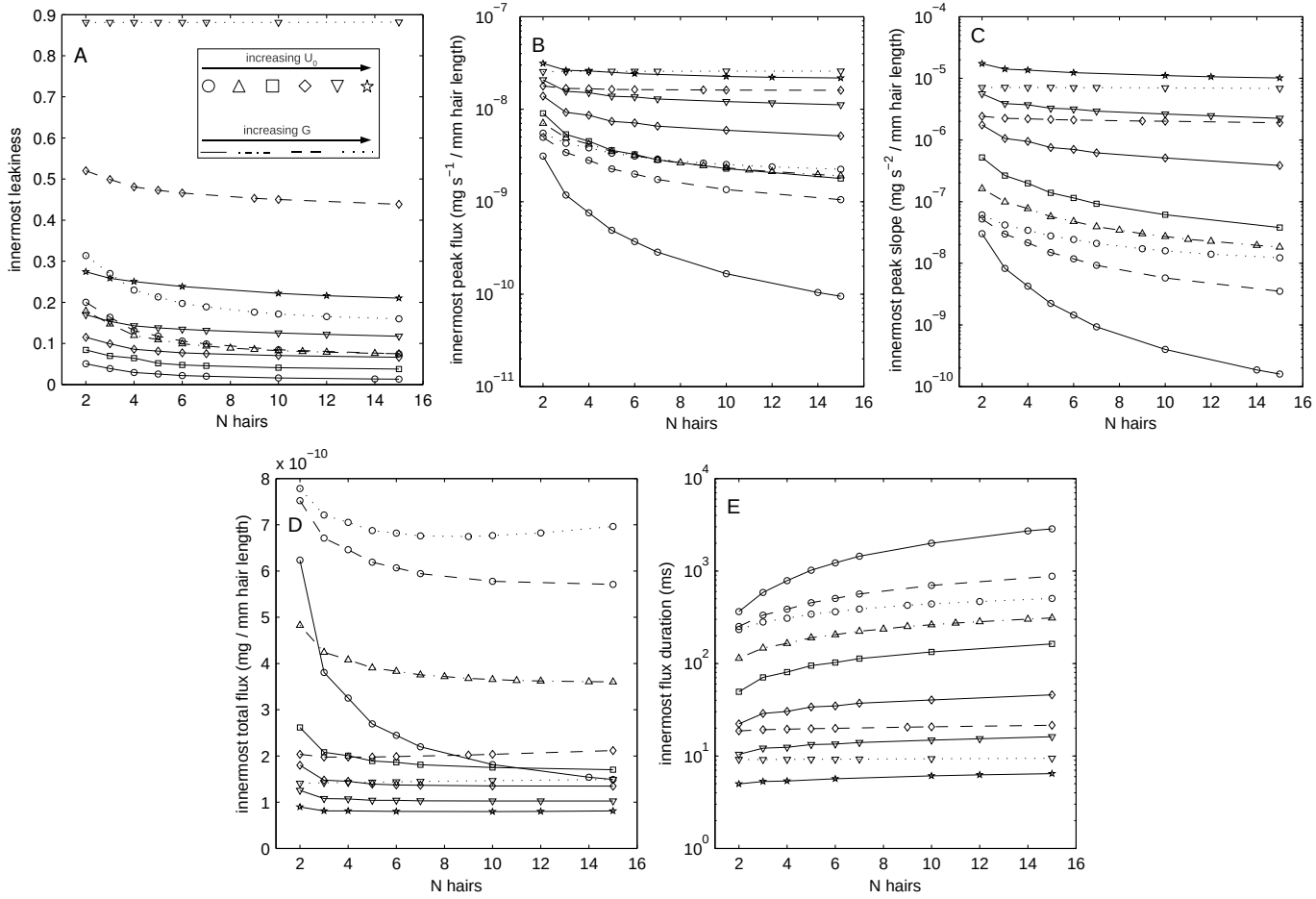


**Figure 3.11:** Sampling performance metrics for innermost hairs vs number of hairs $N$. Marker symbols indicate $U_0$ (cm/s), with corresponding $Re$ in [ ]: $\bigcirc = 0.375$ [0.1], $\triangle = 0.749$ [0.2], $\square = 1.87$ [0.5], $\diamond = 3.75$ [1], $\triangledown = 7.49$ [2], $\star = 15.0$ [4]. Lines indicate gap spacing ($\mu$m) with corresponding $G/D$ in [ ]: solid = 25 [1], dash-dot = 80 [3.2], dashed = 125 [5], dotted = 250 [10]. Trends across markers and lines are summarized in inset of A. Note logarithmic scaling on several y-axes.

likely, as hypothesized by (Gleeson et al. 1993).

### 3.4.3. Intra-array variability

The physical presence of an olfactory appendage affects how the actual environmental odorant concentration field is perceived by olfactory neurons, and this physical filtering varies throughout the array. Peak flux, peak slope, and total flux are all highest at the outer edges of the array, while flux duration is usually longest in the center. Olfactory neurons in the outer aesthetascs of an array will therefore be exposed to higher peaked, sharper odorant flux input and more total odorant molecules, but neurons in aesthetascs in the middle will be stimulated for a longer time period. Thus, aesthetascs at various positions in an array may respond differently to the same environmental odorant signal, despite containing nearly identical populations of olfactory receptor neurons. In particular, the jumps in peak flux, peak slope, and especially total flux at the outermost hairs (Figure 3.8) raises the question of how the signals from "end" aesthetacs might be processed. In species with thousands of aesthetascs such as the spiny lobster *P. argus*, such edge effects must surely be averaged out by the nervous system, but they could be important in species with rows of $O(10)$ aesthetascs such as the mantis shrimp *G. falcatus*.

Heterogeneity in the odorant sampling behavior of individual aesthetascs may be especially important if aesthetasc arrays are used to sample the fine-scale spatial structure of turbulent odor plumes, a question frequently raised in the literature (e.g., Atema 1996, Koehl 2001a). Real plumes are much more complex than the single Gaussian odorant filament studied here, and in nature one could expect to encounter odorant filaments of various peak concentrations and widths. If olfactory neurons require some minimum peak flux, peak slope, total flux, and flux duration in order to detect an odor filament, intra-array variability in sampling performance could mean that hairs near the edges of an array might detect low-concentration filaments that middle hairs miss (since peak flux, peak slope, and total flux are proportional to peak filament concentration and highest at the array edges), while hairs near the middle might detect thin filaments that outer hairs miss (since inner hairs prolong flux duration for a given filament width the most). Of course, we can only offer conjecture as to the significance of these variations in the absence of more neurobiological data.

The qualitative changes in patterns of intra-array leakiness and flux duration as sampling speed increases are fascinating, but of unknown biological importance. To put the sampling speeds of Figures 3.7 and 3.9 in some context, the spiny lobster *P. argus* flicks its aesthetascs at about 6 - 9 cm/s for the rapid downstroke (comparable to panel B in both figures) and at about 2 cm/s for the slower return stroke (comparable to panel A in both) (Goldman and Koehl 2001). The clawed lobster *H. americanus* is known to flick down at 12

- 15 cm/s (comparable to panel C in both) (Moore 1991). While aesthetasc diameters are similar to that used here (25 $\mu$m here, 22 $\mu$m for *P. argus* (Goldman and Koehl 2001), 30 $\mu$m for *H. americanus* (Moore et al. 1991a)), the morphology of both species' aesthetasc arrays is quite complex and poorly defined by a single gap size, although $G/D = 5$ has been estimated for *P. argus* (Goldman and Patek 2002). Hence, whether small enough gaps between olfactory hairs exist in nature for these transitions to be important is unclear. Even if they do occur, it is difficult to say whether the scale of variations observed is neurobiologically important without experimental data.

### 3.4.4. Comparison to a virtual sensor

The main interest of this study has been to quantify the actual (dimensional) flux metrics of various olfactory hair array configurations. Since the physical presence of the array alters the structure of an odorant filament during a sampling event (largely through viscous effects), it can also be informative to compare the actual flux metrics to those of a virtual sensor that does not affect plume structure, but instead samples it passively. We believe a virtual sensor that senses advective flux to be the most appropriate here. Specifically, the virtual sensor can be thought of as a line segment that traverses the entire array and is oriented like the array, parallel to the odorant filament (Figure 3.12). As it intercepts the odorant filament by moving toward it at $U_0$, it captures 100% of the advective odorant mass flux integrated across the line segment at a given moment. Hence, the virtual sensor can be thought of as achieving the maximum peak flux, peak slope, and total flux possible, given a sampling speed and sampling area. The flux duration of the virtual sensor is how long a sensor would experience an influx of odorant if it did not distort the odorant filament at all. Details of these calculations are given in Appendix A.

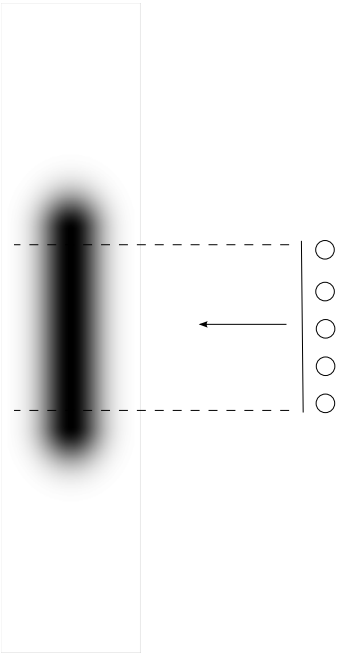

**Figure 3.12:** Schematic of virtual sensor used to normalize odorant sampling performance of a 5-hair array. The virtual sensor is a line segment the same width as the array and moves toward the odorant filament at $U_0$ as the real array would. The virtual sensor does not alter the filament's structure, however, and completely absorbs the section enclosed by the dashed lines via a convective flux.

Normalizing the flux metrics of the finite arrays by their virtual sensor analogs gives an idea of how much the real arrays are extracting compared to what is theoretically possible. Not surprisingly, very little odorant is captured by the real arrays since they are limited to capturing molecules via a diffusive flux instead of a convective flux: maximum normalized peak flux, peak slope, and time integrated flux across our entire parameter space were 0.02, 0.01, and 0.05, respectively. These maximums all occured for two-hair arrays at $U_0 =$ 0.375 cm/s [$Re = 0.1$] and $G = 25$ $\mu$m [$G/D = 1$], the lowest that we investigated, which is surprising given the low leakiness at these arrays. What little fraction of the odorant filament is absorbed, is absorbed over a relatively long period of time compared to a virtual sensor: normalized duration ranged from 1.2 (at $U_0 =$15.0 cm/s [$Re = 4$], $N = 2$) to 19 (at $U_0 = 0.375$ cm/s [$Re = 0.1$], $N = 15$), meaning that the duration of odorant flux lasted from 1.2 to 19 times as long as the advection time for the filament to move past the array at $U_0$. This temporal stretching is much more pronounced than is the case for infinite arrays (Chapter 2 of this work) because fluid is not forced through the array at relatively high speed in the case of finite arrays.

Normalized peak flux, peak slope, and time integrated flux always decrease with number of hairs, and normalized flux duration increases (not shown), unlike the behavior of some of the dimensional metrics as discussed in Section 3.3.1. However, more interesting behavior does occur in the normalized metrics versus $U_0$ and $G$, especially at the lower end of each. Trends versus $U_0$ for small $G$ are shown in Figure 3.13. The importance of $N$ on the basic shape of the peak flux (panel A) and peak slope (panel B) curves stands in contrast with the trends of the dimensional metrics versus $U_0$, for which qualitative shape does not depend on $N$ (not shown). While arrays with only a few hairs always experience decreased normalized peak flux and peak slope with increasing sampling speed, arrays with many hairs display the opposite trend. Edge effects that are only significant for arrays with few hairs may be responsible for this transition. These results again emphasize the importance of $N$ in comparing the theoretical sampling performance of different morphologies, such as mantis shrimp (small $N$, especially juveniles) versus lobsters (large $N$).

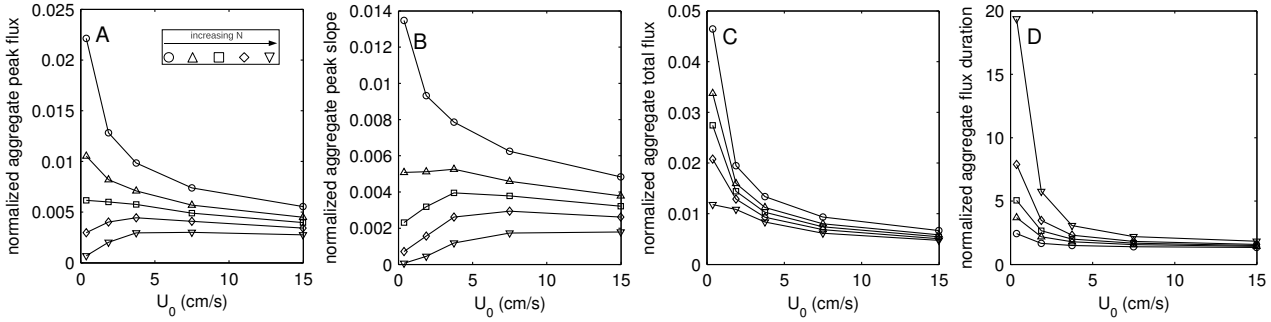


**Figure 3.13:** Trends in normalized aggregate peak flux (A), peak slope (B), total flux (C), and flux duration (D) vs $U_0$ [from $Re$ = 0.1 - 4] for $G = 25$ $\mu$m [G/D = 1] and selected $N$. Markers indicate $N$: $\bigcirc = 2$, $\triangle = 3$, $\square = 4$, $\diamond = 6$, $\triangledown = 15$, summarized in the inset of (A).

The curves in Figure 3.13 also suggest that all the normalized flux metrics might asymptotically approach the same values as $U_0$ increases, no matter how many hairs are in the array. This may be due to thinning boundary layers as flow speed increases, so that each hair behaves independently, and thus number of hairs eventually loses significance since the normalization accounts for total array surface area. Hence, flicking an olfactory appendage at ever faster speeds is expected to yield diminishing returns of the flux metrics we studied, compared to what is theoretically achievable.

These data complement the dimensional flux metrics by providing more evidence that biological olfactory hair arrays operate in a transitional odorant transport regime. While changes in $U_0$ and $G$ can fundamentally alter how the actual peak metrics (peak flux, peak slope) of finite arrays are affected by changes in $N$, here we see that changes in $N$ can

fundamentally alter behavior versus $U_0$ in terms of performance relative to a virtual sensor. Whether these transitions are important neurobiologically can only be answered with experimental data.

## 3.5. Summary

The morphology and kinematics of hair-bearing animal appendages can be critical in determining their function. In the case of the olfactory antennules of marine crustaceans, previous work has shown how the geometry of the aesthetasc array and flicking speed of the appendage often result in a transitory flow regime and discrete sampling of the fluid environment, or sniffing. Although odorant molecules act as passive scalars carried by the fluid flow, odorant sampling performance can exhibit additional variability not easily predicted from simple descriptors of fluid flow alone (e.g., leakiness). Here we show that fundamentally different trends in odorant sampling performance, not predicted by leakiness alone, can occur over a biologically relevant parameter space.

Our data emphasize the importance of sampling speed, gap size, and number of hairs on odorant sampling performance of idealized olfactory hair arrays. The effects of changes in hair number can be strongly modulated by sampling speed and gap size, so that all three parameters are needed to make accurate predictions. This can be important not only for making comparisons across species, but also for different life stages of the same species.

Numerical simulations can tell us the scale of variation likely to occur in the odorant sampling performance of real appendages of different species and life stages, but ascertaining the relevance of this variation is difficult. Normalizing results to the performance of a virtual sensor allows us to compare with what is theoretically possible, but in general, most organisms seem to thrive without achieving anywhere close to theoretical maximum performance. More experimental data for real neurons exposed to realistic odorant plumes is therefore required to determine the neurobiological significance of these results.

## Acknowledgements

This research used resources of the National Energy Research Scientific Computing Center, which is supported by the Office of Science of the U.S. Department of Energy under Contract No. DE-AC02-05CH11231.

# 4. Real Morphology

## 4.1. Introduction

Real olfactory antennules vary widely in morphology, and a resemblence to a straight row of cylinders is the exception rather than the rule. For instance, crabs have toothbrush-like tufts of aesthetascs that deform as the antennule is flicked, and mantis shrimp have multiple rows of aesthetascs (Koehl 2006). The spiny lobster *P. argus* has been well studied but has an exceptionally complex aesthetasc morphology. The aesthetascs are arranged in a complex 3D pattern such that the hairs are nearly parallel viewed at the base, but form a zig-zag viewed at cross sections higher up (Goldman and Koehl 2001). The zig-zag pattern has been suspected to channel flow through the aesthetascs due to the orientation of the antennule as it is flicked, as shown in Figure 4.1 (Gleeson et al. 1993). The aesthetascs are also enclosed by a cage of guard hairs that are known to modify the flow encountered by the aesthetascs (Reidenbach et al. 2008). Hence, a single row of hairs might not be an accurate model of this real geometry.

To facilitate quantifying the differences between idealized geometries and a real olfactory appendage, a 3D tomographic scan of a *P. argus* antennule was obtained (Section 4.2). From this, the surface geometry can be extracted and eventually used in computational models of flow and odorant transport. An image segmentation algorithm designed to extract the surface geometry is presented in Section 4.3 along with some preliminary results. Since complete segmentation results in a form suitable for numerical simulations are not yet available, several key measurements of the morphology were taken manually (Section 4.4) to facilitate 2D numerical simulations of flow around and odorant transport to a single V-formation of aesthetascs (Section 4.5). These represent only a slightly higher level of geometric complexity than the straight rows studied in Chapters 2 and 3, but can provide some basic insight into the effects of the real zig-zag pattern on odorant sampling performance.

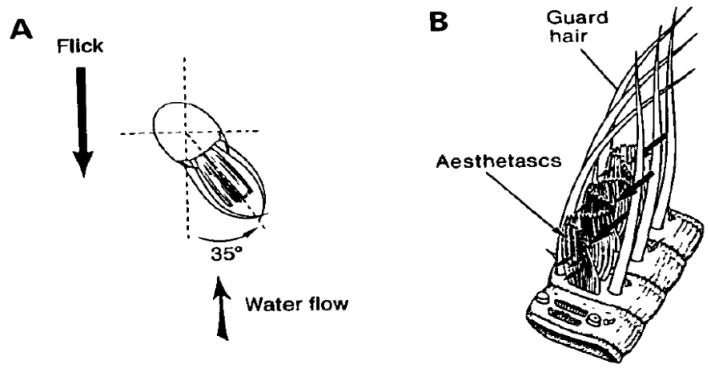


**Figure 4.1:** (A) Cross-sectional view of the lateral filament (right antennule) illustrating the orientation of the aesthetasc tuft relative to the direction of a flick. Note that, during a flick, water enters the tuft at an angle of approximately 35°. (B) Direction and pattern of water flow (arrows) through the V formations of aesthetascs during a flick. Reproduced from (Gleeson et al. 1993).

## 4.2. 3D Scan

### 4.2.1. Specimen acquisition

Several *P. argus* specimens were ordered from a commerical seafood supplier, FloridaLobster.com, and shipped overnight to the Electron Microscope Lab at UC Berkeley in an ice-packed insulated container. The lateral flagellums were removed near the base of the aesthetasc-bearing region and, while submerged in artifical seawater (Instant Ocean), examined under a dissecting microscope. The aesthetasc arrays on the majority of antennules appeared to be clogged with green flocs (perhaps algae), but a few appeared to be in good condition and underwent subsequent treatment. The samples were first fixed in 2% glutaraldehyde in 0.1 M sodium cacodylate and rinsed with 0.1 M sodium cacodylate buffer. Then two samples were stained with 1% osmium tetroxide while two were left unstained. All samples then underwent an ethanol dehydration series and supercritical drying as per standard protocol at the Electron Microscope Lab at the University of California, Berkeley. After critical point drying, the zig-zag pattern of aesthetascs was still identifiable under dissecting microscope, indicating that the samples were not damaged by these procedures. Lastly, one of the osmium-stained samples was also sputter-coated with a gold/palladium mixture to try to increase the signal to noise ratio during subsequent X-ray tomography.

### 4.2.2. Micro X-ray tomography

Hard X-ray microtomography was performed at beamline 8.3.2 at the Advanced Light Source at Lawrence Berkeley National Lab. Briefly, X-ray computed tomography involves the collection of many 2D X-ray images (slices) around a single axis of rotation in order to reconstruct a 3D image of an object, including its internal structure. Although the internal structure of the antennule was not of interest here, this imaging technique is possibly the only one currently able to achieve the micron-scale resolution necessary to resolve individual aesthetascs in 3D. Electron microscopes have been used to obtain 2D images of antennule morphology, but are typically incapable of generating a 3D scan. Unfortunately, X-ray tomography works best on dense materials such as bones and teeth, and is not well suited for chitinous materials such as crustacean antennules. We therefore attempted the aforementioned heavy metal treatments on some specimens to try to increase contrast.

A beam energy of 15 keV was used to scan small sections of both the osmium stained and sputter coated antennule, and a control specimen that was not treated with heavy metals. The metal treatment did not seem to significantly enhance contrast, and in fact, seemed to introduce a V-shaped artifact near the base of the aesthetascs that may have been a layer of sputter-coated metal. Therefore, the sample without any heavy metal treatment was used for a full scan of an approximately 1 cm section of antennule. Scanning such a long section was prudent because although each aesthetasc is only ~20 $\mu$m diameter, the long guard hairs are oriented at an acute angle relative to the antennule, each spanning a few mm. This large range of spatial scales posed another problem for tomography, as there are tradeoffs between field of view and resolution. To get around this problem we tiled five scans vertically, each spanning 2 mm of antennule, with a voxel size of 0.888 $\mu$m. The entire scan took several hours overnight, and because this facility is in high demand, the scanning of multiple specimens is not currently feasible.

Some pre-processing of the images is needed before 3D reconstruction. First a background normalization was done to account for variations in radiation intensity. Then a de-ringing routine was performed to reduce ring-like artifacts that often appear after reconstruction. Lastly, sinograms (Radon transforms) were created and input to a parallel 3D reconstruction routine in a commerical software package (Octopus, inCT, University of Ghent, Belgium).

A single, representative reconstructed slice is shown in Figure 4.2, where the slice is oriented perpendicular to the antennule. Five tiles, each composed of 2000 images similar to that in Figure 4.2, are stacked to form the entire 3D volume of data. A representation of one of these tiles is shown in Figure 4.3, where the volume data is translucent and a slice *parallel* to the antennule and at the base of the hairs is shown (interpolated from the 3D dataset in the commerical visualization program Avizo, VSG). In the slice, the cross sections of a

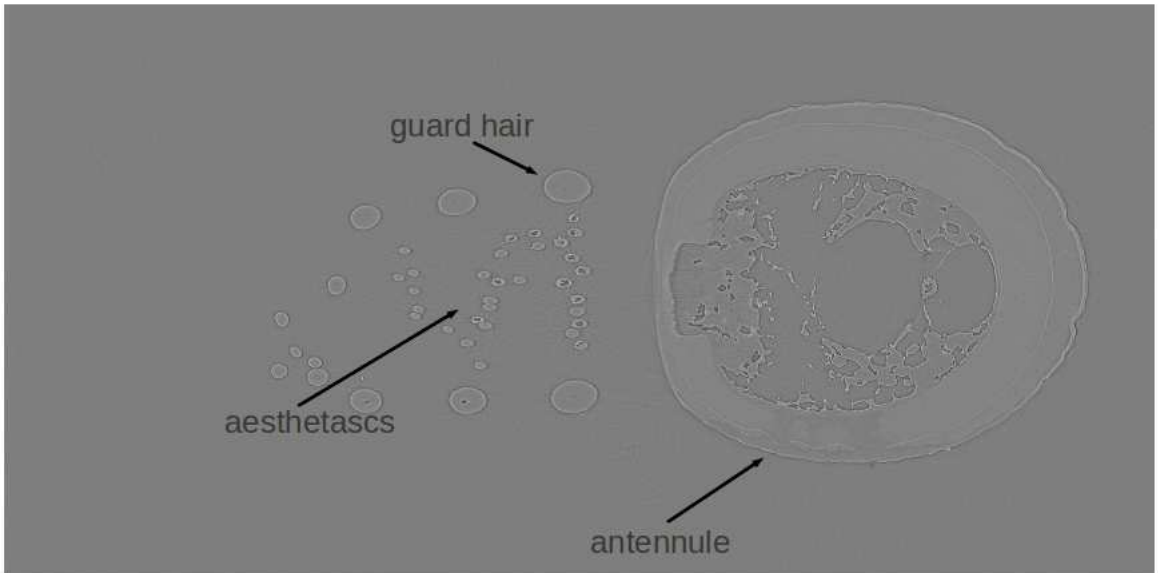


**Figure 4.2:** A single representative slice of the 10,000 making up the 3D tomographic data set. The slices are perpendicular to the antennule.

few salient features are labeled: the large guard hairs, the rows of aesthetascs, and the thin asymmetric sensilla. Although the identity (left vs right) of the antennule was unfortunately not recorded at the time of specimen collection, the location of the asymmetric sensilla and the direction of tilt of the aesthetascs and guard hairs (to the right in Figure 4.3) indicate that this is a right antennule (Gleeson et al. 1993, Goldman and Koehl 2001).

## 4.3. Image segmentation

### 4.3.1. Overview

The term "reconstruction" in the preceding section is somewhat misleading, as the objective of this work is to obtain a digital 3D representation of the *surface* geometry of the antennule,


**Figure 4.3:** Visualization of 3D tomography data for a right antennule, sliced parallel to antennule near bases of hairs. The entire scan consists of five such sections tiled along the antennule. The distal end of this section is to the right, and water would flow into the page during a flick downstroke.

guard hairs, and aesthetascs. The reconstructed dataset, however, consists of far too much information, as it is a filled *volume* of intensity values. Hence, additional processing is necessary to extract only the surface of interest. The simplest method is an intensity threshold; ideally, there is very high contrast between the sample material and air, and the correct choice of the threshold value results in a continuous isosurface. Unfortunately, a thresholding approach by itself is of little practical use with this data because of the carbonacaeous nature of the specimen. As shown in Figure 4.4, numerous disconnected islands and clumps of "noise" are caused by insufficient differences between the X-ray absorbance of the sample versus air and dust. Although the desired geometry is still easily recognizable to the eye, it is not connected or smooth enough to permit use in fluid dynamics simulations. Attemping to remove the artifacts by working directly with the 3D volume data is not computationally feasible or practical due to the shear amount of data (about 60 gigabytes).

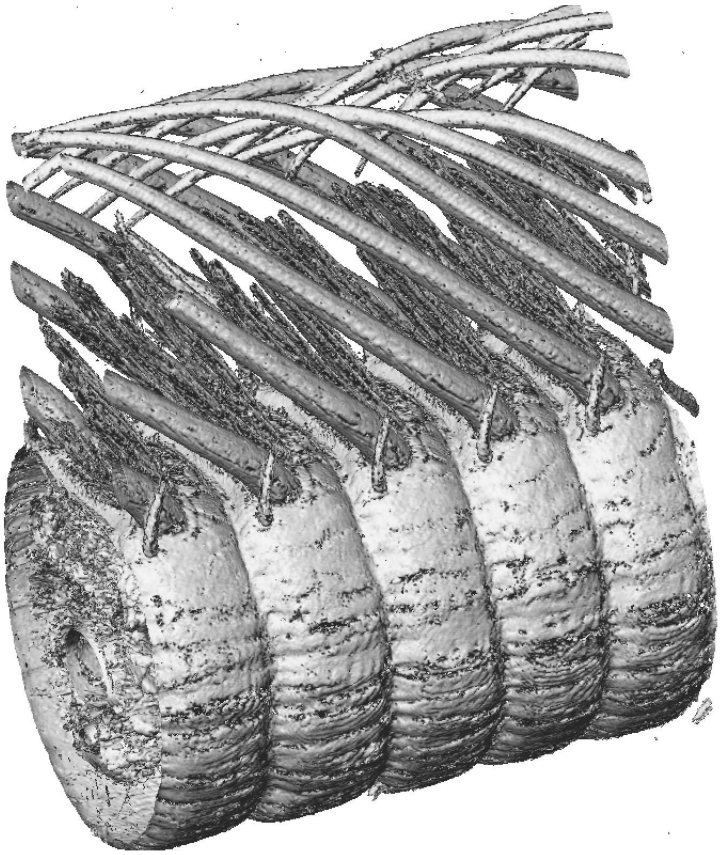

**Figure 4.4:** Isosurface formed by thresholding one tile of volume data. Data has been downsampled by a factor of 6 due to computer memory limitations.

We opted to work with each 2D image (or slice) sequentially, semi-automatically identifying the outlines of the cross sections of the aesthetascs, guard hairs, and antennule (Figure 4.2). A stack of such 2D outlines can then be combined to form a 3D surface. This process of finding shapes in images is part of the field of image segmentation, and is generally a very difficult problem in biological images. Initially, a number of existing segmentation methods were briefly tested: the Hough transform desgined to find circles, watershed segmentation, and a few other methods such as active contours. However, these high-level segmentation algorithms were very sensitive to noise in the images and did not result in clearly separated hair outlines. We therefore decided to use simple thresholding to binarize each image and isolate pixels belonging to each hair (though simple edge-detecting routines might work as well or better - see Section 4.3.5). The result of thresholding a typical image (i.e., Figure 4.2) is shown in Figure 4.5. Unfortunately, it is clear that this method alone also is not sufficient to segment the hairs: it includes both pixels within the hairs as well as pixels around their outer boundaries, and the latter are frequently not connected in a closed curve. In light of these problems, as well as small variations in hair shape from slice to slice (due to both real variation and random noise), we opted to fit geometric primatives to each hair. This method allows limits to easily be placed on the changes in hair geometry between slices, and generally puts "smoothness" constraints on the segmented surface. It also has the inherent requirement of keeping track of each hair's identity from slice to slice, which would be necessary if the odorant flux to individual aesthetascs were desired output from future numerical simulations.

Figure 4.5 suggests that the cross sections of the aesthetascs and guard hairs could be well described by ellipses, and that the cross section of the antennule is also close to elliptical, but with one side flattened (and perhaps well approximated by a cubic spline). There is also little change from one slice to the next, so a set of elipses fit to the objects in one image would likely be a good starting guess for the best fit ellipses for the same objects in the next image. Therefore, instead of attempting to automatically locate these objects in each image independently, our general strategy is to manually segment each object (ideally once, but in practice, in a number of slices) and then step through each consecutive slice one by one, using the previous set of fits as an initial guess for the new fits. To briefly summarize the algorithm: After the initial human-assisted segmentation of a slice, the next slice is thresholded to generate a new set of pixels to fit, and the previous set of fits is overlayed on these points. The old fit is then expanded and contracted slightly (e.g., an ellipse's major and minor axes are increased and decreased) in order to account for the shifts in hair position and size between images. The thresholded pixels in this annular region are what each new geometric primative are fit to. The new fits are stored, overlayed on the next thresholded image, and so on. Details of the algorithm are described in the following sections.

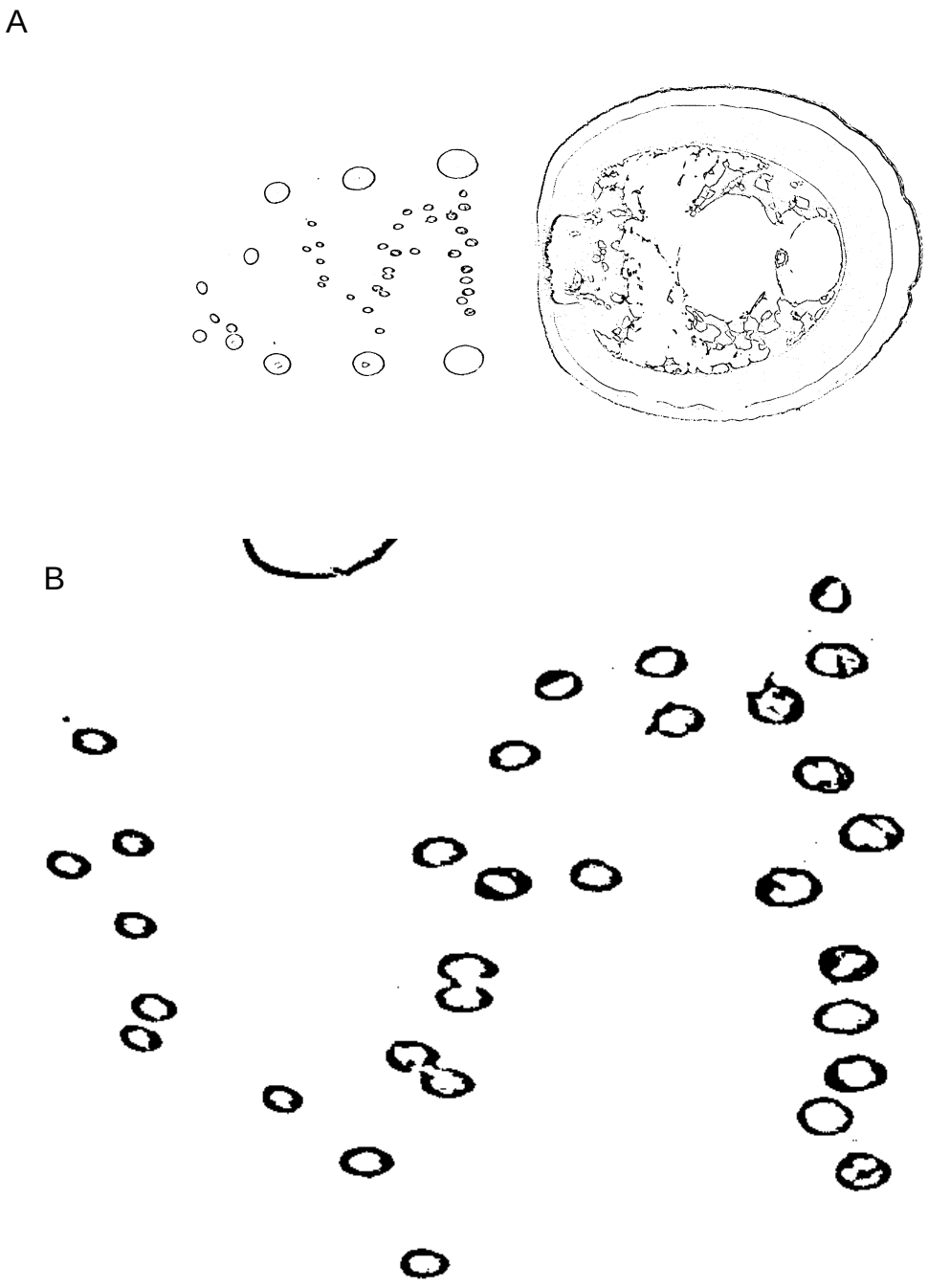


**Figure 4.5:** (A) Pixels corresponded to the thresholded image in Figure 4.2. (B) Zoom-in on region containing the aesthetascs.

### 4.3.2. Segmentation of antennule

The following description of the antennule-fitting algorithm is summarized as pseudocode in Listing B.1 of Appendix B.

Since the right part of the antennule is well approximated by an ellipse, we first fit an ellipse to the antennule in each slice. The initial fit was done by thresholding an image and manually masking the points (via imfreehand() in the Image Processing Toolbox, MATLAB 2011a) along the edge of the antennule, excluding points inside it and points along the flattened left portion. An ellipse was then fit to these points using a non-linear least squares (geometric fitting) routine (Brown 2007). Thereafter, the ellipse fit from the previous slice was overlayed on the thresholded next slice, and expanded and contracted (via its major and minor axes) by five pixels to create an annular region. The points in this annular region were fit to a new ellipse, and so on. This method automatically excludes points along the flattened left side from the ellipse fit.

Next, in each slice, it was necessary to explicitly locate where the actual antennule shape deviated from the fitted ellipse so that this section could be replaced with a spline. Thus, a "top" and "bottom" cutoff point must be defined for each slice. Since the procedure is nearly identical for each, only one case is dicussed from here on. In addition, since the cutoff point ($x_c$ , $y_c$) is constrained to lie somewhere on the fitted ellipse, it suffices to just find the x-coordinate of the cutoff point, $x_c$, and then determine $y_c$ from the equation of the ellipse. A starting guess $x_g$ was chosen by manual inspection and the region in which the break occured was assumed to be bounded by $x_g - b \leq x_c \leq x_g + b$ where $b = 45$ pixels worked well. A smaller interrogation window was then formed by masking the annular region bounded by the fitted ellipse +/- 10 pixels, and additionally constrained by $x_w - w \leq x \leq x_w$ where the window's length $w$ was 10 pixels and its right edge location $x_w$ initially equaled $x_g + b$, the right edge of the search domain. The right edge of the window $x_w$ was then looped from $x_g + b$ to $x_g - b$. During each loop iteration, the interrogation window moved to the left, and the number of thresholded pixels in the window was counted. If there were fewer than 10 pixels, the cutoff point was declared to be $x_c = x_w + offset$. The large offset of 70 pixels was chosen as a conservative measure to ensure that the elliptic section of the fit did not continue past the region of excellent agreement with the data. If the break condition on number of pixels was never satisfied, $x_c$ was very conservatively chosen to be $x_c = x_g + b + offset$; this occasionally happened while a guard hair was merging into the antennule. Setting a new initial guess $x_g$ to be $x_w$, this procedure was then looped over all slices. For each slice, the y-coordinate of the cutoff point $y_c$ was found by substituting $x_c$ into the equation of the fitted ellipse.

Once the cutoff points for the antennule ellipse in each slice are known, a cubic spline can be fit to the points that do not conform to the ellipse. Throughout the slices, the shape of the

left side of the antennule varies from slightly convex, to nearly flat, to concave, and a cubic spline can easily approximate all of these shapes. The challenge here is to allow sufficient degrees of freedom (i.e., knots) that the spline can follow the overall variation in antennule geometry, but not so much freedom that noise and small bumps cause it to oscillate out of control (i.e., Runge's phenomenon). After substantial trial and error, a cubic spline with eight knots was chosen, with the knots equally spaced in the vertical direction. As with the ellipse fitting, the routine was manually started by masking thresholded points in the appropriate left-hand region of the antennule, and fitting a spline to these points (D'Errico 2010), subject to the constraints that its values and slopes at both endpoints matched those of the ellipse fitting the rest of the antennule. These constraints result in a smooth, closed curve approximating the antennule geometry. Note that because the fitted spline is vertically oriented, the spline is a function of the form $x(y)$ in the reference frame of the image. The method used to automatically step through the slices is as follows: An annular region was masked out of the new slice by shifting the old spline left and right. This was accomplished by uniformly sampling the old spline function to yield 1500 points, and then adding and subtracting pixels from each x-coordinate. Since the spline was found to evolve through the slices differently in the middle region (where the aesthetascs are borne) versus at the ends (where the guard hairs are borne), the number of pixels to add or subtract differed accordingly: In the middle region, 7.5 pixels were subtracted and 5 added while in the outer regions, 6.5 pixels were subtracted and 5 were added. These seemingly minor differences helped to facilitate "absorption" of aesthetascs into the antennule as they merged into it through the slices. Thresholded pixels within this mask, and between the cutoff points of the antennule ellipse, were then fit to a new spline, and the process continued through the slices.

### 4.3.3. Segmentation of aesthetascs and guard hairs

Like the antennule, the much smaller aesthetascs and guard hairs are well approximated by ellipses, with the advantage that no splines are needed. Unfortunately, here there is a much more difficult problem: because aesthetascs often touch or nearly touch, especially as they approach the antennule (at their bases), the fitted ellipses will tend to overlap as they evolve through the slices. Simultaneously, one ellipse will tend to engulf its neighbor by gradually "stealing" its underlying pixels. The touching aesthetascs in Figure 4.6 are a good example of when this tends to happen. To partially mitigate this problem, a specialized ellipse fitting routine was created that fits multiple ellipses to multiple hairs at once, with the constraint that there is no overlap between any ellipses. The following detailed description of the method applies to both aesthetascs and guard hairs, though fits of the guard hairs experience this problem much less often. A pseudocode description of the key parts of the algorithm can be found in Listing B.2 of Appendix B.

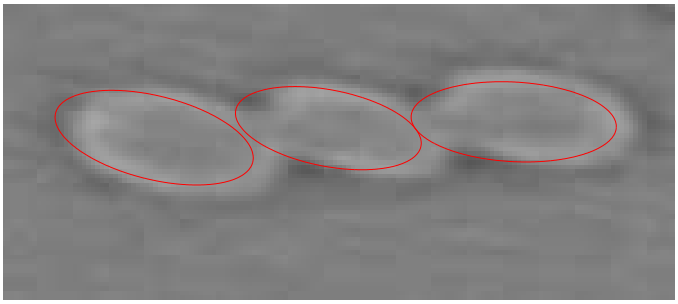

**Figure 4.6:** Example of a group of touching aesthetascs that causes automatic segmentation (indicated by red ellipses) to fail. Small perturbations in each fit tend to grow from slice to slice, and the segmentation routine rarely recovers without manual intervention.

To begin, each hair in a slice is manually segmented by masking thresholded pixels along its outer edge and fitting an ellipse via nonlinear least squares, as was done for the antennule. Note that ellipses manually fit to nearby hairs in this way never overlap in practice, so a simple fitting routine is sufficient here. Then, the first step in the automatic fitting routine is a check to determine which hairs, if any, are close enough to each other to warrant simultaneous fitting. This is accomplished crudely but effectively by expanding each known ellipse's major and minor axes by 2 pixels, sampling 100 equally spaced points on each expanded ellipse, and checking analytically whether any of these points lie within another expanded ellipse. Then the hairs that are close to overlapping are sorted into groups such that every hair in a group is connected continuously to every other hair in that group; a typical example is a row of very close aesthetascs just before it merges into the antennule (third pane in Figure 4.7). In a typical slice there are many groups containing just a single hair, and a few groups each containing a few to several nearly overlapping hairs that must be fit together to prevent overlap.

As with the ellipse fit of the antennule, the points to fit for each hair are determined by masking the annular region between expanded and contracted versions of the previous ellipse (here, the major and minor axes are grown and shrunk by 4 pixels each). Since each image is very large (3500 x 1820 pixels), and there are many aesthetascs to fit in each image, this was sped up drastically by performing this masking procedure on a small rectangular subregion of the image surrounding each hair. Within a nonlinear least squares fitting routine (implemented using fmincon() in the Optimization Toolbox, MATLAB 2011a), each point's error is then calculated by determining its distance to the closest ellipse according to the ellipse parameters during the current iteration. To save CPU time, these distances

were not calculated from every point to every ellipse; instead, points were initially classified by keeping track of which ellipses' annular region(s) they fell within, and distances were only calculated to those nearby ellipses.

To obtain an objective function to be minimized, the sum of the squared distances for all masked points was computed. However, a weighted sum was used: squared distances belonging to points inside the closest ellipse were given a weight of 0.25 while squared distances belonging to points outside the closest ellipse were given a weight of 0.75. This has the effect of biasing the fit so that more points are inside versus outside than would occur in the unbiased case. Since many of the points being fit are, in fact, inside each hair and not along its outer boundary, biasing the fits in this way caused the fitted ellipses to better approximate the true sizes of the hairs. Edge detection instead of thresholding might be an alternate solution to this issue, and is discussed further in Section 4.3.5. Finally, a constraint is imposed on the fits: none of the ellipses in a group are allowed to overlap with each other, or with hairs that are already segmented and not being fit. Overlap is checked via the method described above.

Convergence of the optimization problem was facilitated by using the previous ellipses' parameters as the starting guesses for the new fits, and by bounding the new ellipse parameters to be within a small range of the old values. Even still, fmincon often failed to converge, but this problem was mitigated by introducing a small random perturbation to the initial guess for the center coordinates of each ellipse. By doing this within a loop, a center location was soon found that led to convergence of a solution.

Unlike the antennule, each aesthetasc and guard hair only exists in the images for a subset of all slices. Therefore, they must be removed from the fitting routine if they disappear due to leaving the plane of the slice (at their tips) or if they merge into the antennule (at their bases). Note that the segmentation algorithm can operate going in either direction through the slices (along the antennule), so that a hair is usually initially segmented manually somewhere between these bounds and then automatically segmented in both directions away from this starting slice. To account for the disappearence of a hair at both the tip and base, the number of points to be fit to each hair is summed, and if less than a threshold (55 works well), it is ignored from then on. In addition, points that are inside the already-segmented antennule are discarded from the fits since aesthetasc and guard hair structure becomes incoherent inside the antennule.

Finally, substantial speedup can be realized by fitting the hairs in a given slice in parallel, given the multi-core configuration of modern computers. Since each group of connected hairs can be reasonably assumed to not affect the ellipse fits of any other group, the fits for each group can be done independently. Hence, the algorithm was parallelized using the parfor (parallel for loop) construct in MATLAB 2011a's Parallel Computing Toolbox. This

led to a factor of 3.8 speedup using the four cores of a modern CPU. Since this type of problem is "embarrassingly parallel," it would be expected to scale very well with more processors.

### 4.3.4. Results

Several segmented slices are shown in Figure 4.7. The ellipse fits of the antennule, aesthetascs, and guard hairs in these images are quite good, and the cubic spline that fits the left side of the antennule can follow the changes in morphology (convex to flat to concave) through the slices very well. Although many aesthetascs are touching in the various images, the ellipse fits are always guarenteed not to overlap due to the constraint imposed by the customized fitting routine. However, the algorithm did not automatically segment all ~300 images between the first and last successfully. Instead, a number of manual interventions were required for aesthetascs that were close together. If the error in any fit became too large (cases similiar to Figure 4.6, identified by visual inspection), the routine was stopped, the poor fits deleted, and manual segmention of the offending hair(s) was done for one or more slices. When the automatic routine was restarted, the manual fits, taken as given and skipped by the algorithm, tended to stop errors from growing uncontrollably between slices.

Figure 4.8 shows a reconstructed section of the antennule that was created by sampling the segmented outlines in each slice and creating a 3D point cloud. The major difference between this and Figure 4.4 is the smooth nature of the surface, since it is derived from analytical curves.

### 4.3.5. Future algorithm improvement

There is much room for improvement in the current image segmentation algorithm. One promising area is the calculation of the initial guesses for each ellipse. Currently, the ellipse parameters of the previously segmented slice are used, with small perturbations to the center coordinates to help numerical convergence. However, this is not optimal since it does not use any information from any other slices, whether those slices were automatically or manually segmented. A better initial guess would incorporate the values of the ellipse parameters from several other slices in both directions, perhaps giving more weight to slices that were manually segmented. This would be most beneficial in the common case of hairs that touch throughout many slices. In these cases, the algorithm will often cause one hair to gradually displace the other (Figure 4.6), and the situation usually worsens until one or more fitted ellipses no longer "owns" enough pixels and disappears. The current solution

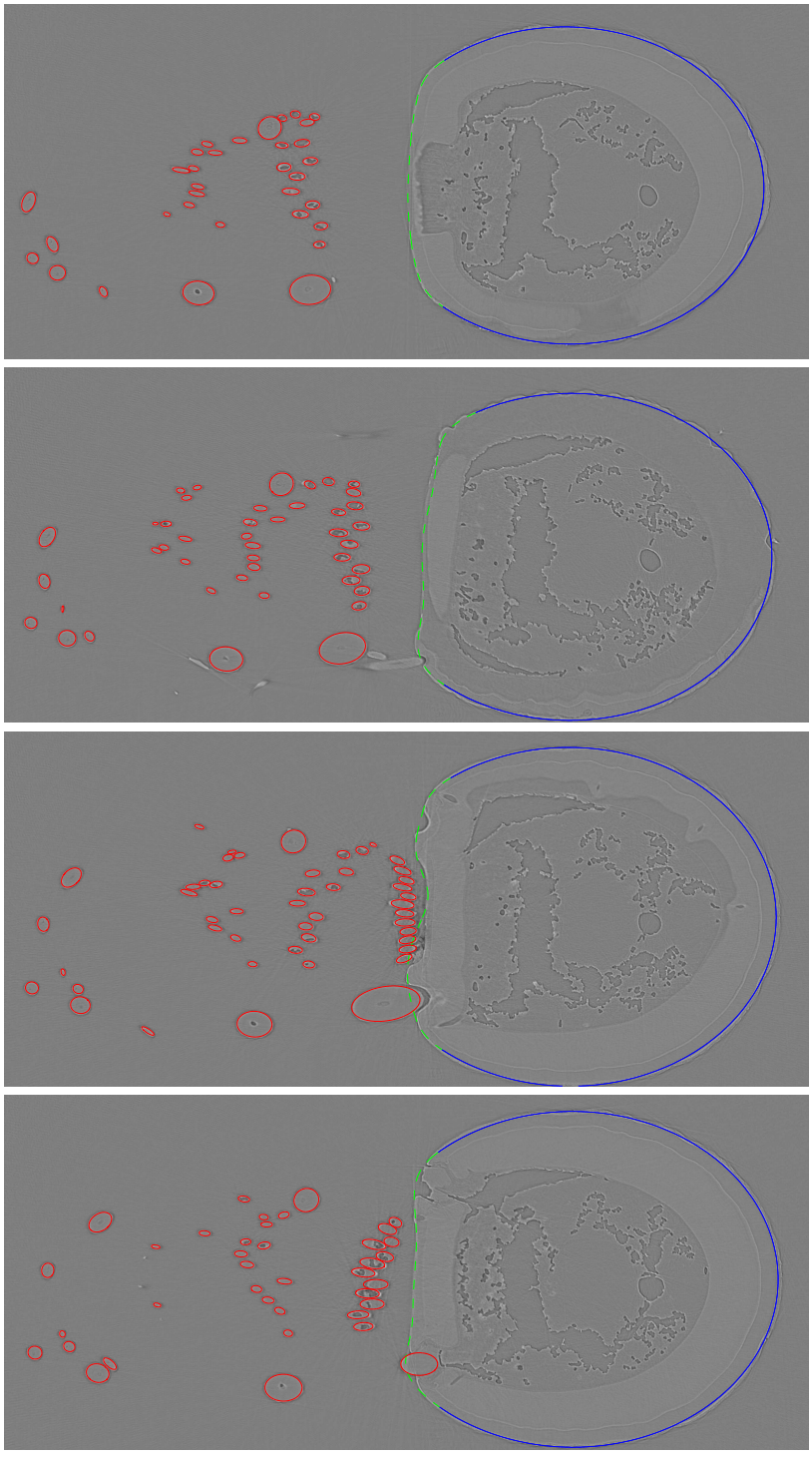

**Figure 4.7:** Series of four segmented slices spaced 100 slices (approximately 90 $\mu$m along the antennule) apart. Elliptic-fit region of antennule is in blue, spline-fit region of antennule is in green, and aesthetascs and guard hairs are in red.

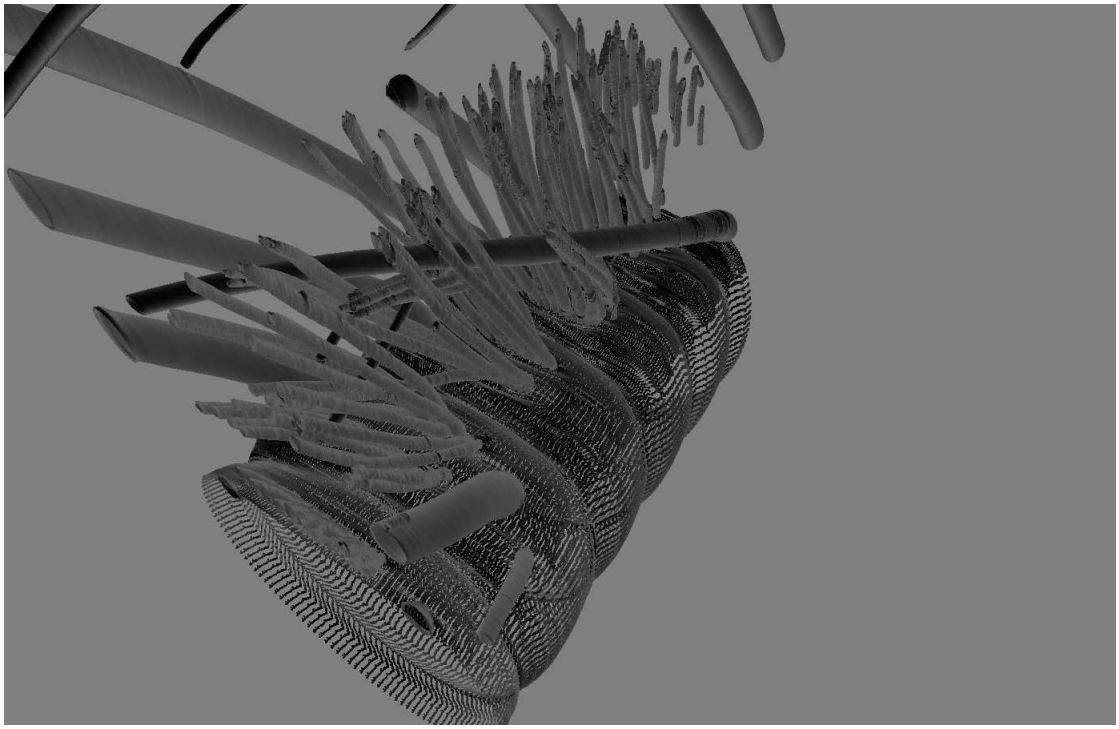

**Figure 4.8:** Rendering of a point cloud sampled from the segmented antennule, guard hairs, and aesthetascs in a single tile of data. This tile corresponds to the only section of antennule that was missing some guard hairs (right side of image).

to this problem is to manually segment the hairs frequently when they are touching, every few slices and sometimes even every slice. The algorithm then fills in the intervening slices by starting at a manually segmented slice and proceeding backwards or forwards. The frequency of manual intervention could likely be reduced if the intial guesses for a given slice were interpolated (linearly or with a spline), using the information from many slices in both directions, backwards and forwards.

One might ask whether it would be easier to segment the volume data by using 2D slices oriented differently than normal to the antennule. For instance, slices oriented parallel to the antennule (such as those in Figure 4.9 of the next section) can encompass all the aesthetascs at once, and result in more circular hair cross sections which might be easier to segment. However, hairs would touch just as often in this orientation than any other, so the problem of fitted ellipses or circles gradually displacing each other through the slices would undoubtedly still exist. In addition, segmenting the antennule would become an entirely different and perhaps more difficult problem since it would now be represented as two parallel curves instead of a single closed curve. Hence, any slice orientation seems to have its strengths and weaknesses.

While the current segmentation method uses a simple intensity threshold to binarize the images and generate points to fit ellipses to, there are other options. Preliminary evidence shows that an edge detecting routine results in a binary image containing a ring of points around the outer edge of each hair, plus an inner ring of points inside the hair that delineates some internal structure. This set of points could easily replace the set of points generated by thresholding, with the possible advantage of there being far fewer points to fit (edge detection results in edges one pixel thick), and thus some computational savings. However, this approach might also be less robust in the face of outlier points and other anomalies, as each pixel would have a much higher weight.

Once segmentation of all the 2D slices is complete, there is still the practical task of assembling this stack of cross sections into a 3D representation that can be used for boundary conditions in a CFD simulation. This may be somewhat dependent on the particular CFD software or code used, but there appear to be two main approaches. While the stereolithography (STL) format is widely compatible, it represents a surface as a triangular mesh, so that a very large number of triangles is needed for an accurate representation of a complex surface. An alternative is a native computer aided design (CAD) format such as ISO 10303 (informally known as STEP). Formats such as STEP represent solid geometry using simple mathematical constructs, and freeform curved surfaces are often represented and stored analytically as non-uniform rational B-splines (NURBS). A crude comparison can be made between formats for images and these 3D geometry formats: bitmap images such as JPEG are to STL surfaces as vector graphics such as SVG are to NURBS surfaces. One must make sure that an STL surface used for boundary conditions is resolved enough to not introduce

too much error in the simulation, whereas a NURBS surface is "infinitely" resolved. However, an STL surface is likely to be much easier to extract from the segmented 2D slices than a NURBS surface. While a triangular mesh can be fit to a point cloud formed by sampling points along the segmented curves in each slice (such as that in Figure 4.8), fitting a NURBS surface to a point cloud is a very difficult reverse-engineering problem. While commerical software that claims such capabilities exists (e.g., Creo Reverse Engineering Extension), the technology is relatively new. Since the segmented slices are actually composed of mathematical constructs such as ellipses and splines, it may seem natural and obvious to utilize this information to construct a 3D NURBS surface. Unfortunately, no software currently exists that is designed to do this, but could conceivably be created.

## 4.4. Morphometrics

### 4.4.1. Overview

Since segmentation of the entire 3D dataset is a difficult and time consuming task, a number of simple measurements of the aesthetasc geometry were taken to characterize important features and the variability of those features within a single antennule. Specifically, the zig-zag arrangment of aesthetascs is a conspicuous feature of *P. argus* antennule morphology and has been hypothesized to channel flow through the gaps between hairs (Gleeson et al. 1993). This is because, as shown in Figure 4.1, the aesthetascs are oriented in a ventrolateral position along the lateral antennule filament during the flick downstroke (Gleeson et al. 1993). Although many features of the zig-zag pattern have been measured previously (Gleeson et al. 1993, Goldman and Koehl 2001), some features that are likely to be very important (e.g., gaps between hairs) have not yet been well quantified. Thus, these measurements will enable more accurate predictions to be made of *P. argus*'s odorant sampling performance.

### 4.4.2. Methods

Measurements were taken by loading each 3D chunk (of five) of the tomography dataset into the 3D data visualization software Avizo 6.2, and viewing a slice taken at an oblique angle, parallel to the antennule and cutting through the aesthetascs. Since there is substantial variation in the geometry of the aesthetasc array throughout its height, two sets of slices were taken: the first located about 315 $\mu$m above the antennule surface, and the second about 660 $\mu$m above. The first slice cut through the aesthetascs at a height slightly less than halfway to the tips, while the second slice was located just below the tips.

To facilitate calculation of distances (i.e., diameters and gaps) and angles, the aesthetascs in each image were manually segmented using freehand masks and nonlinear least-squares ellipse fits, according to the same method employed in Section 4.3.3. During manual segmentation, the location of each aesthetasc was recorded, and hairs were ordered (traveling along each line segment of the zig-zag) and grouped (as belonging to a certain row of the zig-zag). This grouping could be highly subjective sometimes, as the aesthetascs in our specimen often deviate substantially from a regular zig-zag pattern. Segments of the zig-zag that were near the edge of an image and not in full view were not quantified, nor were segments that bore very little resemblence to an identifiable pattern (common in slices taken at the tips).

The aesthetascs were assumed to be circular cylinders, so that the minor axis of each ellipse was taken to be that aesthetasc's true diameter, $D$. Using the recorded ordering and grouping of the hairs, gap lengths ($G$) between the hairs in each row were calculated as the shortest distance between each pair of ellipses (Oldenhuis 2010). Gap lengths were also calculated for the spaces between aesthetasc rows. Here, knowedge of the kinematics of antennule flicking is important: during the flick downstroke, water will flow roughly vertically upward through the zig-zag, while during the return stroke, water will flow downward, with the caveat that the geometry and flow is 3D in reality. Hence, two sets of between-row gaps were recorded: $I_f$, the gap between rows within a segment of antennule, and $I_r$, the gap between rows on neighboring segments. $I_f$ is the downstream gap through which water will likely be channeled during the flick downstroke, while $I_r$ is the downstream gap through which water would likely be channeled during the return stroke. Measurements of $I_f$ and $I_r$ were also highly subjective because of the deviation of the actual hair arrangment from an idealized zig-zag. The pairs of hairs used for these calculations were therefore not always the hairs on the ends of the rows; instead, the gap that appeared most likely to limit flow through each V-formation was used.

Lastly, the angles between each row of aesthetascs ($A$) were calculated by fitting a line to the center coordinates of each aesthetasc in a row, and analytically computing the angle between each pair of lines. Lines were fit by calcuating horizontal (not vertical) distances between center coordinates and the line.

As discussed in Chapters 2 and 3, the gap to diameter ratio $G/D$ is an important dimensionless parameter that governs the nature of flow through and around aesthetasc arrays. To calculate an average gap to diameter ratio ($G/D$) for the within-row gaps, the average diameter $D$ and average gap size $G$ were used. The variability (i.e., standard deviation) of $G/D$ for all measured $D$ and $G$ was estimated by assuming that $D$ and $G$ are uncorrelated and propagating the variability in each (Bevington and Robinson 2003). We tested this assumption by pairing gaps with diameters first by pairing with the gap on the left side of each hair, and then by pairing with the gap on the right side of each hair, for those hairs

not on the ends of a row. Correlation coefficients obtained this way were 0.04 and 0.05, respectively, for data taken 315 $\mu$m above the antennule and 0.01 and -0.04, respectively, for the data 660 $\mu$m above the antennule. Hence, gap and diameter do not appear to be correlated across a single antennule. We found the same to be true for the gaps between rows, and thus computed means and standard deviations for the ratios $I_f/D$ and $I_r/D$ in the same way as for $G/D$.

### 4.4.3. Results

There is considerable variation in the zig-zag pattern of our scanned specimen, both at different heights above the antennule and along the antennule at the same height (Figure 4.9). It has been previously reported that the aesthetascs are nearly parallel at the base, and form a zig-zag pattern at the tips (Gleeson et al. 1993, Goldman and Koehl 2001). While a zig-zag pattern is clearly identifiable in our slices taken at the midway height (Figure 4.9 A1-A5), it deteriorates as height increases and is often barely recognizable at the tips (Figure 4.9 B1-B5). Whether this is an artifact of our particular specimen is unknown; our antennule was indeed missing a few guard hairs in the most proximal section we scanned (Figure 4.9 A1, top). However, the general lack of a clearly defined zig-zag pattern near the aesthetasc tips all along the scanned portion of our antennule (except perhaps Figure 4.9 B2) suggests that physical damage is not to blame.

Figure 4.10 shows an example of aesthetasc segmentation and subsequent measurements for one section of the antennule, at the midway height above the base. Although the angle $A$ between rows was calculated separately for rows in the same segment versus rows in neigboring segments, no significant difference was found between these, so all angle measurements were pooled.

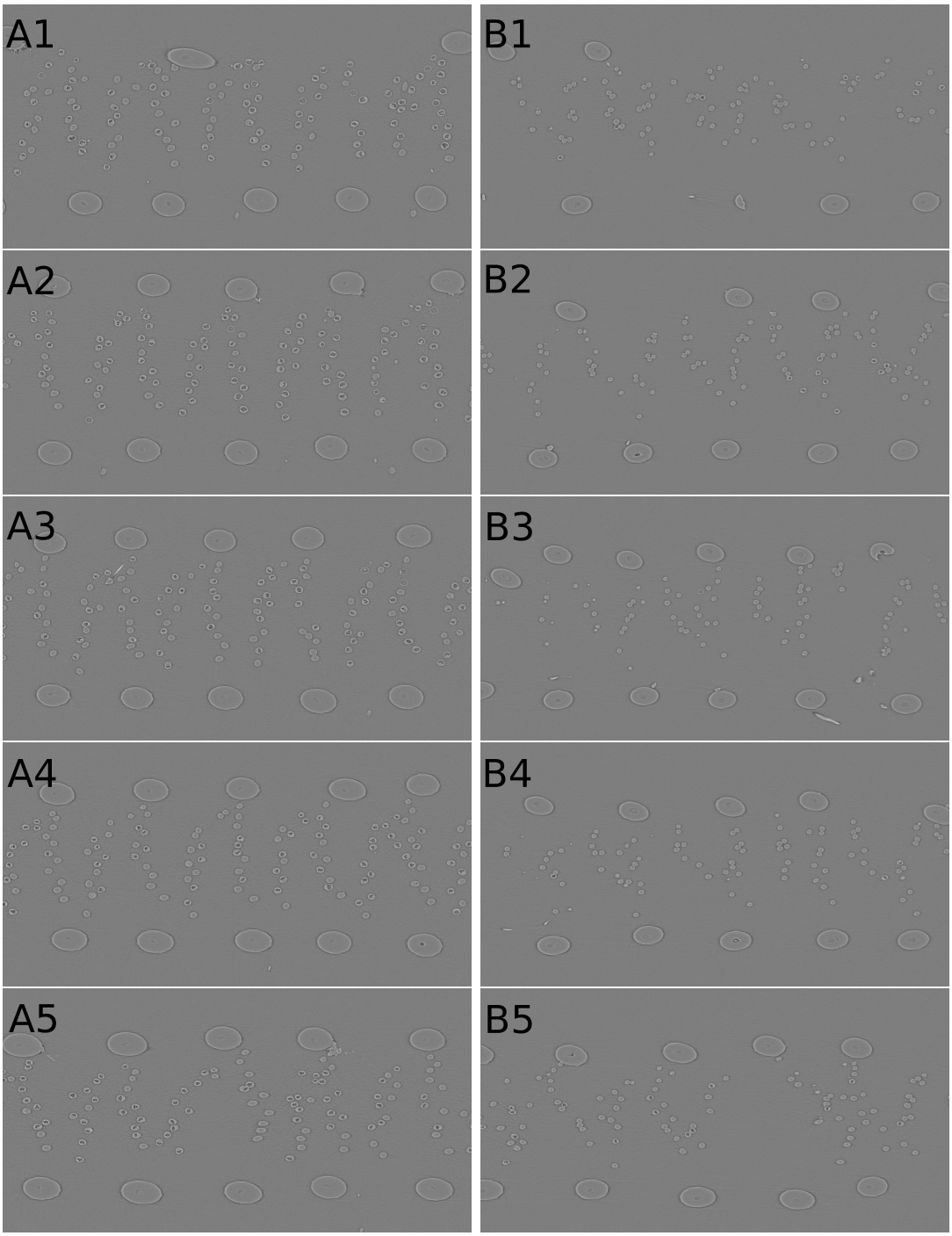


**Figure 4.9:** Cross sectional slices taken parallel to antennule and cutting through aesthetasc array, at approximately 315 $\mu$m above antennule surface (A1-A5) and 660 $\mu$m above surface, near hair tips (B1-B5). Top images are most proximal and bottom images are most distal along the antennule's main axis (there are discrepancies in continuity between images along the antennule due to small translational and rotational offsets in the 5 tiles of volume data.)

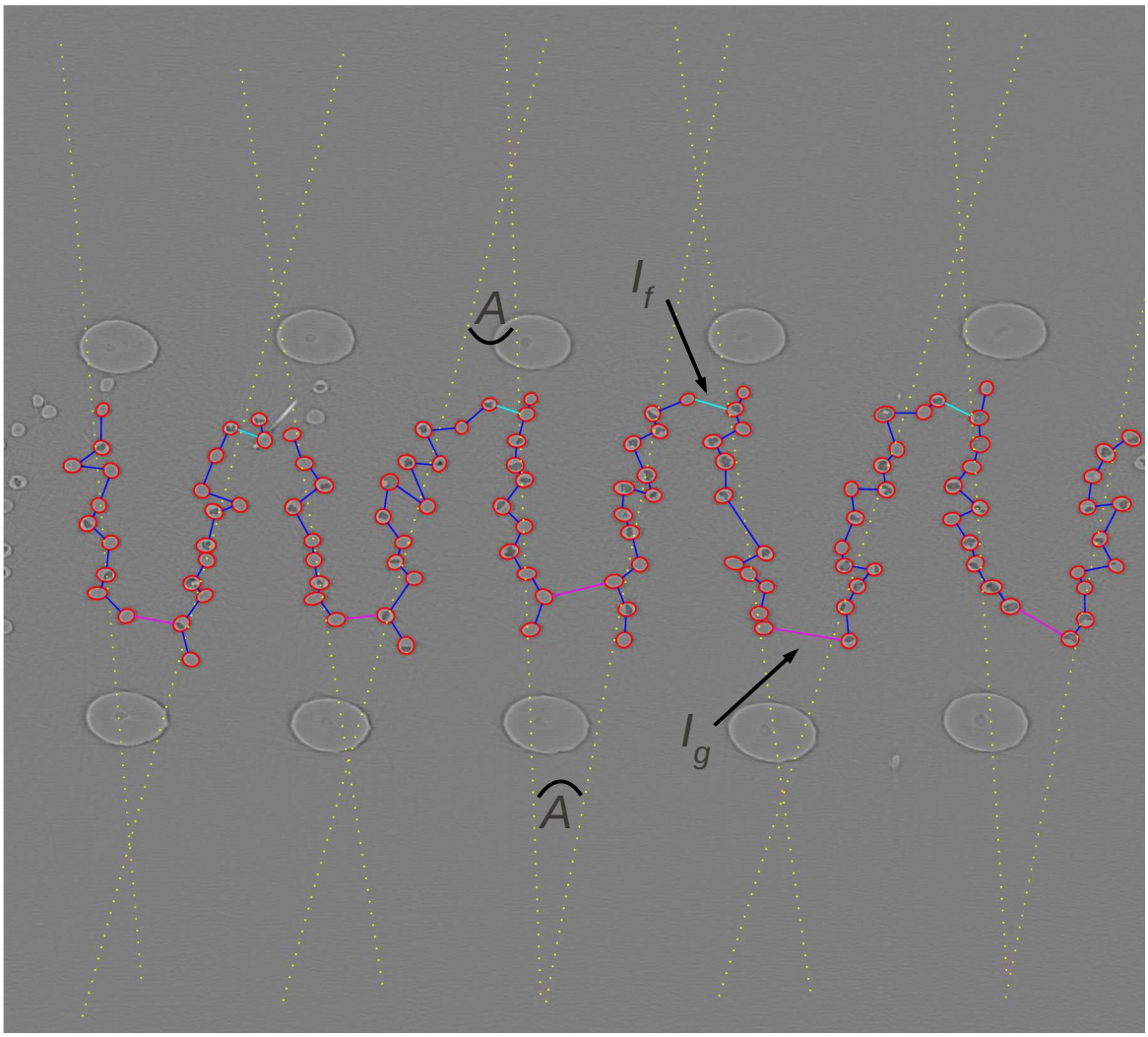


**Figure 4.10:** Example of measurements taken for slice A3 in Figure 4.9 (315 $\mu$m above antennule). Aesthetascs are outlined in red, gaps within each row are in blue, gaps between rows within the same segment ($I_f$) are in magenta, gaps between rows between segments ($I_r$) are in cyan, and linear fits to the centers of the hairs in each row are in yellow (used to calculate angles between rows, $A$).

Morphological measurements are summarized in Table 4.1, as well as previously measured values by Goldman and Koehl (2001). There is generally good agreement in the mean values of measurements found in both studies, particularly between our values at 660 $\mu$m and Goldman and Koehl's, also taken at the tips. One odd exception is $I_f$, for which there

is good agreement between our measurements at the *base* and Goldman and Koehl's at the *tips*. The variation in some array parameters with height is clear from our two sets of measurements: $I_f$ increases with height, $I_r$ decreases, and the angle forming the zig-zag pattern increases as expected. Other parameters ($D$, $G$, and $N$) change little with height. Standard deviations of most quantities are larger near the tips, which is not surprising considering the deterioration of the zig-zag pattern there (Figure 4.9 B1-B5).

The large number of measurements of $D$ and $G$ allows us to construct meaningful histograms of these quantities. Aesthetasc diameter at a midway height above the base (Figure 4.11 A1) is very well described by a normal distribution, as is gap distance (A2) to a lesser degree due to some rightward skewness. Near the tips of the hairs, diameter can still be described by a normal distribution without egregious error (B1), but there is some skewness due to many small diameter values. This is most likely a consquence of the variation in aesthetasc length and insertion angle, making it impossible to slice the volume data at the same location along every aesthetasc. In contrast to these nearly Gaussian distributions, gap spacing between aesthetascs near the tips (B2) is decidedly not Gaussian, with a very large number of hairs touching and having a gap distance of zero.

**Table 4.1:** Morphological measurements of the aesthetasc array of a *P. argus* antenule. Mean, standard deviation (SD), and number of samples (n) for two vertical locations within the array. Values from (Goldman and Koehl 2001) are also listed if available.

| symbol | feature | 315 $\mu$m above base | | | 660 $\mu$m above base | | | Goldman and Koehl | | |
|---|---|---|---|---|---|---|---|---|---|---|
| | | mean | SD | n | mean | SD | n | mean | SD | n |
| $D$ | aesthetasc diameter ($\mu$m) | 22 | 2.0 | 582 | 16 | 2.3 | 312 | 22 | 3 | 42 |
| $G$ | gaps within a row of aesthetascs ($\mu$m) | 24 | 13 | 541 | 24 | 21 | 278 | - | - | - |
| $I_f$ | gap between aesthetasc rows within a segment ($\mu$m) | 50 | 19 | 22 | 87 | 29 | 14 | 53 | 10 | 18 |
| $I_r$ | gap between aesthetasc rows between segments ($\mu$m) | 85 | 27 | 22 | 59 | 23 | 14 | - | - | - |
| $A$ | angle between aesthetasc rows (degrees)* | 21 | 6.3 | 44 | 37 | 12 | 27 | 39 | 8 | 36 |
| $N$ | number of aesthetascs per row | 12 | 1.3 | 46 | 9.3 | 1.9 | 33 | 10 | 1 | 42 |

* No significant differences were found between the average angle formed by aesthetasc rows within a segment versus between segments (two sample t-test at a significance level of 0.05) for both locations above the base, hence the results reported at each location are pooled.

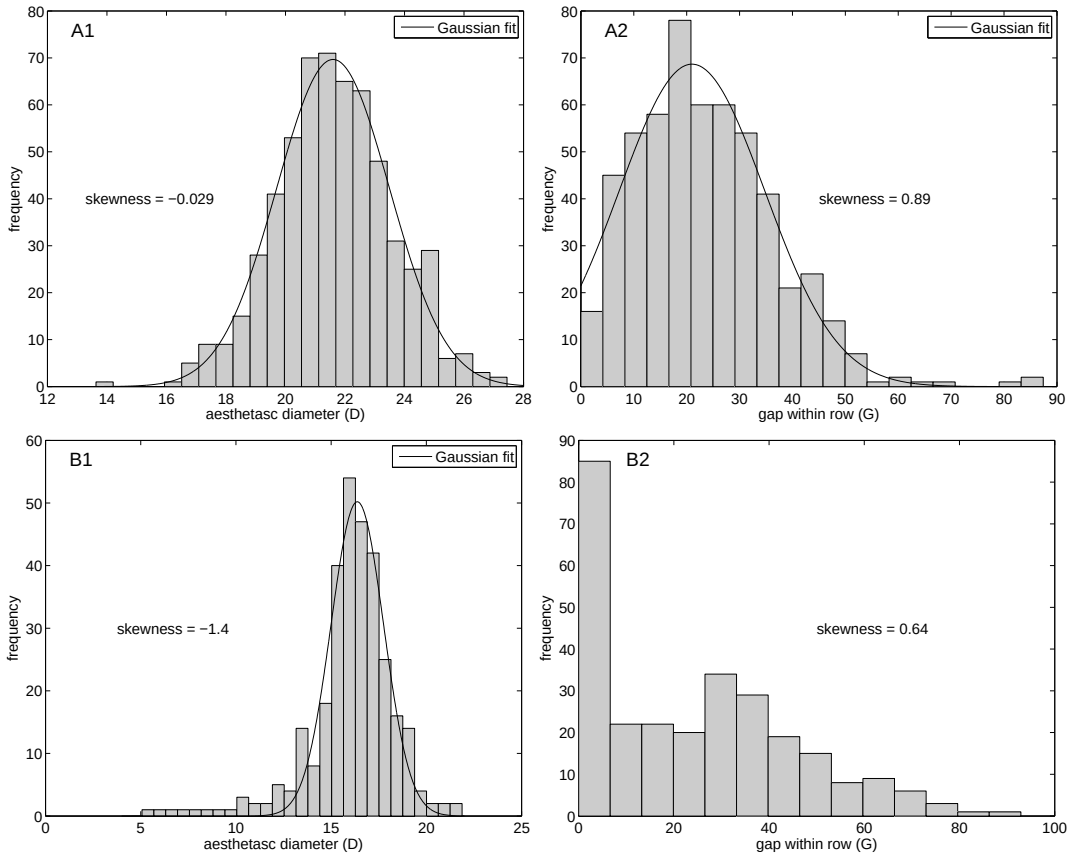


**Figure 4.11:** Histograms of measured aesthetasc diameter (1) and within-row gaps (2), taken 315 $\mu$m above the base (A) and 660 $\mu$m above the base (B). Bin sizes calculated according to the Freedman-Diaconis rule. Skewness of each data set is shown, as well as a Gaussian fit of zero skewness for all but (B2).

Gap to diameter ratios derived from the morphological measurements are listed in Table 4.2. $G/D$ for aesthetascs within each row is small, about 1 - 1.5, while gap to diameter ratios between rows are higher. Again, there is generally much more variation in geometry near the tips than at the midway height due to the breakdown of a coherent zig-zag pattern near the tips.

### 4.4.4. Discussion

Gleeson et al (1993) hypothesized that the zig-zag pattern of aesthetascs in *P. argus* acts to channel water and odorant through the dense array of hairs. The larger gap to diameter

**Table 4.2:** Statistics of derived values calculated from data in Table 4.1.

| symbol | feature | 315 $\mu$m above base | | 660 $\mu$m above base | |
|---|---|---|---|---|---|
| | | mean | SD | mean | SD |
| $G/D$ | gap to diameter ratio (gaps within a row) | 1.1 | 0.62 | 1.5 | 1.3 |
| $I_f/D$ | gap to diameter ratio (gaps between rows within a segment) | 2.3 | 0.91 | 5.4 | 2.0 |
| $I_r/D$ | gap to diameter ratio (gaps between rows between segments) | 3.9 | 1.3 | 3.7 | 1.6 |

* $D$, $G$, $I_f$, and $I_r$ were assumed to be uncorrelated in the calculation of standard deviation for these derived values; see text.

ratios ($I_f$ and $I_r$) at the vertices of the zig-zag pattern (between rows) versus $G/D$ within each row (Table 4.2) seem consistent with this idea. The much smaller gaps between hairs within a row, about the same as an aesthetasc diameter, mean that flow and odorant transport through a row is likely to be drastically inhibited compared to the gaps between rows (see Chapter 3). This will tend to make a V-formation behave hydrodynamically as two solid plates, effectively channeling flow, but also possibly reducing odorant flux to the hairs due to decreased surface area available for molecule capture. This issue is explored quantitatively in Section 4.5.

The variation in aesthetasc array geometry with height (i.e., its three dimensionality) may have important consequences on the flow flow and odorant transport during antennule flicking. Since the downstream gap of each V-formation during the flick downstroke ($I_f$) is larger near the hair tips than lower down (Table 4.1), there is likely to be more flow near the tips. This is especially likely because of the boundary layer due to the antennule itself, which may in fact dominate any effect of hair spacing. Indeed, Reidenbach et al (2008) found fluid velocity to increase quite sharply at a height above the antennule about 3/4 of the way to the aesthetasc tips. This suggests most odorant flux would occur near the tips of the aesthetascs. However, the spacing between hairs along each row ($G$) may also be important. Although the average value of these gaps is the same near the base and at the tips (Table 4.1), a large number of hairs are touching and clustered together near the tips (Figure 4.11 B2). This clustering may act to decrease the effective surface area available for odorant detection near the tips, confounding the hypothesis that most odorant detection occurs there. Furthermore, the cuticle of *P. argus* aesthetascs is in fact permeable to odorant molecules and contains odorant receptors along most of the hair's length (Blaustein et al. 1993), begging the question of why this might be the case if odorant never penetrates down into the array. Simulations of odorant transport using more realistic 3D geometry may be necessary to resolve this question.

Although there is no significant difference in the medial versus lateral angles of the zig-zag pattern, the differences in $I_r$ and $I_f$ (Table 4.1) are significant ($\alpha = 0.05$). Near the base of the hairs, $I_r$ is larger than $I_f$, while the opposite is true near the tips. Thus, the flow that occurs during the flick versus return movements of the antennule is not only asymmetric due to the speed of the movement, but also the geometry of the aesthetasc array. Near the base of the hairs, larger downstream gaps between rows during the return stroke ($I_r$) might act to somewhat mitigate the decreased flow through the V-formations during this slower motion, but the effect of the slower speed probably dominates the effect of the slightly larger gaps. Both the idealized numerical simulations of Chapter 3, and the experiments of Reidenbach et al (2008) using a physical model of a *P. argus* antennule, support this reasoning. The slow return stroke is therefore thought to allow sufficient time for trapped odorant in the V-formations (sampled during the fast downstroke) to diffuse to aesthetasc surfaces (Koehl 2006). The fact that gaps between rows on neighboring antennule segments are larger than gaps between rows on the same segment might simply be a consequence of the segmented nature of crustacean antennules.

## 4.5. Numerical simulations

### 4.5.1. Overview

The ventrolateral orientation and zig-zag pattern of hairs on the antennules of *P. argus* have been thought to channel odor-laden water into the dense aesthetasc array. We wished to test this theory by quantifying leakiness and odorant molecule capture of single V-formations of hairs. Since the gaps between rows of hairs are larger than the gaps within each row in *P. argus*, both "closed" and "open" V-formations were tested to test the significance of this, as well as two different angles between the rows, corresponding to zig-zag geometry near the bases versus the tips of the hairs. As a baseline for comparison, we use a straight row of the same number of hairs as the V-formations, identical to the geometry studied in detail in Chapter 3. We can therefore quantify whether the V-formations of aesthetascs making up the zig-zag pattern of *P. argus* do in fact achieve higher odorant sampling performance than a much simpler row of hairs in cross flow. Nearly straight rows of aesthetascs do occur in some species such as the stomatopod *Gonodactylaceus falcatus*, though this species has multiple rows of hairs, one behind the other in the streamwise direction, and its hairs are much farther apart than is the case in *P. argus* (Mead and Koehl 2000).

## 4.5.2. Methods

The flow of water around and transport of odorant molecules to four different 2D array geometries (Figure 4.12) at two different sampling speeds ($Re$ = 2 [$U_0$ = 7.49 cm/s] and $Re$ = 0.5 [1.87 cm/s]), corresponding to a flick downstroke and return stroke by *P. argus*) during a plume sampling event was numerically modeled according to the methods detailed in Chapter 3. Briefly, COMSOL Multiphysics was used to solve the incompressible Navier Stokes equations for steady fluid flow and the advection-diffusion equation for unsteady scalar transport, using the finite element method (FEM). Generation of the computational mesh was very similar to the method described in Chapter 3, except a triangular instead of rectangular region of very high mesh resolution enclosed the half of the symmetric array that was explicitly modeled (Figure 4.13). Once the steady flow field around each geometry was solved for, an idealized odorant filament, Gaussian in the streamwise direction and long enough to span the cross-stream width of the array, was initialized upstream of the array and allowed to advect toward it. A boundary condition of zero odorant concentration was imposed on each hair, which caused a time-varying inward flux of odorant mass that was recorded for each simulation.

All four array types (Figure 4.12) are composed of 25 $\mu$m diameter cylinders, which is similar to the size of *P. argus* aesthetascs (Table 4.1) and the same as the arrays studied in Chapters 2 and 3. The gaps between hairs within the rows are also 25 $\mu$m, yielding $G/D$ = 1, as is the case in *P. argus* (Tables 4.1 and 4.2). Geometry A does not have any gap between the two rows of the V-formation, while arrays B and C have a 60 $\mu$m gap space between the most downstream cylinders. This corresponds to a gap to diameter ratio ($I/D$) = 2.4 for the space between rows, which matches the data of Goldman and Koehl (2001) and our measured $I_f/D$ at 315 $\mu$m above the base, for the downstream gap during the flick downstroke. The angle of the V-formation is 39° in arrays A and B, and 20° in array C; these values correspond to the angles found midway up and at the tips of the hairs, respectively (Table 4.1). An array with the smaller 20° angle and no downstream gap could not be tested because it is physically impossible: two of the hairs near the vertex would overlap. Geometry D is a simple straight row of cylinders designed to test the possible advantages or disadvantages of the V-shaped geometries. While arrays A and D have 19 hairs, B and C have 20 hairs; however, the difference of one hair is unlikely to have a large impact on the aggregate sampling performance of each array.

To succinctly describe the fluid flow through each array, the volumetric flow rate and leakiness for a number of control surfaces were calculated. These control surfaces are shown in Figure 4.12: the gaps between each hair along a row (i.e., the sides of the V-formations in A, B, and C or the single row of D), as well as the inlet (in A, B, C) and outlet (in B, C) gaps between rows. Flow rate was computed by integrating the normal component

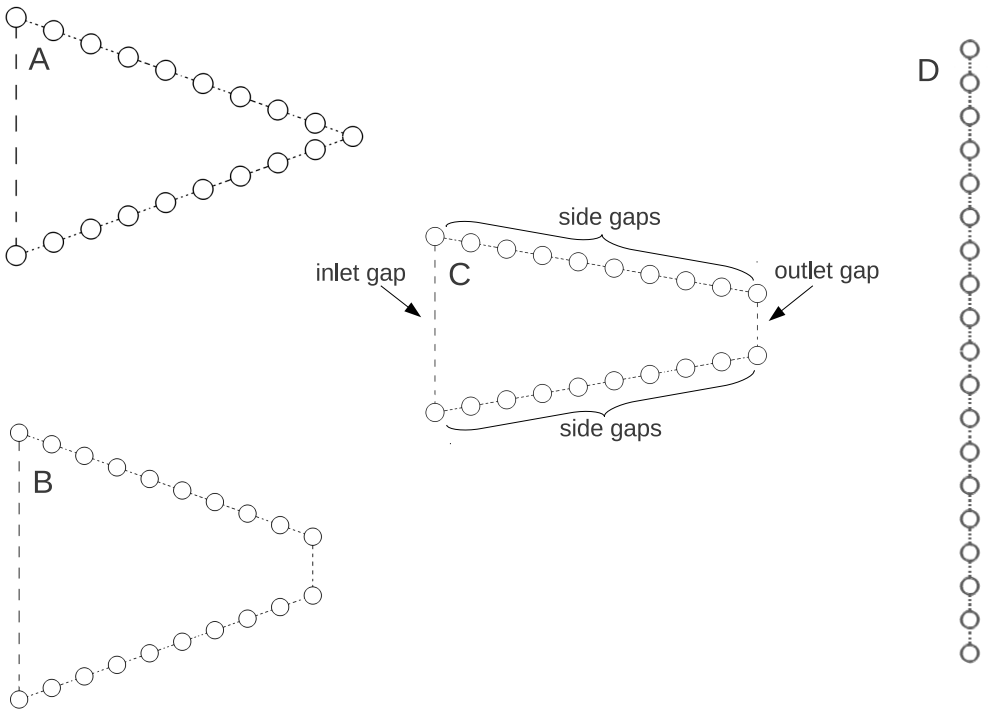


**Figure 4.12:** Tested geometries. Flow is from left to right in all cases. Dashed/dotted lines across gaps indicate control surfaces, labeled in (C), over which the normal component of velocity was integrated to calculate flow rate and leakiness, and do not represent real surfaces. (A) Closed V-formation of 19 cylinders with a 39° angle between rows. (B) Open V-formation of 20 cylinders with a 39° angle between rows. (C) Open V-formation of 20 cylinders with a 20° angle between rows. (D) Straight row of 19 cylinders. All cylinder diameters and gaps are 25 $\mu$m, except the vertical outlet gap of open formations (B) and (C), which is 60 $\mu$m.

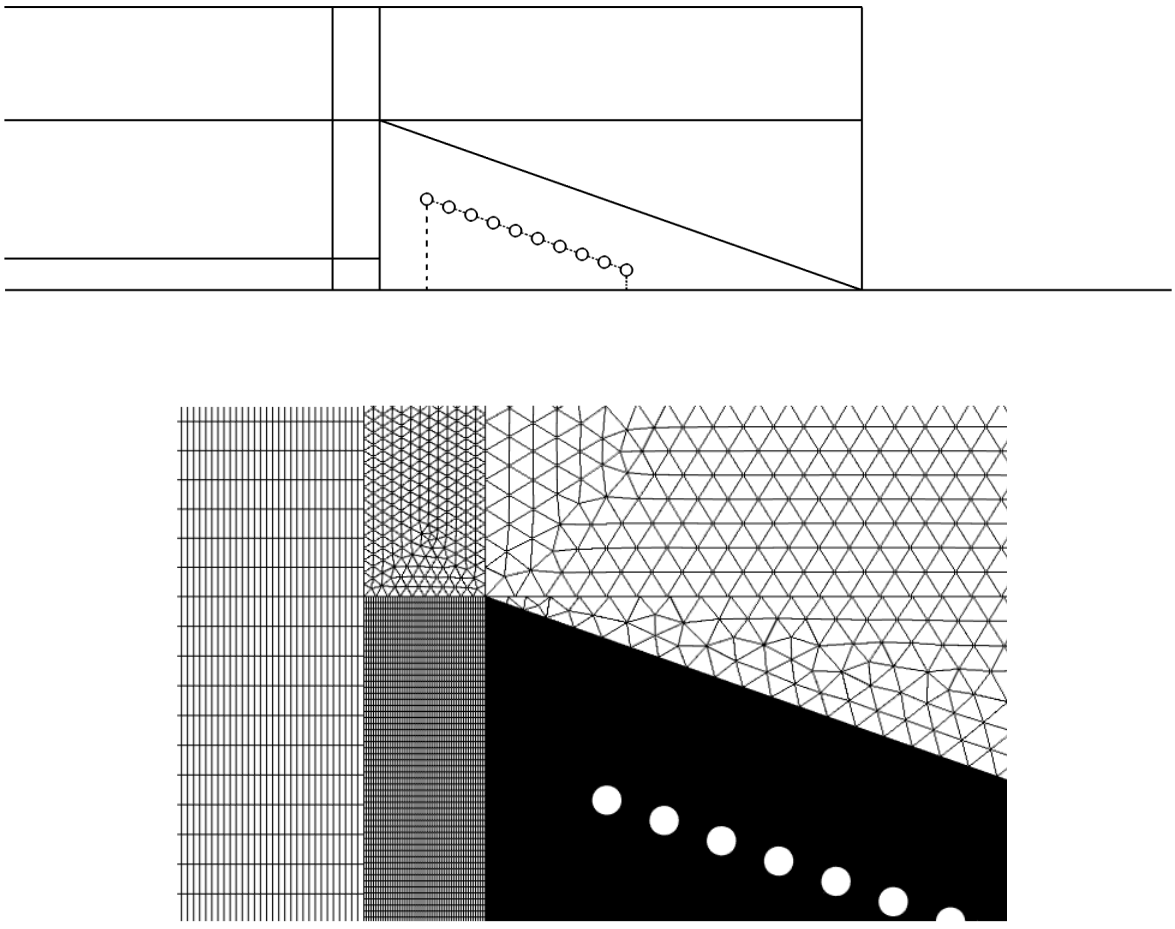

**Figure 4.13:** Top: sketch of mesh regions close to array. Bottom: computational mesh in near-field. Highest refinement is in triangular area surrounding the cylinders (appears black due to high element density). Setup is otherwise identical to that used in the simulations reported in Chapter 3.

of velocity along each control surface, and leakiness was computed (as in Chapter 3) by dividing this actual flow rate by the flow rate that would hypothetically occur if the normal component of the freestream velocity were integrated over the same control surface. Flow rate is included here in addition to leakiness because leakiness may not be very meaningful when applied to control surfaces at an angle to the freestream flow (along the side gaps in V-formations). Flow rates and leakiness values were aggregated over the side gaps along the rows of A, B, and C - we do not address patterns in intra-array variability in flow.

As in Chapters 2 and 3, the time-varying odorant flux into the arrays is quantified by several parameters that may be neurobiologically important. These are summarized below for a flux time series $f(t)$; for a detailed description of each parameter's relevance and calculation, see Chapter 3. As with leakiness of the side gaps, these parameters are calculated in the aggregate sense, using the summed time series of flux into all hairs of each array.

| | |
|---|---|
| peak flux | maximum value of $f(t)$ |
| peak onset slope (or peak slope) | maximum value of $\frac{d}{dt}(f(t))$ |
| time-integrated flux (or total flux) | $\int_0^\infty f(t)dt$ |
| flux duration | minimum value of $t_2 - t_1$ such that $\int_{t_1}^{t_2} f(t)dt = 0.95$(total flux) |

### 4.5.3. Results

Instantaneous snapshots of the odorant concentration field during a sampling event at *Re* = 2 (a flick downstroke by *P. argus*) by each geometry are shown in Figure 4.14. The sampling behavior of all three V-formations (A, B, C) superficially appears quite similar, but with some odorant mass escaping through the outlet gaps between the two rows of B and C. The hair at the vertex of array A, which lacks an outlet gap, is blocked by two upstream hairs and experiences very little odorant flux, as evidenced later in Figure 4.15. While the hairs along the straight row (D) experience odorant flux at roughly the same time, the hairs along the V-formations are exposed to odorant in a staggered fashion due to their stream-wise separation. As discussed in Section 4.5.4, this has important implications for how V-formations, versus straight rows in crossflow, might integrate sensory information from each hair in the array.

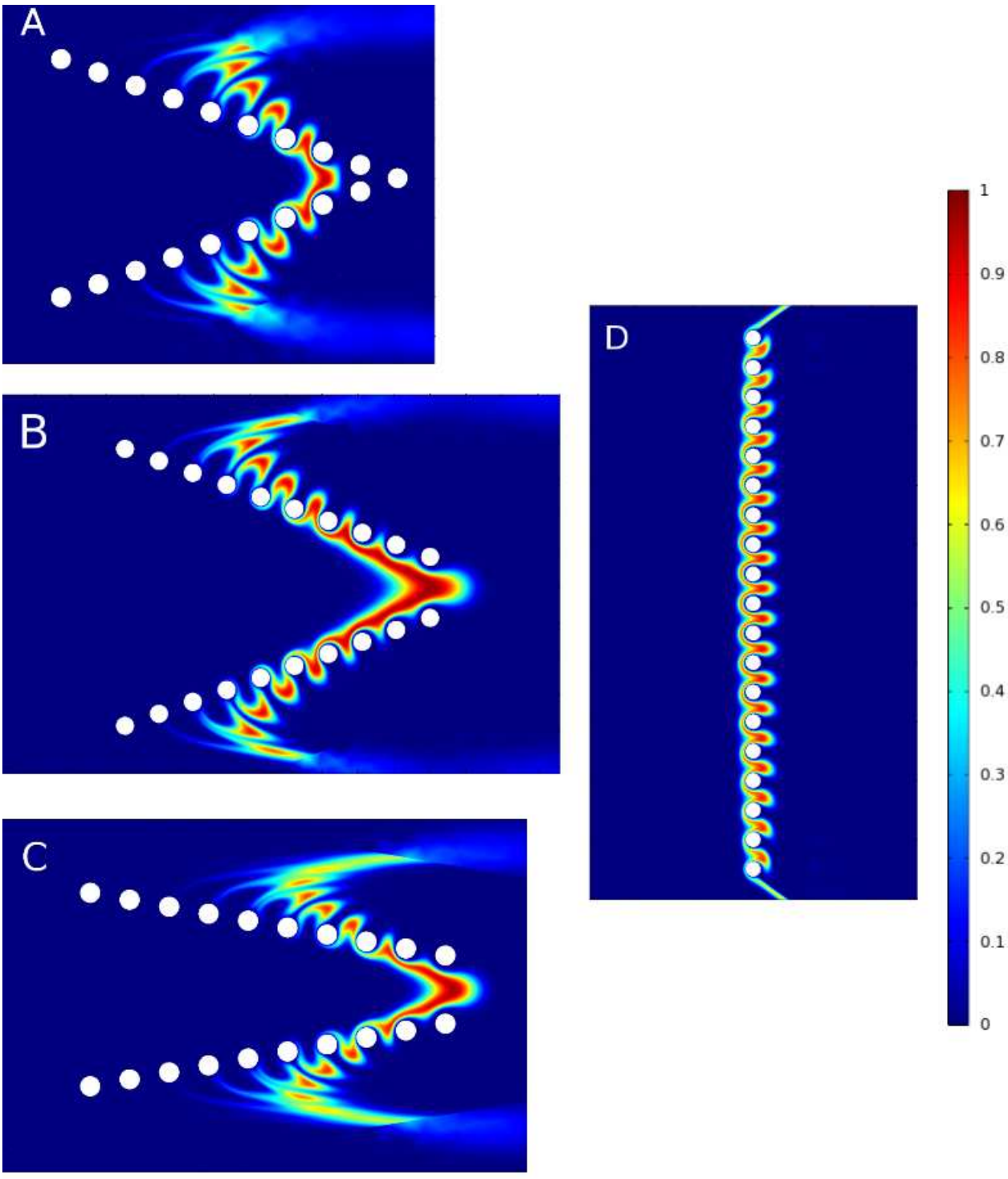


**Figure 4.14:** Odorant concentration field snapshots during a sampling event of the same Gaussian odorant filament by each geometry. Colorbar indicates concentration (mg/L) for all cases.

### Flow and leakiness

Table 4.3 summarizes the flow rates and leakiness values for the inlet, side, and outlet (when present) gaps of the V-formations (A, B, C), as well as for the simple straight row of hairs (D). Note that flow rates through the inlet gap and side gaps of array A are necessarily the same due to mass conservation.

At both high and low $Re$, array B (larger angle, with downstream gap) has the highest flow through the inlet gap, which is also higher than the total flow through the gaps of the straight row. However, leakiness of the inlet gap is highest for array C (smaller angle, with downstream gap), indicating that average fluid velocity entering array C is highest even though its inlet gap is smaller than array B. Overall leakiness of the straight row is smaller than leakiness of the inlet space of any of the V-formations, indicating a low permeability to water relative to its cross stream width.

Although flow rate and leakiness for the inlet gap of a V-formation may predict how much odorant will enter the volume between rows, examining flow through the gaps betwen hairs along each row may more accurately reflect sampling performance since odor molecules must contact a hair in order to be detected. This is especially true for cases B and C, for which much odorant might escape through the outlet gap. Array B experiences the highest total flow through the side gaps, though a straight row matches it at the slower sampling speed of the return stroke. As with the inlet gap, leakiness along the sides of the V-formation is again highest for case C. However, since leakiness of the side gaps appears to increase as the angle between rows decreases (between cases B and C), an absolute quantity such as flow rate (which intuitively decreases from B to C) may be more appropriate here than leakiness.

Having a downstream outlet gap between rows indeed improves the flow rate and leakiness between hairs of the V-formation (A vs B). Array B also achieves higher flow rates and leakiness than a straight row (D). Hence, a V-formation with a downstream opening does seem to funnel water at the relatively low $Re$ at which olfactory appendages operate, and the effect is stronger for a larger angle forming the V (B vs C). However, because odorant-laden fluid can exit the V-formation through an outlet gap, bypassing detection, whether better odorant sampling performance is achieved by a V-formation is best answered by directly examining odorant flux into the hairs.

**Table 4.3:** Flow rates and leakiness values for different gaps in each geometry, at high $Re$ and low $Re$ conditions. "Inlet gap" refers to the upstream opening between rows of a V-formation, "outlet gap" refers to the downstream opening, and "all side gaps" refers to quantities evaluated over all the gaps within both rows forming the V, as labeled in Figure 4.12. Case A does not contain a downstream gap between rows, and Case D refers to a single row in crossflow, whose aggregate flow rate and leakiness values are also listed as "side" values for comparison despite the different geometry. All flow rates are in $mm^3$ / s.

| | Flick Downstroke ($Re = 2$) | | | | | |
|---|---|---|---|---|---|---|
| geometry | Inlet Gap | | All Side Gaps | | Outlet Gap | |
| | flow rate | leakiness | flow rate | leakiness | flow rate | leakiness |
| A | 3.3 | 0.16 | 3.3 | 0.29 | - | - |
| B | 4.8 | 0.23 | 3.8 | 0.35 | 0.97 | 0.22 |
| C | 3.5 | 0.36 | 3.0 | 0.53 | 0.55 | 0.12 |
| D | - | - | 3.5 | 0.10 | - | - |
| | Return Stroke ($Re = 0.5$) | | | | | |
| geometry | Inlet Gap | | All Side Gaps | | Outlet Gap | |
| | flow rate | leakiness | flow rate | leakiness | flow rate | leakiness |
| A | 0.27 | 0.053 | 0.27 | 0.098 | - | - |
| B | 0.40 | 0.077 | 0.32 | 0.11 | 0.081 | 0.072 |
| C | 0.30 | 0.12 | 0.24 | 0.17 | 0.055 | 0.049 |
| D | - | - | 0.32 | 0.037 | - | - |

### Odorant flux

Time series of odorant flux into each individual hair of each array are shown in Figure 4.15 for $Re = 2$ and $Re = 1$. Though all the time series exhibit similar qualitative features, the most obvious feature of the V-formations is how much more spread out in time the fluxes into each hair are than for a straight row geometry. Although a monotonic trend in when each hair's peak flux occurs is seen in the V-formations just as in the straight row arrays, the fact that the hairs of a V-formation are spread out in the streamwise direction causes odorant fluxes to be spaced apart temporally. As is the case with a straight row of hairs, the outermost (or most upstream) hairs experience the highest peak flux by a large margin, and there is usually the same monotonic decrease in peak flux toward the center (or most downstream) hairs. One exception to this trend occurs for array B, where there is a small jump in peak flux to the most downstream hairs.

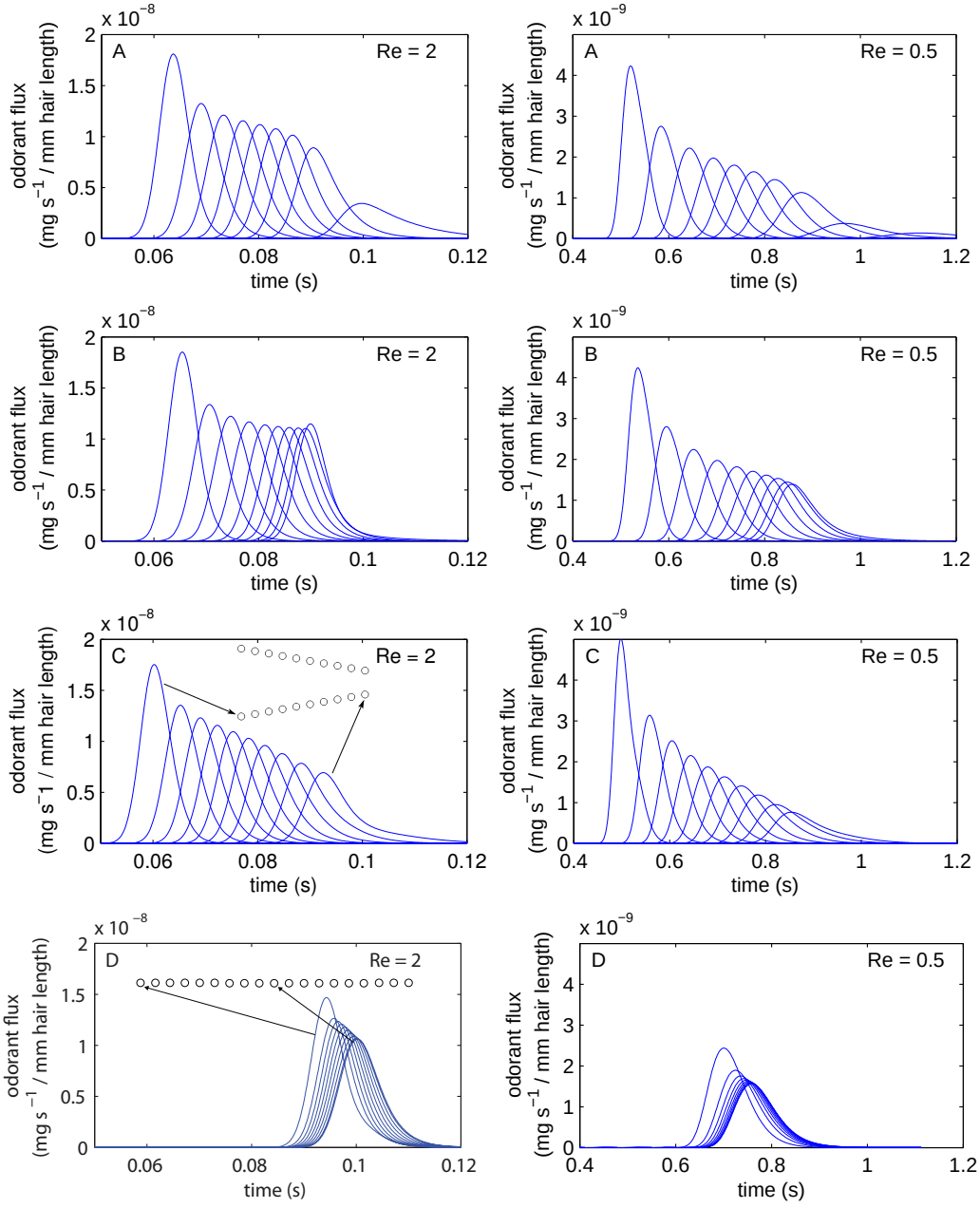


**Figure 4.15:** Odorant flux time series into each hair of array geometries A - D at $Re = 2$ and $Re = 0.5$. Since each array is symmetric, only fluxes to half the hairs (one side of each array) are shown. The first curve always corresponds to the most upstream (A, B, C) or outermost (D) hair, while the last curve always corresponds to the most downstream (A, B, C) or innermost hair (D), labeled for array (C), $Re = 2$. Curves in between correspond to the hairs in between in a straightforward fashion. Flux to the most downstream of hair of A at $Re = 2$ is very small and not visible in the plot.

**Table 4.4:** Aggregate flux metrics for each geometry at $Re = 2$ and $Re = 1$.

| | Flick Downstroke ($Re = 2$) | | | |
|---|---|---|---|---|
| geometry | peak flux (mg / s · mm) | peak slope (mg / $s^2$ · mm) | total flux (mg / mm) | flux duration (ms) |
| A | 5.9E-8 | 9.0E-6 | 1.8E-9 | 43 |
| B | 9.9E-8 | 9.3E-6 | 2.0E-9 | 33 |
| C | 6.0E-8 | 9.0E-6 | 1.9E-9 | 40 |
| D | 2.0E-7 | 3.4E-5 | 2.0E-9 | 17 |
| | Return Stroke ($Re = 0.5$) | | | |
| geometry | peak flux (mg / s · mm) | peak slope (mg / $s^2$ · mm) | total flux (mg / mm) | flux duration (ms) |
| A | 8.5E-9 | 3.3E-7 | 3.0E-9 | 470 |
| B | 1.3E-8 | 3.1E-7 | 3.6E-9 | 400 |
| C | 1.0E-8 | 4.3E-7 | 3.2E-9 | 420 |
| D | 3.0E-8 | 4.7E-7 | 3.5E-9 | 190 |

Figure 4.16 shows the aggregate flux time series for each array, in which the flux into every hair of the array has been summed, for $Re = 2$ and $Re = 0.5$. While the aggregate curve for the straight row (D) is nearly Gaussian at both sampling speeds (as was the case for all straight rows studied in Chapter 3), the V-formations display very different behavior due to the larger temporal separation between fluxes to each hair. Several cases exhibit two peaks, and the the peaks are generally broader, flatter, and not as high as those of the straight row. Flux during the slower return stroke is about 10 times lower than during the flick downstroke for each geometry. However, we must note the caveat that we only tested one outlet gap size, the one of most relevance to the downstroke, so our V-formation geometries are more appropriate for modeling the downstroke than the return stroke of *P. argus*.

The flux metrics that summarize the aggregate flux time series to each array are listed in Table 4.4. Interestingly, the straight row of hairs (D) achieves the highest peak flux, peak slope, and total flux at the $Re$ of the flick downstroke, though all the arrays achieve similar total flux. A straight row also experiences the shortest duration of odorant flux, due to its thin cross-stream extent compared to a V-formation. The same is true at the return stroke sampling speed, except array B achieves a slightly higher total flux than the straight row.

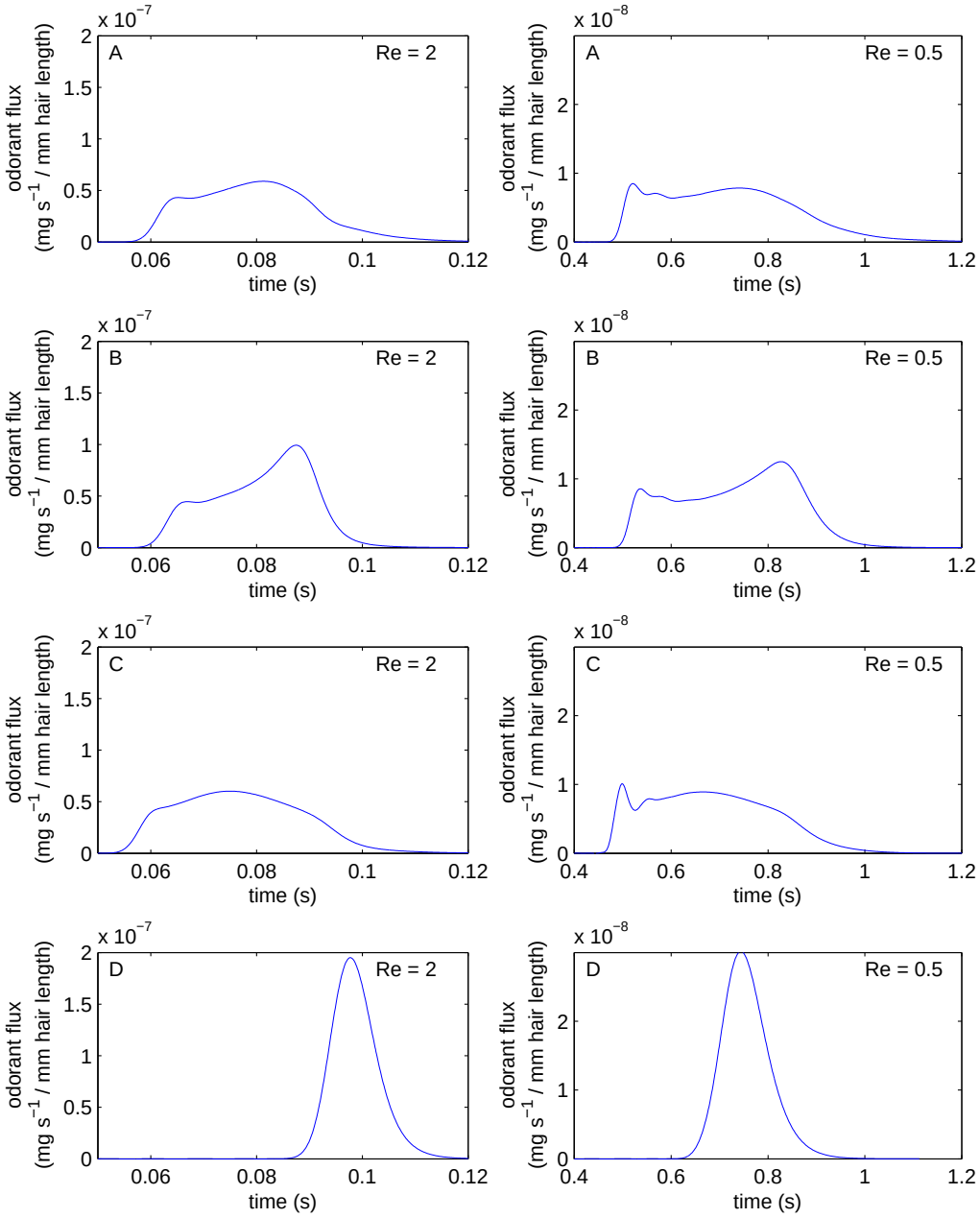


**Figure 4.16:** Aggregate odorant flux time series, summed over all hairs in the array, for geometries A-D at $Re = 2$ and $Re = 1$.

### 4.5.4. Discussion

Although a V-formation of aesthetascs does appear to effectively funnel odorant-laden water into the volume enclosed by the V, it does not appear to be more effective than a simple straight row in cross-flow at capturing odorant molecules during a plume sampling event. A straight row achieves similar or higher peak flux, peak slope, and total flux. This result might be due to the fact that odorant funneled into a V-formation is not guarenteed to be detected, especially when a downstream outlet gap between rows is present. In addition to odorant leaking out of the outlet gap, any plume structures that do penetrate into the volume contained by a V-formation may undergo more shear strain before reaching the hair surfaces than in the case of a straight row, which would act to decrease concentration gradients and generally decrease flux. However, the V-formations do experience an odorant flux for a longer time than a straight row. Although the flux durations at the downstroke $Re$ are still very short compared to known neural integration timescales ($\sim 100$ ms for the clawed lobster *Homarus americanus* (Gomez and Atema 1996a)), flux durations at the return stroke $Re$ are much higher and likely to lead to detection by the nervous system. The zig-zag pattern of aesthetascs in *P. argus* might therefore be an adaptation to retain odorant near the aesthetascs as long as possible. Interestingly, the mantis shrimp *G. falcatus* has multiple rows of aesthetascs in the stream-wise direction (Mead and Koehl 2000). This might be a similar adaptation that increases the duration of odorant flux and makes detection of very thin plume structures more likely.

While the flux time series to individual hairs of the V-formations are very similar in shape to that of the original Gaussian odorant filament, the shape of the aggregate flux time series are quite different. The signal distortion that V-formations introduce, but that straight rows in cross flow do not, may be due to the V-formations having a high "sampling fraction" (see Chapter 2) in an aggregate sense compared to straight rows. While a straight row is very thin (a hair diameter) in the stream-wise direction, a V-formation spans a much longer distance. Thus, as an odorant filament advects past each array, at any instant in time there will probably be more array surface area in contact with the filament for a V-formation than for a straight row. In the case of the V-formation, gradients in odorant concentration in the stream-wise direction will become averaged out by the array as a whole when transduced to a temporal flux signal. This high level of filament shape distortion means that it would be less likely for the nervous system of an animal to reconstruct the spatial structure of the original plume from an aggregated signal, versus from signals from each individual aesthetasc. Although the level of neural convergence in crustaceans such as *P. argus* is largely unknown, it is unlikely that signals from each aesthetasc are processed individually. The degree of aggregation of chemosensory information along the antennule may therefore be an important factor in determining what fine-scale details of the plume are available to *P. argus*. This is obvious if spatial sampling (e.g., comparing signals from different aesthetascs)

is employed, but the data presented here show that this is also true if temporal sampling (e.g., inferring spatial plume structure from a time series of measurements) is used.

## 4.6. Conclusions

This chapter investigated the morphology of a real aesthetasc array, that of the spiny lobster *P. argus*, in great detail in an effort to understand how its peculiar arrangment of sensory hairs might affect odorant sampling performance. A 3D scan of an actual specimen revealed substantial variation in hair arrangement within a single antennule. Although the previously reported zig-zag pattern of aesthetascs was well defined at an intermediate height above the antennule, it deteriorated into a much more haphazard arrangment near the tips of the hairs, where the most exposure to odorant-laden water would be expected to occur. Nonetheless, measurements of the geometry show that on average, hairs are very closely spaced along each row but that larger spaces at the vertices between rows might effectively channel water through each V-formation. This hypothesis is supported by idealized numerical simulations of single V-formations of hairs. However, as the data in Chapter 3 already showed, *odorant* sampling performance is not necessarily well predicted by *fluid* sampling performance. Data presented here indicate that in many regards, a simple straight row of hairs in crossflow is better than a V-formation at capturing odorant molecules from the same odorant filament. It is possible that the zig-zag morphology of *P. argus* is then an adaptation to prolong the duration of odorant flux and mitigate the relatively long sensory integration times of crustacean olfactory neurons. Biologically inspired chemical sensor arrays that have much faster response times than olfactory neurons (a feat admittedly yet to be accomplished) may achieve higher performance with a simple row of sensors than a more exact replica of *P. argus* morphology.

## Acknowledgements

This research used resources of the National Energy Research Scientific Computing Center, which is supported by the Office of Science of the U.S. Department of Energy under Contract No. DE-AC02-05CH11231, and of the Advanced Light Source at Lawrence Berkeley National Laboratory, which is supported by the Director, Office of Science, Office of Basic Energy Sciences, of the U.S. Department of Energy under Contract No. DE-AC02-05CH11231.

# 5. Conclusions

## Summary

The work in this dissertation focuses on using computational methods to examine how arrays of chemosensory hairs, crustacean aesthetascs, interact with and sample turbulent odor plumes. Although these biological sensor arrays play an important role in the rapid plume tracking abilities of many marine crustaceans (e.g., lobsters, mantis shrimp, blue crabs), the small-scale transport of odorant molecules from the plume to individual aesthetascs is poorly understood. The transduction of spatial plume structures to time-varying odorant fluxes to aesthetascs that occurs during this process is likely to filter information contained in an organism's odor landscape. Following a research path from simpler to more complex numerical models of reality, the work presented here aims to quantify how the morphology and sampling kinematics of an aesthetasc array affect how an odorant plume is perceived by an organism.

In Chapter 2, perhaps the simplest type of array geometry possible, an infinitely wide row of 2D cylindrical hairs, was used to investigate the fundamental properties of odorant transport within the gaps between hairs of an array. High shear in the fluid flow in the gaps, caused by sampling a plume at higher speeds, increases peak odorant flux metrics but also leads to distortion of original plume structure as represented in the temporal flux signal. Sampling faster also reduces the total number of odorant molecules detected. Hence, there are performance tradeoffs that both crustaceans with chemosensory antennules and similarly equipped bio-inspired plume-tracking robots are likely to experience.

Chapter 2 also provides some evidence that crustacean antennules may be good starting points in the design of engineered sensor arrays, since arrays based on the antennules of the spiny lobster *P. argus* and mantis shrimp *G. falcatus* generate temporal flux signals of the same shape as the sampled odorant filament, with very little distortion. However, because the timescales of response of both crustacean olfactory neurons and current chemical sensors are relatively slow, measuring fine-scale plume structure does not seem feasible via analysis of temporal signals. Crustaceans may instead utilize spatial sampling to infer plume structure by comparing the signals they receive from different regions of the aesthetasc array.

Chapter 3 introduced another element of realism, leakiness, to the model of a crustacean aesthetasc array. This was done by accounting for the number of hairs in the row, which is never infinite in reality. While some features of infinite-extent arrays, such as the design tradeoff between peak and total flux and the brief duration of flux during a typical plume sampling event, are also found in finite-extent arrays, the latter exhibit some intriguing behaviors not predictable by the simpler infinite array model. Firstly, the finite width of a real array means that not all sensory hairs will experience exactly the same fluid flow and odorant transport dynamics, as is the case for infinite arrays. Differences in the sampling performance of hairs across the array may cause some odorant patches to be detected by some hairs of the array but missed by other hairs, and vice versa. This type of specialization could occur due to physical processes alone, even if all aesthetascs contained exactly the same type of olfactory neurons.

A number of other important consequences of finite geometry are detailed in Chapter 3, the most surprising of which is the following non-monotonic behavior: while adding more sensory hairs to a simple linear array acts to increase peak flux metrics for high sampling speeds and sparse arrays, the opposite occurs for low sampling speeds and dense arrays of closely spaced hairs. These fundamental changes in odorant sampling performance are not well predicted by trends in leakiness alone, even though the two are undoubtedly related. This suggests that the dynamics of scalar transport to biological hair arrays should be investigated explicitly, since simple parameters describing the fluid flow are not sufficient to explain trends in odorant sampling performance.

Simple linear rows of hairs, even those of finite width, are still a far cry from the antennule morphologies of many crustacean species. Therefore, Chapter 4 examines a particular species' aesthetasc array in detail - that of the well studied Florida spiny lobster, *P. argus*. A state-of-the-art 3D tomographic scan was performed of an actual antennule, and a parallelized image segmentation method designed to extract the surface geometry is presented. This segmentation algorithm seems promising for tomography of biological appendages composed of densely spaced, hair-like structures. The scan of the *P. argus* antennule shows frequent deviation from the idealized zig-zag pattern of aesthetascs previously described in the literature, emphasizing the importance of natural variability in morphology even within a single antennule. Nonetheless, average properties of the morphology agree with previous measurements, and were used to build a simplified 2D numerical model of the V-formations making up the zig-zag array. A V-formation of hairs does effectively channel flow through the aesthetascs as previously hypothesized in the literature, but as the work in Chapter 3 shows, this does not imply more effective odorant sampling. Indeed, a simple straight row of hairs in crossflow achieves higher peak flux, peak onset slope, and total flux than any V-formation tested. A V-formation does result in a longer period of chemical flux to sensors, and both olfactory neurons and current engineered chemical sensors might benefit

from this sampling behavior since both have relatively long response times. However, these results remind us that biological solutions are often not optimal solutions for engineering problems such as plume tracking robots, and should be viewed as a viable starting point instead of a final design.

## Future directions

This work focused on an analysis of the temporal features of the odorant flux time series that result when an array of flux-detectors samples a turbulent plume. These time series are presumably used by organisms to perceive the spatial structure of their odor environment. However, additional information could be extracted from these signals by considering the spatial arrangement of olfactory hairs within the array. If an odorant patch that exhibited variation along the span of the array were sampled, this variation could in principle be estimated by comparing the sensory output from each hair. Thus, a fruitful future research direction might investigate various types of odorant patches, in addition to the simple Gaussian filament studied here, to determine how their structures might be reconstructed from patterns of sensor response across the arrays.

Strong evidence is presented here that suggests the duration of odorant stimulation during the flick downstroke is too short for odorant detection or quantification to occur in benthic crustaceans such as lobsters. This implies that the return stroke and inter-flick pause during typical sampling behavior are important if thin, 1 mm odorant filaments are to be detected. Although it is popularly believed that these phases of the flicking motion allow sufficient time for diffusion of odorant molecules trapped in the array to diffuse to aesthetasc surfaces and be detected, this hypothesis has never been explicitly tested. A simulation of a complete flick/return/pause sequence would help quantify the proportation of odorant flux that occurs during each phase, and whether neural stimulation is indeed lengthened substantially by trapping of odorant during the return stroke and pause. However, this type of numerical simulation would probably be costly: a very large, highly resolved domain would be needed to contain the entire back-and-forth advection distance of the odorant filament during the complete flicking sequence.

Real aesthetasc array morphologies are 3D due to the presence of the antennule to which the hairs are attached, and the finite length of the hairs themselves. This three dimensionality is likely to have a profound impact on flow and odorant transport dynamics because water can move around the array in two different dimensions, reducing leakiness and perhaps odorant sampling performance compared to a 2D array. Complete segmentation of the surface geometry of our scanned *P. argus* antennule would provide boundary conditions for

input into numerical simulations of a plume sampling event by a real 3D morphology. By comparing odorant sampling performance of the scanned geometry to idealized, but still 3D, simplifications (e.g., no guard hairs, straight row versus zig-zag), the importance and possible utility of each aspect of the real morphology could be deduced.

Over the course of this research project, it became increasingly apparent how little is known in the field of animal olfaction and turbulent plume tracking behavior. The large range of important spatial scales involved, from the turbulent eddies that form filamentous chemical structures to the microscopic aesthetascs arrayed along the antennules, make a comprehensive treatment of the problem very difficult. The fact that many other chemosensory structures are distributed over a crustacean's body further complicates the question of how these animals perceive their odor environment. Nonetheless, the aesthetascs are known to play an important role in orientation and navigation in odor plumes, so developing a detailed understanding of their functioning is worthwhile. One of the major difficulties in putting the results of the present work in a meaningful perspective is the lack of neurobiological data for these sensory structures when they undergo transient exposure to odorant. Although a virtual sensor can be used to normalize plume sampling performance to what is theoretically possible, it does not help distinguish differences in performance that are biologically significant from those that are not. To do that, it is crucial that more extensive measurements of neural response under realistic plume conditions be performed.

# Bibliography


Andreas Acrivos and Thomas D. Taylor. Heat and mass transfer from single spheres in stokes flow. *Physics of Fluids*, 5(4):387–394, 1962.

I. Alameddine and M. El-Fadel. Brine discharge from desalination plants: a modeling approach to an optimized outfall design. *Desalination*, 214(1-3):241–260, 2007.

M. E. Hassan Amrani, Richard M. Dowdeswell, Peter A. Payne, and Krishna C. Persaud. An intelligent gas sensing system. *Sensors and Actuators B: Chemical*, 44(1-3):512 – 516, 1997.

J. Atema. Chemoreception in the sea: adaptations of chemoreceptors and behaviour to aquatic stimulus conditions. *Symposia of the Society for Experimental Biology*, pages 387–423, 1985.

J. Atema. Distribution of chemical stimuli. *Sensory biology of aquatic animals.*, pages 29–56, 1988.

J. Atema. Eddy chemotaxis and odor landscapes: Exploration of nature with animal sensors. *Biological Bulletin*, 191(1):129–138, 1996.

Jelle Atema. Chemical signals in the marine environment: Dispersal, detection, and temporal signal analysis. *Proceedings of the National Academy of Sciences of the United States of America*, 92(1):62–66, 1995.

M. F. Barad, P. Colella, and S. G. Schladow. An adaptive cut-cell method for environmental fluid mechanics. *International Journal For Numerical Methods In Fluids*, 60(5):473–514, June 2009.

H. B. Barlow. Temporal and spatial summation in human vision at different background intensities. *Journal of Physiology*, 141(2):337–350, 1958.

P.R. Bevington and D.K. Robinson. *Data reduction and error analysis for the physical sciences*. McGraw-Hill Higher Education. McGraw-Hill, 2003.

V. Bisignanesi and M. S. Borgas. Models for integrated pest management with chemicals in atmospheric surface layers. *Ecological Modelling*, 201(1):2–10, 2007.

DN Blaustein, RB Simmons, MF Burgess, CD Derby, M Nishikawa, and KS Olson. Ultrastructural localization of 5'amp odorant receptor sites on the dendrites of olfactory receptor neurons of the spiny lobster. *The Journal of Neuroscience*, 13(7):2821–2828, 1993.

Richard Brown. fitellipse.m: Fit ellipses to 2d points using linear or nonlinear least squares, 2007. URL `http://www.mathworks.com/matlabcentral/fileexchange/15125`.

E. Bursell. Observations on the orientation of tsetse flies (*Glossina pallidipes*) to wind-borne odors. *Physiological Entomology*, 9(2):133–137, 1984.

R. S. Cantor, H. Ishida, and J. Janata. Sensing array for coherence analysis of modulated aquatic chemical plumes. *Analytical Chemistry*, 80(4):1012–1018, 2008.

W. E. S. Carr, H. G. Trapidorosenthal, and R. A. Gleeson. The role of degradative enzymes in chemosensory processes. *Chemical Senses*, 15(2):181–190, April 1990.

K. Y. Chan, H. Fujioka, R. H. Bartlett, R. B. Hirschl, and J. B. Grotberg. Pulsatile flow and mass transport over an array of cylinders: Gas transfer in a cardiac-driven artificial lung. *Journal of Biomechanical Engineering-Transactions of the ASME*, 128(1):85–96, 2006.

Dipankar Chatterjee, Gautam Biswas, and Sakir Amiroudine. Numerical investigation of forced convection heat transfer in unsteady flow past a row of square cylinders. *International Journal of Heat and Fluid Flow*, 30(6):1114 – 1128, 2009.

A. Y. L. Cheer and M. A. R. Koehl. Fluid-flow through filtering appendages of insects. *IMA Journal of Mathematics Applied in Medicine and Biology*, 4(3):185–199, 1987a.

A. Y. L. Cheer and M. A. R. Koehl. Paddles and rakes - fluid-flow through bristled appendages of small organisms. *Journal of Theoretical Biology*, 129(1):17–39, 1987b.

M. F. Cooperband and R. T. Carde. Comparison of plume structures of carbon dioxide emitted from different mosquito traps. *Medical and Veterinary Entomology*, 20(1):1–10, 2006.

J. Crimaldi. Planar laser induced fluorescence in aqueous flows. *Experiments in Fluids*, 44 (6):851–863, 2008.

J. P. Crimaldi and J. R. Koseff. High-resolution measurements of the spatial and temporal scalar structure of a turbulent plume. *Experiments in Fluids*, 31(1):90–102, 2001.

J. P. Crimaldi and J. R. Koseff. Structure of turbulent plumes from a momentumless source in a smooth bed. *Environmental Fluid Mechanics*, 6(6):573–592, 2006.

J. P. Crimaldi, M. A. R. Koehl, and J. R. Koseff. Effects of the resolution and kinematics of olfactory appendages on the interception of chemical signals in a turbulent odor plume. *Environmental Fluid Mechanics*, 2(1):35–64, 2002a.

J. P. Crimaldi, M. B. Wiley, and J. R. Koseff. The relationship between mean and instantaneous structure in turbulent passive scalar plumes. *Journal of Turbulence*, 3:1–23, 2002b.

Shamik DasGupta and Scott Waddell. Learned odor discrimination in drosophila without combinatorial odor maps in the antennal lobe. *Current Biology*, 18(21):1668 – 1674, 2008.

C. T. David, J. S. Kennedy, and A. R. Ludlow. Finding of a sex-pheromone source by gypsy moths released in the field. *Nature*, 303(5920):804–806, 1983.

A. De Robertis, C. A. Morgan, R. A. Schabetsberger, R. W. Zabel, R. D. Brodeur, R. L. Emmett, C. M. Knight, G. K. Krutzikowsky, and E. Casillas. Columbia river plume fronts. ii. distribution, abundance, and feeding ecology of juvenile salmon. *Marine Ecology-Progress Series*, 299:33–44, 2005.

M. del Valle. Electronic tongues employing electrochemical sensors. *Electroanalysis*, 22(14): 1539–1555, July 2010.

C. D. Derby, H. S. Cate, and L. R. Gentilcore. Perireception in olfaction: Molecular mass sieving by aesthetasc sensillar cuticle determines odorant access to receptor sites in the caribbean spiny lobster *Panulirus argus*. *Journal of Experimental Biology*, 200(15):2073–2081, 1997.

John D'Errico. Slm - shape language modeling, 2010. URL `http://www.mathworks.com/matlabcentral/fileexchange/24443-slm-shape-language-modeling`.

B. D. Dickman, D. R. Webster, J. L. Page, and M. J. Weissburg. Three-dimensional odorant concentration measurements around actively tracking blue crabs. *Limnology and Oceanography-methods*, 7:96–108, January 2009.

W. Ernst, P. Jackman, K. Doe, F. Page, G. Julien, K. Mackay, and T. Sutherland. Dispersion and toxicity to non-target aquatic organisms of pesticides used to treat sea lice on salmon in net pen enclosures. *Marine Pollution Bulletin*, 42(6):433–444, 2001.

M. C. Ferner and M. J. Weissburg. Slow-moving predatory gastropods track prey odors in fast and turbulent flow. *Journal of Experimental Biology*, 208(5):809–819, 2005.

C. M. Finelli, N. D. Pentcheff, R. K. Zimmer-Faust, and D. S. Wethey. Odor transport in turbulent flows: Constraints on animal navigation. *Limnology and Oceanography*, 44(4): 1056–1071, 1999.

Hugo B. Fischer, John E. List, Robert C. Koh, Jorg Imberger, and Norman H. Brooks. *Mixing in Inland and Coastal Waters*. Academic Press, November 1979.

S. K. Friedlander. Mass and heat transfer to single spheres and cylinders at low reynolds numbers. *AIChE J.*, 3(1):43–48, 1957.

R. A. Gleeson. Morphological and behavioral identification of the sensory structures mediating pheromone reception in the blue-crab, *Callinectes sapidus*. *Biological Bulletin*, 163 (1):162–171, 1982.

R. A. Gleeson, W. E. S. Carr, and H. G. Trapidorosenthal. Morphological-characteristics facilitating stimulus access and removal in the olfactory organ of the spiny lobster, *Panulirus argus* - insight from the design. *Chemical Senses*, 18(1):67–75, 1993.

J. A. Goldman and M. A. R. Koehl. Fluid dynamic design of lobster olfactory organs: High speed kinematic analysis of antennule flicking by *Panulirus argus*. *Chemical Senses*, 26 (4):385–398, 2001.

J. A. Goldman and S. N. Patek. Two sniffing strategies in palinurid lobsters. *Journal of Experimental Biology*, 205(24):3891–3902, 2002.

G. Gomez and J. Atema. Time-course of recovery from adaptation by hydroxyproline-sensitive lobster olfactory receptor neurons. *Biological Bulletin*, 187(2):259–260, 1994.

G. Gomez and J. Atema. Temporal resolution in olfaction: Stimulus integration time of lobster chemoreceptor cells. *Journal of Experimental Biology*, 199(8):1771–1779, 1996a.

G. Gomez and J. Atema. Temporal resolution in olfaction II: time course of recovery from adaptation in lobster chemoreceptor cells. *Journal of Neurophysiology*, 76(2):1340–1343, 1996b.

G. Gomez, R. Voigt, and J. Atema. Frequency filter properties of lobster chemoreceptor cells determined with high-resolution stimulus measurement. *Journal of Comparative Physiology a-Sensory Neural and Behavioral Physiology*, 174(6):803–811, 1994.

G. Gomez, R. Voigt, and J. Atema. Temporal resolution in olfaction III: flicker fusion and concentration-dependent synchronization with stimulus pulse trains of antennular chemoreceptor cells in the american lobster. *Journal of Comparative Physiology a-Sensory Neural and Behavioral Physiology*, 185(5):427–436, 1999.

F. W. Grasso and J. A. Basil. How lobsters, crayfishes, and crabs locate sources of odor: current perspectives and future directions. *Current Opinion in Neurobiology*, 12(6):721–727, 2002.

F. W. Grasso, T. R. Consi, D. C. Mountain, and J. Atema. Biomimetic robot lobster performs chemo-orientation in turbulence using a pair of spatially separated sensors: Progress and challenges. *Robotics and Autonomous Systems*, 30(1-2):115–131, 2000.

U. Grunert and B. W. Ache. Ultrastructure of the aesthetasc (olfactory) sensilla of the spiny lobster, *Panulirus argus*. *Cell and Tissue Research*, 251(1):95–103, 1988.

E. Hallberg, K. U. I. Johansson, and R. Elofsson. The aesthetasc concept - structural variations of putative olfactory receptor cell complexes in crustacea. *Microscopy Research and Technique*, 22(4):325–335, 1992.

Taeheon Han, Kyung-Soo Yang, and Kyongjun Lee. Heat transfer characterization of two isothermal circular cylinders in proximity. *Journal of Heat Transfer*, 132(3):034504, 2010.

B. Hansen and P. Tiselius. Flow through the feeding structures of suspension feeding zooplankton - a physical model approach. *Journal of Plankton Research*, 14(6):821–834, 1992.

D. J. Harvey, T. F. Lu, and M. A. Keller. Comparing insect-inspired chemical plume tracking algorithms using a mobile robot. *IEEE Transactions On Robotics*, 24(2):307–317, April 2008a.

D. J. Harvey, T. F. Lu, and M. A. Keller. Effectiveness of insect-inspired chemical plume-tracking algorithms in a shifting wind field. *IEEE Transactions On Robotics*, 24(1): 196–201, February 2008b.

Hanns Hatt and Barry W. Ache. Patch-clamping arthropod olfactory receptor neurons to study mechanisms of olfactory transduction. *Journal of Neuroscience Methods*, 69(1):43 – 49, 1996.

E. L. Hines, E. Llobet, and J. W. Gardner. Electronic noses: a review of signal processing techniques. *IEE Proceedings-Circuits Devices and Systems*, 146(6):297–310, December 1999.

D. C. Hood and B. G. Grover. Temporal summation of light by a vertebrate visual receptor. *Science*, 184(4140):1003–1005, 1974.

A. J. Horner, M. J. Weissburg, and C. D. Derby. Dual antennular chemosensory pathways can mediate orientation by caribbean spiny lobsters in naturalistic flow conditions. *Journal of Experimental Biology*, 207(21):3785–3796, 2004.

M. H. Huesemann, A. D. Skillman, and E. A. Crecelius. The inhibition of marine nitrification by ocean disposal of carbon dioxide. *Marine Pollution Bulletin*, 44(2):142–148, 2002.

H. Ishida, G. Nakayama, T. Nakamoto, and T. Moriizumi. Controlling a gas/odor plume-tracking robot based on transient responses of gas sensors. *IEEE Sensors Journal*, 5(3): 537–545, June 2005.

Hiroshi Ishida and Toysaka Moriizumi. *Machine Olfaction for Mobile Robots*, pages 399–417. Wiley-VCH Verlag GmbH & Co. KGaA, 2004.

D. James, S. M. Scott, Z. Ali, and W. T. O'Hare. Chemical sensors for electronic nose systems. *Microchimica Acta*, 149(1-2):1–17, February 2005.

G. Juncu. Conjugate heat/mass transfer from a circular cylinder with an internal heat/mass source in laminar crossfiow at low reynolds numbers (vol 48, 419, 2005). *International Journal of Heat and Mass Transfer*, 51(11-12):3255–3256, 2008.

S Junek, E Kludt, F Wolf, and D Schild. Olfactory coding with patterns of response latencies. *Neuron*, 67(5):872–84, 2010.

K. E. Kaissling. Flux detectors versus concentration detectors: Two types of chemoreceptors. *Chemical Senses*, 23(1):99–111, February 1998.

S. Kazadi, R. Goodman, D. Tsikata, D. Green, and H. Lin. An autonomous water vapor plume tracking robot using passive resistive polymer sensors. *Autonomous Robots*, 9(2): 175–188, September 2000.

T. A. Keller and M. J. Weissburg. Effects of odor flux and pulse rate on chemosensory tracking in turbulent odor plumes by the blue crab, *Callinectes sapidus*. *Biological Bulletin*, 207(1):44–55, 2004.

T. A. Keller, I. Powell, and M. J. Weissburg. Role of olfactory appendages in chemically mediated orientation of blue crabs. *Marine Ecology-Progress Series*, 261:217–231, 2003.

T. Kikas, P. Janata, H. Ishida, and J. Janata. Chemical plume tracking. 2. multiple-frequency modulation. *Analytical Chemistry*, 73(15):3669–3673, 2001a.

Timo Kikas, Hiroshi Ishida, Donald R. Webster, and Jiri Janata. Chemical plume tracking. 1. chemical information encoding. *Analytical Chemistry*, 73(15):3662–3668, 2001b.

V.A. Kirsch. Stokes flow in model fibrous filters. *Separation and Purification Technology*, 58(2):288 – 294, 2007.

M. A. R. Koehl. Hairy little legs: Feeding, smelling, and swimming at low reynolds number. fluid dynamics in biology. *Contemporary Mathematics*, 141:33–64, 1992.

M. A. R. Koehl. Fluid flow through hair-bearing appendages: feeding, smelling and swimming at low and intermediate reynolds numbers. *Symposia of the Society for Experimental Biology*, 49:157–182, 1995.

M. A. R. Koehl. Small-scale fluid dynamics of olfactory antennae. *Marine and Freshwater Behaviour and Physiology*, 27(2-3):127–141, 1996.

M. A. R. Koehl. Transitions in function at low reynolds number: hair-bearing animal appendages. *Mathematical Methods in the Applied Sciences*, 24(17-18):1523–1532, 2001a.

M. A. R. Koehl. Fluid dynamics of animal appendages that capture molecules: Arthropod olfactory antennae. In L. Fauci and S. Gueron, editors, *IMA Workshop on Computational Modeling in Biological Fluid Dynamics*, pages 97–116, 2001b.

M. A. R. Koehl. Physical modelling in biomechanics. *Philosophical Transactions of the Royal Society of London Series B-Biological Sciences*, 358(1437):1589–1596, 2003.

M. A. R. Koehl. Biomechanics of microscopic appendages: functional shifts caused by changes in speed. *Journal of Biomechanics*, 37(6):789–795, 2004.

M. A. R. Koehl. The fluid mechanics of arthropod sniffing in turbulent odor plumes. *Chemical Senses*, 31(2):93–105, 2006.

M. A. R. Koehl, J. R. Koseff, J. P. Crimaldi, M. G. McCay, T. Cooper, M. B. Wiley, and P. A. Moore. Lobster sniffing: Antennule design and hydrodynamic filtering of information in an odor plume. *Science*, 294(5548):1948–1951, 2001.

C. F. Lange, F. Durst, and M. Breuer. Momentum and heat transfer from cylinders in laminar crossflow at 10(-4)<= Re <= 200. *International Journal of Heat and Mass Transfer*, 41(22):3409–3430, 1998.

M. S. Laverack. The diversity of chemoreceptors. In J. Atema, editor, *Sensory Biology of Aquatic Animals*, pages 287–317. Springer-Verlag, New York, 1988.

A. B. P. Leonard. *The biomechanics, autecology and behavior of suspension-feeding in crinoid echinoderms.* PhD thesis, University of California, San Diego, 1992.

Qian Liao and Edwin A. Cowen. The information content of a scalar plume - a plume tracing perspective. *Environmental Fluid Mechanics*, 2:9–34, 2002.

C. Loudon and M. A. R. Koehl. Sniffing by a silkworm moth: Wing fanning enhances air penetration through and pheromone interception by antennae. *Journal of Experimental Biology*, 203(19):2977–2990, 2000.

C. Loudon, B. A. Best, and M. A. R. Koehl. When does motion relative to neighboring surfaces alter the flow-through arrays of hairs. *Journal of Experimental Biology*, 193: 233–254, 1994.

D. Martinez, O. Rochel, and E. Hugues. A biomimetic robot for tracking specific odors in turbulent plumes. *Autonomous Robots*, 20(3):185–195, 2006.

K. S. Mead. From odor molecules to plume tracking: An interdisciplinary, multilevel approach to olfaction in stomatopods. *Integrative and Comparative Biology*, 42(2):258–264, 2002.

K. S. Mead and M. A. R. Koehl. Stomatopod antennule design: The asymmetry, sampling efficiency and ontogeny of olfactory flicking. *Journal of Experimental Biology*, 203(24): 3795–3808, 2000.

K. S. Mead and T. M. Weatherby. Morphology of stomatopod chemosensory sensilla facilitates fluid sampling. *Invertebrate Biology*, 121(2):148–157, 2002.

K. S. Mead, M. A. R. Koehl, and M. J. O'Donnell. Stomatopod sniffing: the scaling of chemosensory sensillae and flicking behavior with body size. *Journal of Experimental Marine Biology and Ecology*, 241(2):235–261, 1999.

K. S. Mead, M. B. Wiley, M. A. R. Koehl, and J. R. Koseff. Fine-scale patterns of odor encounter by the antennules of mantis shrimp tracking turbulent plumes in wave-affected and unidirectional flow. *Journal of Experimental Biology*, 206(1):181–193, 2003.

W. C. Michel and B. W. Ache. Odor-evoked inhibition in primary olfactory receptor neurons. *Chemical Senses*, 19(1):11–24, 1994.

P. Moore and J. Crimaldi. Odor landscapes and animal behavior: tracking odor plumes in different physical worlds. *Journal of Marine Systems*, 49(1-4):55–64, 2004.

P. A. Moore. *Aquatic odor signals: their structure, filtering, and behavioral use in the lobster,* Homarus americanus. PhD thesis, Boston University, 1991.

P. A. Moore and J. Atema. Spatial information in the 3-dimensional fine-structure of an aquatic odor plume. *Biological Bulletin*, 181(3):408–418, 1991.

P. A. Moore, G. A. Gerhardt, and J. Atema. High-resolution spatiotemporal analysis of aquatic chemical signals using microelectrochemical electrodes. *Chemical Senses*, 14(6): 829–840, 1989.

P. A. Moore, J. Atema, and G. A. Gerhardt. Fluid-dynamics and microscale chemical movement in the chemosensory appendages of the lobster, *Homarus americanus*. *Chemical Senses*, 16(6):663–674, 1991a.

P. A. Moore, N. Scholz, and J. Atema. Chemical orientation of lobsters, *Homarus americanus*, in turbulent odor plumes. *Journal of Chemical Ecology*, 17(7):1293–1307, 1991b.

P. A. Moore, R. K. Zimmer-Faust, S. L. Bement, M. J. Weissburg, J. M. Parrish, and G. A. Gerhardt. Measurement of microscale patchiness in a turbulent aquatic odor plume using a semiconductor-based microprobe. *Biological Bulletin*, 183(1):138–142, 1992.

P. A. Moore, M. J. Weissburg, J. M. Parrish, R. K. Zimmer-Faust, and G. A. Gerhardt. Spatial-distribution of odors in simulated benthic boundary-layer flows. *Journal of Chemical Ecology*, 20(2):255–279, 1994.

J. Murlis. Odor plumes and the signal they provide. In R. T. Carde and A. Minks, editors, *Insect Pheromone Research: New Directions*, pages 221–231. Chapman and Hall, New York, 1997.

J. Murlis and C. D. Jones. Fine-scale structure of odor plumes in relation to insect orientation to distant pheromone and other attractant sources. *Physiological Entomology*, 6(1): 71–86, 1981.

J. Murlis, J. S. Elkinton, and R. T. Carde. Odor plumes and how insects use them. *Annual Review of Entomology*, 37:505–532, 1992.

T. Nakamoto and H. Ishida. Chemical sensing in spatial/temporal domains. *Chemical Reviews*, 108(2):680–704, 2008.

Rody Oldenhuis. Determine the distance between two ellipses (in 3d), 2010. URL `http://www.mathworks.com/matlabcentral/fileexchange/26329-determine-the-distance-between-two-ellipses-in-3d`.

J. L. Page, B. D. Dickman, D. R. Webster, and M. J. Weissburg. Getting ahead: context-dependent responses to odorant filaments drive along-stream progress during odor tracking in blue crabs. *Journal of Experimental Biology*, 214(9):1498–1512, May 2011a.

J. L. Page, B. D. Dickman, D. R. Webster, and M. J. Weissburg. Staying the course: chemical signal spatial properties and concentration mediate cross-stream motion in turbulent plumes. *Journal of Experimental Biology*, 214(9):1513–1522, May 2011b.

P. Pyk, S. B. I. Badia, U. Bernardet, P. Knusel, M. Carlsson, J. Gu, E. Chanie, B. S. Hansson, T. C. Pearce, and Pfmj Verschure. An artificial moth: Chemical source localization using a robot based neuronal model of moth optomotor anemotactic search. *Autonomous Robots*, 20(3):197–213, 2006.

Pamela B. Reeder and Barry W. Ache. Chemotaxis in the florida spiny lobster, *Panulirus argus*. *Animal Behaviour*, 28(3):831 – 839, 1980.

M. A. Reidenbach, N. George, and M. A. R. Koehl. Antennule morphology and flicking kinematics facilitate odor sampling by the spiny lobster, *Panulirus argus*. *Journal of Experimental Biology*, 211(17):2849–2858, September 2008.

Jean-Pierre Rospars, Vlastimil Krivan, and Petr Lansky. Perireceptor and receptor events in olfaction. comparison of concentration and flux detectors: a modeling study. *Chem. Senses*, 25(3):293–311, 2000.

D. I. Rubenstein and M. A. R. Koehl. Mechanisms of filter feeding - some theoretical considerations. *American Naturalist*, 111(981):981–994, 1977.

G. S. Settles. Sniffers: Fluid-dynamic sampling for olfactory trace detection in nature and homeland security - the 2004 freeman scholar lecture. *Journal of Fluids Engineering-Transactions of the ASME*, 127(2):189–218, 2005.

M. Spencer and K. A. Linberg. Ultrastructure of aesthetasc innervation and external morphology of the lateral antennule setae of the spiny lobster *Panulirus interruptus* (Randall). *Cell and Tissue Research*, 245(1):69–80, 1986.

Hartwig Spors, Matt Wachowiak, Lawrence B. Cohen, and Rainer W. Friedrich. Temporal dynamics and latency patterns of receptor neuron input to the olfactory bulb. *The Journal of Neuroscience*, 26(4):1247–1259, 2006.

M. T. Stacey, K. S. Mead, and M. A. R. Koehl. Molecule capture by olfactory antennules: Mantis shrimp. *Journal of Mathematical Biology*, 44(1):1–30, 2002.

G. Stanescu, A. J. Fowler, and A. Bejan. The optimal spacing of cylinders in free-stream cross-flow forced convection. *International Journal of Heat and Mass Transfer*, 39(2): 311–317, 1996.

P. Steullet, H. S. Cate, W. C. Michel, and C. D. Derby. Functional units of a compound nose: Aesthetasc sensilla house similar populations of olfactory receptor neurons on the crustacean antennule. *Journal of Comparative Neurology*, 418(3):270–280, March 2000.

C. Y. Su, C. Martelli, T. Emonet, and J. R. Carlson. Temporal coding of odor mixtures in an olfactory receptor neuron. *Proceedings of the National Academy of Sciences of the United States of America*, 108(12):5075–5080, March 2011.

K. Tamada and H. Fujikawa. The steady flow of viscous fluid at low reynolds numbers passing obliquely through a plane grid made of equal parallel circular cylinders. *Journal of the Physical Society of Japan*, 14(2):202–216, 1959.

Henry G. Trapido-Rosenthal, William E. S. Carr, and Richard A. Gleeson. Biochemistry of an olfactory purinergic system: Dephosphorylation of excitatory nucleotides and uptake of adenosine. *Journal of Neurochemistry*, 49(4):1174–1182, 1987.

Yu. Vlasov, Yu. Ermolenko, A. Legin, A. Rudnitskaya, and V. Kolodnikov. Chemical sensors and their systems. *Journal of Analytical Chemistry*, 65:880–898, 2010.

Mingyu Wang and John G. Georgiadis. Conjugate forced convection in crossflow over a cylinder array with volumetric heating. *International Journal of Heat and Mass Transfer*, 39(7):1351 – 1361, 1996.

D. R. Webster and M. J. Weissburg. Chemosensory guidance cues in a turbulent chemical odor plume. *Limnology and Oceanography*, 46(5):1034–1047, 2001.

D. R. Webster, S. Rahman, and L. P. Dasi. On the usefulness of bilateral comparison to tracking turbulent chemical odor plumes. *Limnology and Oceanography*, 46(5):1048–1053, 2001.

D. R. Webster, S. Rahman, and L. P. Dasi. Laser-induced fluorescence measurements of a turbulent plume. *Journal of Engineering Mechanics-ASCE*, 129(10):1130–1137, 2003.

D.R. Webster and M J Weissburg. The hydrodynamics of chemical cues among aquatic organisms. *Annual Review of Fluid Mechanics*, 41:73–90, 2009 2009.

M. J. Weissburg and R. K. Zimmer-Faust. Life and death in moving fluids - hydrodynamic effects on chemosensory-mediated predation. *Ecology*, 74(5):1428–1443, 1993.

S. B. Wilson and J. M. Anderson. A thermal plume in the tay estuary detected by aerial thermography. *International Journal of Remote Sensing*, 5(1):247–249, 1984.

Seong-Yeon Yoo, Hwa-Kil Kwon, and Jin-Hyuk Kim. A study on heat transfer characteristics for staggered tube banks in cross-flow. *Journal of Mechanical Science and Technology*, 21:505–512, 2007.

W. R. Young and Scott Jones. Shear dispersion. *Physics of Fluids A: Fluid Dynamics*, 3 (5):1087–1101, 1991.

E. Zettler and J. Atema. Chemoreceptor cells as concentration slope detectors: Preliminary evidence from the lobster nose. *Biological Bulletin*, 197(2):252–253, 1999.

R. K. Zimmer-Faust, C. M. Finelli, N. D. Pentcheff, and D. S. Wethey. Odor plumes and animal navigation in turbulent water-flow - a field-study. *Biological Bulletin*, 188(2): 111–116, 1995.

# A. Virtual sensor normalization

The flux into the virtual sensor at a given time is equal to $C(t)U_0\left[ND + (N-1)G\right]$ where $C(t)$ is odorant concentration anywhere along the sensor (the line segment of cross-stream width $ND + (N-1)G$). Therefore, peak flux corresponds with the maximum concentration of the filament, peak slope corresponds with the maximum spatial slope of the filament, and total flux corresponds with the total odorant mass contained in this cross-stream section of the Gaussian filament. We define flux duration in a similar manner to how it is defined for the real arrays; that is, the smallest cross-stream distance that contains 95% of the total mass in the filament. Therefore, the flux metrics for a virtual sensor are:

- peak flux $= C_0U_0\left[ND + (N-1)G\right]$
- peak slope $= \frac{C_0U_0^2e^{-0.5}}{\sigma_f}\left[ND + (N-1)G\right]$
- time integrated flux $= C_0\sigma_f\sqrt{2\pi}\left[ND + (N-1)G\right]$
- duration $= width_{95}/U_0$ where $width_{95} = 0.560$ mm, which corresponds to the smallest cross-stream interval that contains 95% of mass in the odorant filament

# B. Image segmentation algorithm

**Listing B.1:** Method used to segment antennule cross-sections, summarized as MATLAB pseudocode.

```
%initial manual segmentation of ellipse

load, threshold, and display initial image (slice = 0);
maskedpoints = imfreehand();
[x0,y0,a,b,alpha] = fitellipse(maskedpoints); %outputs are center coordinates
    , major and minor axes, and rotation angle
save fit parameters

%automatic ellipse fits for the rest of this tile of data (2000 slices)

for slice = 1:1999
        load and threshold current image;

        maskedpoints = pixels inside ellipse defined by
        (x0,y0,a+5,b+5,alpha) AND outside ellipse defined by
        (x0,y0,a-5,b-5,alpha)

        [x0,y0,a,b,alpha] = fitellipse(maskedpoints);
        save fit parameters
end

%initial manual guess of ellipse cutoff point location (slice = 0), followed
    by automatic location of cutoff points in all slices
%this is done twice, for both top and bottom cutoff locations

load and display slice 0;
xg = user input;
for slice = 0:1999
        load and threshold current image;
        load (x0,y0,a,b,alpha) for ellipse fit in current slice
        for xw = xg+45 : -1 : xg-45 %loop right edge of interrogation window
            from right to left

                maskedpoints = pixels inside ellipse defined by
```

```
                (x0,y0,a+10,b+10,alpha) AND outside ellipse defined by
                (x0,y0,a-10,b-10,alpha) AND for which xw-10 <= x <= xw

                if numel(maskedpoints) < 10
                        xc = xw + 70;  %70 pixel safety factor
                        xg = xw;
                        break;
                end

        end

        if xw == xg-45 %break condition never reached
                xc = xw + 45 + 70;
        end

        yc = y-coordinate matching xc on current ellipse fit

end

%initial manual fit of cubic spline

load, threshold, and display slice 0;
load (x0,y0,a,b,alpha) for ellipse fit in current slice
load top and bottom cutoff points in current slice
evaluate slopes of ellipse at top and bottom points

maskedpoints = imfreehand();

settings = slmset('leftslope',bottom slope,'rightslope',top slope,'leftvalue
    ',top x-cutoff,'rightvalue',bottom x-cutoff,'knots',8);
slm = slmengine(maskedpoints,settings);  %fitting routine
ypts = linspace(top y-cutoff, bottom y-cutoff, 1500);  %1500 evenly spaced
    points
xpts = slmeval(ypts,slm)  %evaluate spline at these locations


%automatic spline fits for all slices
for slice = 0:1999

        load and threshold current slice
        load (x0,y0,a,b,alpha) for ellipse fit in current slice
        load top and bottom cutoff points in current slice
        evaluate slopes of ellipse at top and bottom points

        lox = NaN(size(xpts));  hix = NaN(size(xpts));

        %get x-coordinates that will demarcate masked region
```

```
        %720 <= y <= 1025 contains "inner" section of spline where
            aesthetascs tend to merge

        lox(ypts<720 | ypts>1025) = xpts(ypts<720 | ypts>1025) - 6.5;
        hix(ypts<720 | ypts>1025) = xpts(ypts<720 | ypts>1025) + 5;
        lox(ypts>720 & ypts<1025) = xpts(ypts>720 & ypts<1025) - 7.5;
        hix(ypts>720 & ypts<1025) = xpts(ypts>720 & ypts<1025) + 5;

        %create mask from closed polygon formed by these points
        mask = poly2mask([lox fliplr(hix)],[ypts fliplr(ypts)]);

        maskedpoints = points inside mask AND between top and bottom cutoffs

        %fit spline to masked points
        settings = slmset('leftslope',bottom slope,'rightslope',top slope,'
            leftvalue',top x-cutoff,'rightvalue',bottom x-cutoff,'knots',8);
        slm = slmengine(maskedpoints,settings); %fitting routine
        ypts = linspace(top y-cutoff, bottom y-cutoff, 1500); %1500 evenly
            spaced points
        xpts = slmeval(ypts,slm) %evaluate spline at these locations

        save spline parameters (slm) for current slice

end
```

**Listing B.2:** Method used to segment aesthetasc and guard hair cross-sections, summarized as MATLAB pseudocode.

```
%manual segmentation of ellipses for slice s

while (user input continues)
        maskedpoints = imfreehand();
        [x0,y0,a,b,alpha] = fitellipse(maskedpoints); %outputs are center
            coordinates, major and minor axes, and rotation angle
        save fit parameters; %saving routine must keep track of which hair
            this is and in what slice
end

for slice = s+1:1999 %or s-1:-1:0 to work in other direction

%first group nearly-touching hairs
        for i = 1:numhairs %loop over all hairs in current slice
                for j = 1:numhairs %check overlap with every other hair
                        if comparing hair with itself or this pair is already
                            accounted for
                                continue;
                        end
```

```
                [xpts,ypts] = 100 equally spaced points along hair j
                    with a=a+2, b=b+2
                isoverlap = checkinside(hair i, xpts, ypts) %logical
                    matrix created by analytically checking whether
                    each point is inside hair i
                if any(isoverlap) %if at least one point on hair j is
                     inside hair i
                        group hair i and hair j together as a pair
                end
        end
end

combine pairs that share hairs in common into larger groups,
single hairs each form their own group

parfor i = 1:numgroups  %runs in parallel
        for j = 1:numhairs within group i
                load x0,y0,a,b,alpha for current hair in previous
                    slice

                subthresh = subregion of thresholded image bounded by
                     square centered on current hair's old location
                    and of side length a+40
                maskedpoints = pixels in subthresh that are inside
                    ellipse defined by
        (x0,y0,a+4,b+4,alpha) AND outside ellipse defined by
        (x0,y0,a-4,b-4,alpha) AND outside segmented antennule

                if numel(maskedpoints) <= 55
                        remove current hair from fitting routine
                        continue
                else
                        pts{j} = maskedpoints; %save pixels to fit to
                             each hair
                end

        end

        define lower and upper bounds for x0,y0,a,b,alpha of each
            fitted ellipse, these are allowed to change by +/-
            4,4,3,3,0.17, respectively, from fits of previous slice

        while (solution not converged)

                define initial guesses for x0,y0,a,b,alpha of each
                    ellipse as old values from previous slice, except
                    x0 and y0 are perturbed by +/- 2*rand
```

```
                    use fmincon to vary x0,y0,a,b,alpha for each ellipse
                        to minimize SSE,
                    subject to the constraint that no ellipse overlaps
                        with any other, or with pre-existing ellipses on
                        current slice:

                    for j = 1:numhairs within group i
                            compute distance of each maskedpoint in pts{j
                                } to ellipse j
                    end

                    for maskedpoints appearing in more than one cell of {
                        pts},
                            choose smallest distance and store which
                                ellipse it corresponds to
                    end

                    for j = 1:numhairs within group i
                            calculate and store relative location (inside
                                vs outside) of each maskedpoint and
                                corresponding closest ellipse
                    end

                    %compute average sum of squared distances
                    SSE = 0.25*sum((distances of inside points).^2) +
                        0.75*sum((distances of outside points).^2) / numel
                        (maskedpoints);

            end %while loop until convergence

            save all fit parameters

        end %parfor loop over groups

end %loop over slices
```